

Design, Finite Element and Experimental Analysis of Piezoelectric Tactile Sensors for Endoscopic Graspers

Harpiyar Singh

A Thesis
in
The Department
of
Mechanical Engineering

Presented in Partial Fulfillment of the Requirements
for The Degree of Master of Applied Science at
Concordia University
Montreal, Quebec, Canada.

December 2003

© Harpiyar Singh 2003



Library and
Archives Canada

Bibliothèque et
Archives Canada

Published Heritage
Branch

Direction du
Patrimoine de l'édition

395 Wellington Street
Ottawa ON K1A 0N4
Canada

395, rue Wellington
Ottawa ON K1A 0N4
Canada

Your file Votre référence

ISBN: 0-612-94733-5

Our file Notre référence

ISBN: 0-612-94733-5

The author has granted a non-exclusive license allowing the Library and Archives Canada to reproduce, loan, distribute or sell copies of this thesis in microform, paper or electronic formats.

L'auteur a accordé une licence non exclusive permettant à la Bibliothèque et Archives Canada de reproduire, prêter, distribuer ou vendre des copies de cette thèse sous la forme de microfiche/film, de reproduction sur papier ou sur format électronique.

The author retains ownership of the copyright in this thesis. Neither the thesis nor substantial extracts from it may be printed or otherwise reproduced without the author's permission.

L'auteur conserve la propriété du droit d'auteur qui protège cette thèse. Ni la thèse ni des extraits substantiels de celle-ci ne doivent être imprimés ou autrement reproduits sans son autorisation.

In compliance with the Canadian Privacy Act some supporting forms may have been removed from this thesis.

Conformément à la loi canadienne sur la protection de la vie privée, quelques formulaires secondaires ont été enlevés de cette thèse.

While these forms may be included in the document page count, their removal does not represent any loss of content from the thesis.

Bien que ces formulaires aient inclus dans la pagination, il n'y aura aucun contenu manquant.

Canada

ABSTRACT

Design, Finite Element and Experimental Analysis of Piezoelectric Tactile Sensors for Endoscopic Graspers

Harpiyar Singh

This dissertation reports on the design, experimentation and the finite element analysis of a prototype PVDF endoscopic tooth-like tactile sensor capable of measuring the compliance of a contact tissue/sensed object. Present day endoscopic graspers are designed tooth-like in order to grasp slippery tissues, but do not measure tissue tactile properties like force and softness. The main objective of this study is to design and model a sensor capable of measuring the total applied force on the sensed object as well as compliance of the tissue/sensed object. The sensor consists of a rigid and compliant cylindrical element. Determination of the compliance of sensed objects is based on the relative deformation of contact object/tissue on the compliant and rigid elements of the sensor. A PVDF film is sandwiched between rigid cylinder and plate, which measures the force applied on the rigid element. Another PVDF film is sandwiched between the two base plates to measure the total force applied on the sensor.

Using 2D finite element analysis, the tissue has been modeled as an elastic beam on rigid and elastic foundations and the results are compared with 3D ANSYS model. The compliance of the sensed object is measured by recording the PVDF films response under different load sets. The data obtained for the force variation are plotted against the dimensionless function λ , which is the function of thickness and Young's modulus of elasticity of both the sensor and the sensed object.

An array of the sensors was also designed in two different arrangements depending on the method of measuring the total applied force. These two different arrangements measure the total force on the sensed object using common base and different base plates in configurations. It has been shown that good agreement exists between the finite element results and experimental values for a single sensor and array of sensors. The sensor exhibits high force sensitivity and good linearity. An array of these sensors can be miniaturized to integrate with commercial endoscope graspers.

Acknowledgments

I bow myself in the grace of God “Waheguru”, I pray to the Almighty God for being in good health and condition, and for the successful completion of my masters. I pray to his greatness to inspire me the right path to his content and to enable me to conclude my work.

With a deep sense of gratitude, I wish to express my sincere thanks to both of my supervisors, Dr. Javad Daraghi and Dr. Ramin Sedaghati, for their immense help in planning and executing the works in time. Their company and assurance at the time of crisis would be remembered lifelong. The cooperation I received from other faculty members of mechanical engineering department is gratefully acknowledged.

I wish I would never forget the company I had from my fellow research scholars of my department at concave research center and my roommates. In particular, I am thankful to Arlene Zimmerman, Jose Esteves, Sophie and Jue Hulet for their helping hands and cooperation.

I express gratitude to my parents “Dr. Kuldeep Singh and Sukjit Kaur”, who taught me the values of the hard work, patience by their own experiences. In spite of all my efforts and work I can never pay invaluable debt of my grand parents “S. & Sr. Bhagwan Singh Pannu”. I would like to share this moment with my father, mother and brother. I am heartily pay reverence to my elder brother Mr. Gurpiyar Singh for his moral support and guidance. Finally, I would like to thank all whose direct and indirect support helped me for completing my thesis.

Harpiyar Singh

TABLE OF CONTENTS

i.	List of Figures	x
ii.	List of Tables	xiv
iii.	List of Acronyms and Symbols	xviii
		Page
Chapter 1	Introduction	
1.1.	Introduction	1
1.2.	Tactile Sensation	4
1.3.	Softness of Tissue	9
1.4.	Present Study	11
1.5.	Overview of Thesis	12
Chapter 2	Tactile Sensing Devices	
2.1.	Sensor Characteristics	15
2.1.1.	Signal to Noise Ratio (SNR)	15
2.1.2.	Force Sensitivity	16
2.1.3.	Spatial Resolution	16
2.1.4.	Frequency Response	16
2.1.5.	Linearity	17
2.1.6.	Temperature Variation	17
2.2.	Technologies For Tactile Sensing	18
2.2.1.	Capacitive Sensors	18
2.2.2.	Conductive Polymers	20

2.2.3. Inductive Displacement Sensors	22
2.2.4. Magneto resistive Force Sensors (MR)	22
2.2.5. Optical Sensors	23
2.2.6. Strain Gage Sensors	25
2.2.7. Piezoelectric Sensors	29
2.3. Selection and Decision	32
 Chapter 3 Design of Piezoelectric Sensor	
3.1. Single Sensor Design	36
3.1.1. Design of Plates	37
3.1.2. Design of PVDF Films	38
3.1.2.1. PVDF-1 Design	39
3.1.2.2. PVDF-2 Design	40
3.1.3. Rigid Cylinder Design	41
3.1.4. Compliant Cylinder Design	42
3.1.5. Sensed Object Design	43
3.1.6. Single Sensor Assembly	43
3.2. Two Sensor Design	45
3.2.1. Two Sensor with Different Base Plates	45
3.2.2. Two Sensor with Common Base Plates	46
 Chapter 4 Numerical Simulation and Comparison	
4.1. Finite Element Formulation	48
4.2. Analysis in ANSYS	58

4.3. Design of Grasper with Different Base	63
4.3.1. Limitation of Design of endoscope Grasper with Different Base	67
4.4. Design of Grasper with Common Base plate	67
4.5 Comparison of Theoretical Results	72
4.5.1 Comparison of 2D Model with 3D Model	72
4.5.2 Comparison of Two Sensor on the Different and Common Base Plate	77
4.5.3 Comparison of the Single Sensor and Two Sensor with Common Base	78
4.6. Novelty of Design	80
 Chapter 5 Experimental results and Comparison	
5.1. Experimental Analysis	81
5.2. Calibration of the Load cell	83
5.3. Measurement of Modulus of elasticity	84
5.4. Experimental Results	87
5.4.1. Single Sensor	88
5.4.2. Two Sensors with Common Base	90
5.4.3. Two Sensors with Different Base	91
5.5 Comparison of the Experimental Results	93
5.5.1. Comparison of the Experimental and Theoretical results for Single sensor	95
5.5.2. Comparison of the Experimental and Theoretical Results for	

Common Base Sensor	96
5.5.3. Comparison of the Experimental and Theoretical Results for	
Different Base Sensor	99
Chapter 6 Conclusions and Recommendations	
6.1 Conclusions	103
6.2 Recommendations for Future Work	105
Bibliography	108
Appendix I	
Piezoelectric Effect	115
Appendix II	
Program of Simulation and Data Obtained	128
Appendix III	
Interfacing with Electronics	147

List of Figures

Figure	Page
1.1 Close up view of the zeus robots operating on a model heart	3
1.2 Endoscopic grasper integrated with tooth-like tactile sensor	7
2.1 Variable capacitance force transducer	19
2.2 Capacitive type sensor for measuring the force	20
2.3 Conductive polymer sensor is based on the change in resistivity	21
2.4 Optical sensor, measures the light intensity between emitter and receiver	25
2.5 Strain gage type sensor based on the change of physical geometry	28
2.6 Voltage generation by the piezoelectric substance	31
2.7 Ultrasound sensor consists of PVDF films on the opposite sides rubber	32
3.1 Complete assembly of the single sensor	36
3.2 Design of base plate for single sensor	38
3.3 PVDF-1 film of design with both sides metallized	40
3.4 PVDF-2 Film metallized both sides	41
3.5 Rigid cylinder made up of phenolic	42
3.6 Compliant cylinder made up of soft rubber	43
3.7 Assembly of single sensor	44

3.8	Assembly of two sensors on different base	46
3.9	Assembly of two sensors on common base	47
4.1a	Geometrical model of the single sensor	49
4.1b	Fabricated single sensor	49
4.2	Finite element model for single tactile sensor	50
4.3	Two degrees of freedom model	54
4.4	Variation of the force ratio with the lambda function	57
4.5	Different types of elements used for meshing	59
4.6	Meshed single sensor with assigned elements	59
4.7	Force ration versus λ for 2D and 3D model	61
4.8	The Effect of modulus of elasticity of sensed object on the force ratio at two different sets of compliant cylinder	62
4.9	The design of the two sensors mounted on the different base plates	64
4.10	The Effect of modulus of elasticity of sensed object on the force ratio of grasper with two sensors having different base at two different sets of compliant cylinder	66
4.11a	The Design of the two sensors mounted on the common base plates	69
4.11b	Photograph of the manufactured common base sensor	69
4.12	Effect of modulus of elasticity of sensed object on the force ratio of grasper with two sensors having common base at two different sets of compliant cylinder	71

4.13	Variation of force ratio with modulus of elasticity of sensed object at compliance of the cylinder 2.4×10^4	74
4.14	Variation of force ratio with modulus of elasticity of sensed object at compliance of cylinder 3.3×10^4 .	75
4.15	Variation of force ratio with modulus of elasticity of sensed object at two sets of compliant cylinders.	76
4.16	Comparison of two sensors on common base and different base plates	78
4.17	Effect of Modulus of elasticity of sensed object on the force ratio for single sensor and double sensor mounted on the common base	79
4.18	Single sensor acts as teeth	80
5.1a	Layout for the experimental setup for measuring the response of the tactile sensor under dynamic loading	82
5.1b	Layout for the experimental setup for measuring the response of the tactile sensor under dynamic loading	83
5.2	Expected order of the softness of the sample depending on the technical data by manufacturer	87
5.3	Softness of the sample depending on the experimental results obtained from single sensor	89
5.4	Softness of the sample depending on the experimental results, for common base	91
5.5	Softness of the sample depending on the experimental results, for different base	93
5.6	Comparison of the experimental results between single sensor, common base and different base sensor	94

base and different base sensor.

5.7	Comparison of the experimental results with 2D model and 3D model for single sensor	96
5.8	Comparison of the experimental results with 3D model for common base sensor	98
5.9	Comparison of the experimental results with 3D model for different base sensor	100
A1.1	Piezoelectric in ionic crystals such as quartz, ion position in quartz lattice with and without applied stress	115
A1.2	Figure A1.2 Voltage generation by the piezoelectric substance	125
A3.1	PVDF Film act as Capacitor with Aluminum Coating	147
A3.2	Electrical Equivalent Circuit for Sensor	147
A3.3	Purpose of Load Resistance	148
A3.4	Charger Amplifier and Voltage Amplifier	149
A3.5	Circuit Diagram of the Wheat stone bridge	150

List of Tables

Table	Page
2.1 Comparison of the different sensor technologies used for measuring Force.	34
3.1 The properties of the plexiglas.	37
3.2 Properties of the PVDF films	39
4.1 Voltage generation and force distribution on the rigid cylinder of single sensor at the compliance of cylinder 2.4×10^4 .	60
4.2 Voltage generation and force distribution on the rigid cylinder of single sensor at the compliance of cylinder 3.3×10^4 .	60
4.3 Voltages generation and forces distribution on the two circular PVDF films in different base model with compliance cylinder modulus of $2.4 \times 10^4 \text{ N/m}^2$.	65
4.4 Voltages generation and forces distribution on the two circular PVDF films in different base model with compliance cylinder modulus of $3.3 \times 10^4 \text{ N/m}^2$.	66
4.5 Voltages generation and forces distribution on the two circular PVDF films in common base model with compliance cylinder modulus of $2.4 \times 10^4 \text{ N/m}^2$.	70
4.6 Voltages generation and forces distribution on the two circular PVDF films in common base model with compliance cylinder modulus of $3.3 \times 10^4 \text{ N/m}^2$.	70
5.1 Calibration data for the Strain Indicator	84

5.2	Experimental results of the modulus of elasticity for the white silicon rubber, sample 1.	86
5.3	Experimental results of the modulus of elasticity for the unknown sample of rubber, sample 6.	86
5.4	Physical properties of the rubber specimens provided by the manufacturer.	86
5.5	Experimental results for single sensor at the 3N of load with different rubber samples	89
5.6	Experimental results at the 3N of load with different samples of the rubbers, for common base sensor	91
5.7	Experimental results at the 3N of load with different samples of the rubbers, for different base sensor	92
5.8	Calculated percentage error in the experimental results	97
A2.1	Voltage generation and force distribution on the rigid cylinder of single sensor at the compliance of cylinder 2.4×10^4	130
A2.2	Voltage generation and force distribution on the rigid cylinder of single sensor at the compliance of cylinder 3.3×10^4	131
A2.3	Voltages generation and forces distribution on the two circular PVDF films in common base model at compliance of 2.4×10^4 of outer cylinders	132
A2.4	Voltages generation and forces distribution on the two circular PVDF films in common base model at compliance of 3.3×10^4 of outer cylinders	134

A2.5	Voltages generation and forces distribution on the two circular PVDF films in different base model at compliance of 2.4×10^4 of outer cylinders.	135
A2.6	Voltages generation and forces distribution on the two circular PVDF films in different base model at compliance of 3.3×10^4 of outer cylinders.	136
A2.7	Effect of different positions of force applied along x-axis on the force-ratio in sensor with common base.	138
A2.8	Effect of different positions of force applied along the x-axis on the force ratio, for sensor with different base.	139
A2.9	Experimental data for the single sensor at six different load sets for sample 1	140
A2.10	Experimental data for the single sensor at six different load sets for sample 2	140
A2.11	Experimental data for the single sensor at six different load sets for sample 3	140
A2.12	Experimental data for the single sensor at six different load sets for sample 4	141
A2.13	Experimental data for the single sensor at six different load sets for sample 5	141
A2.14	Experimental data for the single sensor at six different load sets for sample 6	141
A2.15	Experimental data for the two sensors on the common base, at the different load sets, sample 1	142

A2.16	Experimental data for the two sensors on the common base, at the different load sets, sample 2	142
A2.17	Experimental data for the two sensors on the common base, at the different load sets, sample 3	142
A2.18	Experimental data for the two sensors on the common base, at the different load sets, sample 4	143
A2.19	Experimental data for the two sensors on the common base, at the different load sets, sample 5	143
A2.20	Experimental data for the two sensors on the common base, at the Different load sets, sample 6	143
A2.21	Experimental data for the two sensors on the different base arrangement, At the different load sets, sample 1	144
A2.22	Experimental data for the two sensors on the different base arrangement, At the different load sets, sample 2	144
A2.23	Experimental data for the two sensors on the different base arrangement, At the different load sets, sample 3	145
A2.24	Experimental data for the two sensors on the different base arrangement, At the different load sets, sample 4	145
A2.25	Experimental data for the two sensors on the different base arrangement, At the different load sets, sample 5	146
A2.26	Experimental data for the two sensors on the different base arrangement, At the different load sets, sample 6	146

List of Acronyms and Symbols

[B]	Double Differential of Shape function Matrix
[B _e]	Derivative of Shape function for Potential
[B _u]	Strain Nodal Displacement Matrix
[c]	Elasticity Matrix (N/m ²)
[e]	Piezoelectric Matrix at Constant Stress (C/m ²)
[ε]	Dielectric Matrix
[k]	Element Stiffness Matrix
[K]	Stiffness Matrix for System
[K _{beam}]	Stiffness Matrix for Beam Element
[K _{ee}]	Dielectric Stiffness Matrix
[K _{elastic foundation}]	Stiffness Matrix for Elastic foundation
[K _{eu}] , [K _{ue}]	Piezoelectric Stiffness Matrix
[K _{uu}]	Structural Matrix
[N]	Shape Function Matrix
[N _x],[N _y],[N _z]	Derivative of Shape Function Respect to X,Y,Z
{F}	Force Vector for System
{d}	Element Nodal Displacement Vector
{D}	Electric Flux Density (C/m ²)

$\{E\}$	Electric Field Vector (V/m)
$\{f\}$	Element Nodal Force Vector
$\{S\}$	Strain Vector (Dimensionless)
$\{T\}$	Stress Vector (N/m ²)
$\{U\}$	Displacement Vector for System
A	Area Ratio
A_a	Area of Rigid Cylinder
A_b	Area of Compliant Cylinder
C	Capacitance
CCD	Charge coupled device
1-D, 2-D	One Dimensional, Two Dimensional
d_{31}, d_{32}, d_{33}	Piezo Coefficient Related to the Charger (C/N)
DC	Direct current
$\Delta L'$	Change in length of the Strain Gage
DOF	Degree of Freedom
$\Delta R'$	Change in Resistance of Strain Gage
E	Modulus of Elasticity
e	Piezoelectric Coefficient (C/m ²)
E_1	Modulus of Elasticity Sensed object

E_2	Modulus of Elasticity Compliant cylinder
E_x, E_y, E_z	Electrical field in X,Y,Z Direction
$F_1, F_2, F_3, F_4, F_5, F_6$	Force applied on Element 1,2
FREG	Force feed Back Endoscopic Grasper
FRS	Force Sensing Resistor
g_{31}, g_{32}, g_{33}	Piezo Coefficient Related to the Voltage (V-m/N)
GF	Gage Factor
GMR	Giant Magnetoresistive
I	Second Moment of Inertia
ϕ	Nodal Potential
K_f	Spring Constant Per unit length
K_{f1}	Stiffness of Sensed Object
K_{f2}	Stiffness of sensed object above Compliant
K_{f3}	Stiffness of compliant Cylinder
L	Length of the Plate
λ	Lambda Function
L'	Length of the Strain Gage
LED	Light Emitting Diode
LVDT	Linear Variable Differential Transformer

MEMS	Micro Electro Mechanical Systems
MIS	Minimal Invasive Surgery
MR	Magnetoresistive
P	Uniform Applied load
Π	Potential Energy
PVDF	Polyvinylidene Fluoride
PZT	Lead Zirconate Titanate
Q	Charge
R	Radius of the Rigid Cylinder
ρ	Density
R'	Resistance
R_1	Inner Radius of the Compliant Cylinder
R_2	Outer Radius of the Compliant Cylinder
RTV	Room temperature Vulcanization
SNR	Signal to Noise ratio
T	Thickness of Plate
t	Gap between the electrodes
T_1	Thickness of Sensed object
T_2	Rigid and Compliant Cylinder Height

u, v, w	deflection in X,Y,Z axis
$U_1, U_2, U_3, U_4, U_5, U_6$	Degree of Freedom for Element 1,2
V	Voltage
$v(x)$	Displacement function
W	Width of Piezoelectric crystal
τ	Time Constant

Chapter 1

Introduction

1.1 Introduction

Minimally Invasive Surgery (MIS) is a revolutionary surgical technique. In the minimally invasive surgery, the surgery is performed with the instruments and viewing equipment inserted through small incisions rather than by making a large incision to expose and provide access to the operation site. The main advantage of this technique is the reduced trauma to healthy tissues, which is a leading cause for patient post-operative pain and long hospital stay. The less hospital stay and rest periods reduce the cost of operation. Therefore procedure costs, can be significantly reduced with MIS. However MIS procedures are more demanding on the surgeon, requiring more difficult surgical techniques. The instruments used in MIS have only four degrees of freedom through the entry port, preventing the ability to arbitrarily orient the instrument tip. Dexterity is significantly reduced because of the lost degree of freedom and motion reversal due to the friction effect at the entry point. Force feedback reduces, due to the friction at the inflated airtight abdominal wall. There is no tactile sensing on which surgeon can highly depend in surgery to locate arteries and tumors hidden in the tissue. Also, softness of the tissue cannot be judged during the operation using ordinary instruments. Three fundamentals have to be fulfilled to optimize minimally invasive surgery: three-dimensional imaging, actuation maneuverability of instrument and sensorial feedback.

For better control of instrument and the operative procedure, tactile feedback can be obtained with help of microsensor.

Minimally invasive surgery (MIS) operations include laparoscopy (abdominal cavity), thoracoscopy (chest cavity), arthroscopy (joints), ophthalmic microsurgery (eyes) etc. In 1985, Muhe, a German scientist, performed the first major laparoscopy surgery for cholecystectomy (removal of gall bladder). In less than a decade, there was a quick shift from open surgery to laparoscopic surgery in the United States of America, 1993 [1]. Adoption of laparoscopic techniques has been slower in more complex procedures, largely because of the greater difficulty due to the surgeon's reduced dexterity and perception.

To perform the MIS more effectively, the surgeon should be able to feel the tissue, sense the pressure of blood vessels and ducts during the procedure. This ability is very important during manipulation tasks such as the grasping of the internal organs, gentle load transfer during lifting, suturing and removing tissues. The need to feel the tissue and its softness is particularly important during operation. In MIS surgery, stereoscope vision and tactile information about tissue consistency are no longer available to the surgeon. To compensate for these sensory deficits, various tissues can be characterized with an electromechanical sensor that records their properties. In future, these sensors will be integrated with surgical instruments, providing the surgeon with information about tactile properties of tissue.

Surgery is perhaps the most exciting and rapidly developing area where tactile sensing is actually of central importance. Minimally Invasive Surgery is only 18 years old and now routinely used as the preferred choice of patients and doctors for many

operations. However, despite its advantages, MIS severely reduces the surgeon's sensory perception during the manipulation. Minimally invasive surgery is based on a visual and tactile experience and any limitation on the surgeon's sensory abilities is most undesirable.

In laparoscopy, long slender tools are inserted through small puncture openings in the abdominal wall and the surgeon uses a range of tip-mounted instruments guided by video feedback images. As the instruments are rigid rods and effectively have fixed pivots at the entry points, the available degrees of freedom are restricted and therefore demand extra operator expertise. Figure 1.1 shown the endoscopic surgery performed on the heart model designed by the zeus robotics [61]. This model consists of the camera and endoscopic instruments. Different equipments are used for performing the different operation like suturing, cutting. The Zeus robotic surgical system operated by computer used in thoracoscopic and coronary artery bypass grafting procedures.

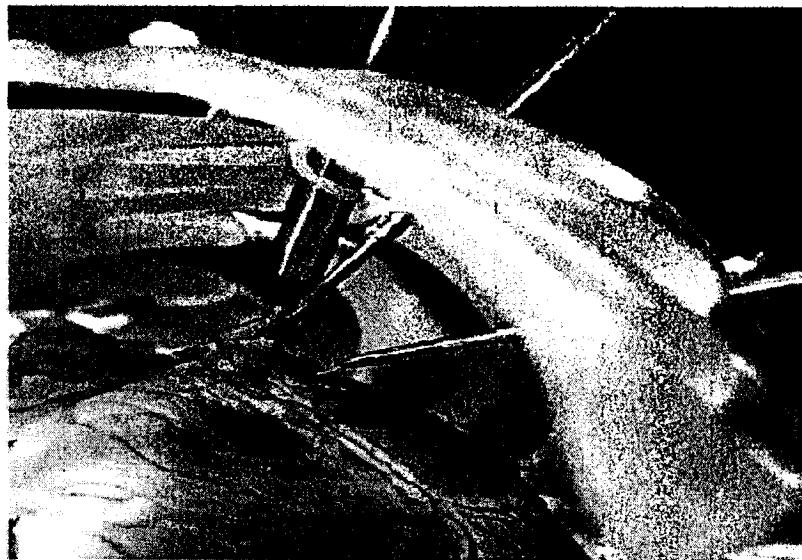


Figure 1.1 Close up view of the zeus robots operating on a model heart.

Voges [2] reports on the main difficulties experienced in MIS. These difficulties are: restricted manipulation mobility, lack of depth from 2D vision and the almost complete lack of a sense of touch. The relevance of tele-presence is clear and Voges predicts that future systems will have new designs of flexible instruments with greater mobility, force reflection, 3D monitoring and data enhancement. It is clear that tactile sensing is greatly needed in this area and researchers are responding to the opportunity.

1.2 Tactile Sensation

Tactile sensing is defined as continuous sensing of variable contact forces. The tactile sensation may be defined as sensing ability of human finger (force, hardness, temperature, and roughness). The reason that tactile sensing is so important in MIS surgery is that, soft tissue can only be properly examined and identified by assessing its softness, viscosity and elasticity properties. The palpation of tissues and organs is an essential procedure that surgeons value highly. One of the limitations of the present day MIS using laparoscopic tools is lack of tactile sensitivity, which causes a loss of surgeon's palpation evaluation capability and also tissue compliance. Surface texture and roughness perception of various tissues are also important for inspecting the texture of tissue by endoscopic grasper during MIS surgery. Texture perception is different from roughness. To find out the surface texture perception, the tactile sensor must be capable of measuring the roughness, compliance and viscoelastic behavior. Since tissue is viscoelastic and behaves non-linearly, sensor must be capable of measuring compliance as function of time so that the viscoelastic properties of the tissue can be ascertained.

Extensive investigation has been performed for tactile perception of the tissue during minimal invasive surgery. Surgeons have been known to insert their fingers through the access openings during MIS simply to perform direct tactile exploration [3]. Dario's short but far-sighted review [4] cites medical applications in which the hardness of soft tissues is detected through palpation. Bicchi et. al. [5] gives a good description of the issues in MIS and describes an experiment with a modified commercial instrument to sense force using strain gauge. LED-optical detector was used for positioning. They measured the compliance and viscoelastic properties of tissue using a sensorized laparoscopic device by measuring the grasper force and its angular displacement. Bicchi et. al. [5] have discussed capacitive tactile sensor and associated tactile display used in MIS. By correlating force against deformation, the system was able to identify five objects of different elastic properties.

An experiment with a sensor for laparoscopic attachment has been described by Fischer et. al. [6]. A 64-point sensor of area 1 cm^2 was connected to a fingertip for vibrotaction display.

The ultrasonic tactile method is entirely non-destructive in its use as a sensor. A microrobot was designed for colonoscopy using a pneumatic inchworm propulsion method described by Dario et. al. [7]. The difficulties of adopting totally autonomous robotic systems in surgery are discussed by Howe et. al. [8] and an approach is developed where the surgeon maintains supervision and control but is constrained from driving the cutting tools outside force limited regions.

Cohn et. al. [9] performed a series of designs for endoscopic and laparoscopic tools. An interesting idea raised here is the possibility of using the capacitive tactile

sensor, not to measure applied force, but to detect the varying dielectric permittivity of different tissues. They suggest that water, fat, blood vessels, and cancerous tissue might all be discriminated by this means. A striking feature of the design of Mitani et. al. [10] is that it uses disposable kit with the help of inexpensive materials. In this case, sensing head is replaced for each patient. This aspect is very important for medical sensors to avoid infection and transmitted diseases.

Gray and Fearing [11] have reported on an array of microtactile capacitive sensors used in endoscopic-surgery telemanipulator to test sensing of the organic tissue on the small scale. Eight by eight tactile capacitive array sensors were used for detection of sub-millimeter features and objects, where the entire sensor array is smaller than normal human spatial resolution of 1mm. The sensor has capability of detecting millinewton forces and good interpolation between elements. The sensors had severe hysteresis problems, but no detectable proximity effects. Due to hysteresis problem the results have not been reliable.

Mehta [12] has designed and fabricated a capacitive micromachined endoscopic tooth-like pressure sensor. But the sensor can only measure a few grams of the applied force and secondly there is no provision available to measure the compliance of tissue. Dargahi et. al. [13] has designed and fabricated a micro machined robust piezoelectric endoscopic tooth like tactile sensor with good linearity and a high dynamic response. Sensor may be damaged due to application of shear stress along the sensor while handling the tissue. The sensor lacks DC response due to the nature of the PVDF films. Piezoelectric tooth like tactile sensors are mounted in the form of arrays on the endoscope for measuring the force as shown in the Figure 1.2.

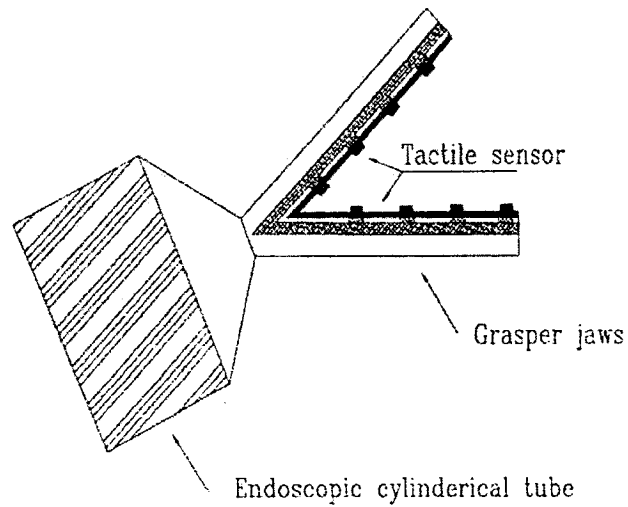


Figure 1.2 Endoscopic grasper integrated with a tooth-like tactile sensor

Dario et. al. [14] have constructed a tactile sensor, which can distinguish amongst various compliant objects. However their work lacks any theoretical basis. Silva et. al. [15] developed the strain gauge type tactile sensor for measuring the finger force. It was constructed using metallic strain gauges. It is rugged and has a linear response. It also provides good repeatability, resolution of 0.3 N, low hysteresis and sensitivity of 0.12 V/N. However their design is not suitable for measuring the compliance of the sensed object.

Shinoda et. al. [16] have designed the acoustic cell ultrasonic sensing matrix which are placed face to face. They mounted this sensor on a robot finger with 5 degrees of freedom. Designed sensor was able to measure minimum of 10 μ m displacement by 18.5 mm cell height and 0.001 rad change in surface inclination. This sensor can also measure contact force and slip of the grasped object as well.

Dargahi et. al. [17] developed a prototype for tactile sensing system with only three PVDF sensing elements. The magnitude and position of force is obtained by using triangulation approach combined with membrane stress. The lack of agreement between theoretical and experimental results could be attributed both to the experimental errors and the assumption in the theoretical analysis. Ohka et. al. [18] developed the optical tactile sensor equipped with an optical wave guide plate mounted on a robot manipulator. The experimental results confirmed that the tactile sensor is capable of detecting the distribution of three-axial forces and they were in good agreement with the theoretical results. This tactile sensor comprised a CCD camera, light source, an acrylic board and a silicon rubber sheet that are assembled into a casing. Thus it is very difficult to miniaturize it.

Obana et. al. [19] designed a semiconductor strain gauge tactile transducer. It was designed with the goal of measuring finger force without affecting the hand dexterity. Semiconductor strain gage was used due to its small size and high sensitivity. The transducer has both dynamic and static responses with negligible hysteresis and good linearity. Force sensitivity was 0.05 V/N. This sensor is ideal for measuring the force applied on the tissue. However it is capable to measure the softness of tissue in-order to avoid tissue damage. Howe et. al. [8] also designed capacitive tactile array sensor which is based on an earlier design of Fearing [3]. This device measures the pressure distribution at the contact between the robot hand and the grasped object. Experiments confirmed the system's ability to convey significant contact information.

Shimizu et. al. [20] have developed a new sensor for measuring the contact force and hardness of the object. It is made up of piezo-resistive displacement sensor on the

diaphragm, and a chamber for pneumatical actuation. They theoretically analyzed the operation of the tactile sensor, and designed its specifications for a device to detect the contact force and human hand touch. Payandeh et. al. [21] designed haptic interface for endosurgery. The design consists of tunable spring based on the haptic and surgical requirements. Simulation and experimental results demonstrate the practicality of such design concept.

1.3 Softness of Tissue

While performing the minimally invasive surgery it is also necessary to know the properties of the tissue and the force acting on the tissue. Many different layouts were proposed and designed to examine the tissues behavior while performing minimal invasive surgery. Hutter et. al. [22] discussed the modeling of soft tissue deformation for laparoscopic surgery simulation. The work was mainly based on virtual reality surgical simulator for real time and finite element simulation of elastic tissue deformation in complex systems.

Chen et. al. [23] measured Young's modulus of soft tissue using elasticity imaging. A simple 1-D ultrasound elasticity measurements were performed and good accuracy and consistency with mechanical measurement were established. The exponential shape of the stress-strain curve was observed. Correction factor for constrained and unconstrained cases for different Poisson's ratio were also discussed in this study. Similar method was employed for reconstructive elasticity imaging of large deformations using ultrasonic displacement and strain images [24]. Estimation of shear modulus distribution in soft tissue from strain distribution were performed by Sumi et. al.

[25]. Tissue was considered as a linear isotropic incompressible elastic body. Mathematical formulation was used to calculate the shear modulus.

Brouwer et. al. [26] measured the soft tissue properties for haptic modeling in surgical simulation which will be useful in designing of virtual environment and teleoperated systems for surgery. The properties of tissue were measured both in-vivo and ex-vivo conditions. Five tissues and task (cutting, stretching, and spreading) combination were performed on the pigs prior to the experiments for other research. The results obtained have shown excellent exponential behaviors. Similar type of work was carried-out for in-vivo data acquisition [27]. An instrument (TeMPeST 1-D) was designed for measuring force displacement response in-vivo. This also permits investigation in viscoelastic and non-linear properties of in-vivo tissue. Two aspects were covered in this study to provide highly realistic simulation of laparoscopic surgery and developing instruments, which can measure the mechanical properties of tissue in-vivo.

Chail et. al. [28] designed the haptic scissor for the cutting biological tissues. Simulation of haptic scissor gave simple and computationally efficient results. Different experiments were performed on the different real and virtual models of tissues. Rosen et. al. [29-30] designed an endoscope virtual reality surgical training simulator using haptic devices. For designing the simulator biomechanical properties of soft tissue are also very essential. This simulator can help novice surgeons for more dexterity on the use of endoscope instruments. Simulator also evaluates the surgical skills. The Markov Modeling (MM) and force controlled endoscopic grasper for minimally invasive surgery were used in this endoscopic simulator. Different setups were used to compare the skills

with the help of force torque sensor. Force feedback endoscopic grasper (FREG) was developed with computer control and a haptic user interface.

1.4 Present Study

The present thesis constitutes a proof-of-concept design of a piezoelectric tactile sensor (mainly used in the endoscopic grasper) capable of measuring the force and compliance of the tissue in order to increase the dexterity of the surgeon during MIS. Present day endoscopic graspers are designed tooth-like in order to grasp slippery tissues. However they are not equipped with tactile sensors to measure the compliance of tissue.

The proposed tactile sensor consists of rigid and compliant cylindrical elements. Determination of the compliance of the sensed objects is based on the relative deformation of contact object/tissue on the compliant and rigid element of the sensor. The Polyvinylidene Fluoride (PVDF) film sandwiched between rigid cylinder and plate and also between the two base plates has been used to measure the force applied on the rigid element and the total force applied on the sensor, respectively. A two-dimensional finite element model has been developed for a single sensor. In the proposed finite element model the sensed object and compliant cylindrical element have been modeled on the elastic foundation, respectively. Moreover a 3D finite element model of the single sensor has been developed using ANSYS software and the results have been compared with 2D formulation.

A prototype of the sensor has been fabricated and extensive experimental study have been performed to investigate the performance of the proposed sensor and validate the theoretical results.

The arrays of the sensor have also been designed in the form of common base plates and different base plates arrangement. The main objectives of the present study are summarized as follows:

1. To Design, fabricate, and test a prototype PVDF tactile force sensor for measuring the compliance of objects/tissues
2. To develop a Finite element model of the sensor in 2D and 3D
3. To compare the theoretical and experimental results obtained from the single sensor, common base sensor, and different base sensor.

1.5 Overview of the Thesis

The present thesis consists of six chapters. Chapter 1 introduces an overview of MIS methods. The most important and relevant contributions to the field of tactile sensation to date and thorough review on the softness of the tissue are presented in this Chapter. The chapter concludes by identifying the main objectives of the present study and the layout of the thesis.

Different tactile sensing devices are discussed in Chapter 2. The sensor characteristics i.e. signal to noise ratio (SNR), sensitivity, temperature drift are also described in this section. Finally the selection and decision for using the piezoelectric sensor are addressed.

Chapter 3 presents the design of the sensors. The single sensor design was discussed with properties of materials used during the fabrication. Then design of the two sensors mounted on the grasper with common base and different base, respectively were discussed. The manufacturing and fabrication stages of the sensors were also presented.

The three different sensors with different arrangements were fabricated using plexi-glass, phenolic and PVDF films. The purpose of non-conductive and conductive glue, used for assembling the system together, is also discussed.

Chapter 4 explains the analytical study of the sensors. The 2D and 3D design of the single sensor were discussed using mathematical approach and simulation in ANSYS, respectively. The simulation in ANSYS is further extended for the common base and different base sensor. Towards the end of the chapter the limitations of different base sensor are addressed and the results obtained from 2D, 3D and the simulation of three different sensors are compared.

In Chapter 5, the experimental setup, calibration of the instruments and procedure used for the data acquisition are discussed. At the end of the chapter the experimental and theoretical results are compared. The comparison of single sensor, common base sensor and different base sensor is also compared pictorially.

In Chapter 6 the conclusion and summary of the theoretical and experimental work are presented. The drawbacks of sensors with future suggestion and recommendation are also discussed.

At the end of dissertation, Appendices are provided to enhance and cover more related aspect to the thesis. The Appendix I discusses about the piezoelectricity and finite element formulation for the piezoelectric substance. The properties and behavior of the PVDF materials are presented in this Appendix. Analytical approach of the PVDF film is also discussed. Appendix II provides computer programs and data obtained from ANSYS. Finally, Appendix III explains about the interfacing with electronic circuits for signal amplification.

Chapter 2

Tactile Sensing Devices

The measuring of the force is the main task to find the compliance of the tissue and force on the tissue. Different parameters have been used to measure the force. The force sensors have been designed depending on their requirement and application. The advantages and disadvantage of the different force measuring devices are discussed in this section and also the selection criterion is addressed. The piezoelectric sensor is preferred over all other sensors for tactile sensing. Tactile sensing implies the detection of wide range of local parameters affected by contact. The most important factors among those contact-based effects are contact stresses, slippage, heat transfer and hardness.

Before proposing the viable solution that could enhance tactile sensation, it is realized that the potential force sensing modalities required to be first properly explored. Force can be measured by measuring alteration of other properties of sensor. In some sensors, electrical and structural properties have been used as the parameters to measure the force. The electrical resistance might increase while in others current might be generated. As the size of the sensor is very small, it is very difficult to measure the structural deformation, so structural properties are measured with the changes in the electrical properties. Sensor is required to be a part of the transducer systems before these properties changes can be realized. A transducer system is a device that senses either the absolute value or changes in some physical quantities, such as force or strain, which converts the quantity into an electrical signal that can be used for measurement. The

characteristics of the sensors currently used for measuring the force and pressure are discussed in the following sections.

2.1 Sensor Characteristics

The present study is mainly concerned with the sensing force between the endoscopic grasper and tissue. Sensor should be capable of measuring the compliance of the tissue. Different technologies have been used to measure the tactile sensing. This is very important since artificial tactile sensors are going to be used to augment the human dexterity. Dario et. al. [14] discussed the sensing body structure by an advanced robotic system. The skin-like sensing and positioning model with the help of piezoelectric polymer were proposed. Some important specification were used to evaluate the tactile sensing, like signal to noise ratio, frequency response, spatial resolution, temperature drift, force sensitivity, dynamic range, and linearity [31].

2.1.1 Signal-to-Noise ratio (SNR)

It is the ratio of the amplitude of the desirable signal to the amplitude of noise signal (undesirable signal) at a given point in time. SNR is expressed as 20 times the logarithm of the amplitude ratio, or 10 times the logarithm of the power ratio. SNR is usually expressed in dB and in terms of peak values for impulse noise and root-mean-square values for random noise. In defining or specifying the SNR, both the signal and noise should be characterized, *e.g.*, peak-signal-to-peak-noise ratio, in order to avoid ambiguity. Sensors can be characterized by their electrical impedance [32]. Electrical impedance takes four main simple forms: resistive, capacitive, inductive and resonant.

The performance of the sensor depends on the noise signal embedded in the signal. This is one of the fundamental parameter of sensor performance.

2.1.2 Force Sensitivity

The force sensitivity is an important feature for instruments measuring very small force. The sensitivity of the sensor depends on the rate of change of output with respect to the input. The higher the sensitivity gives the higher precision and resolution power to the sensor. Sensitivity values generally required for tactile sensor are between 0.5×10^{-2} - 1×10^{-2} N [33].

2.1.3 Spatial Resolution

In tactile sensing, space constraint plays a significant role for designing the sensor. The sensor should be attuned to the space available without compromising the results. The size of single sensor (tactel) is generally 1 to 2 mm.

2.1.4 Frequency Response

The frequency or dynamic response is another property that needs to be considered for selecting the sensor. When the input or the force applied to the sensor is not static and it varies with time, it is known as dynamic input. In that case, sensor must be compatible to measure the dynamic responses. By using dynamic response of sensor, veins pulse can be located and thus damaging of vein could be avoided. Piezoelectric sensors are very sensitive to dynamic response. The ideal frequency response for the

robotics finger is from DC to 20 Hz [34]. The practical application suggests that the frequency response varies from dc to very low frequency ($<10\text{Hz}$). The sensor with good static and low dynamic response is preferred.

2.1.5 Linearity

A sensor is said to be linear when input/output relation follows straight line, i.e. output is proportional to the input. The slope of the line gives the sensitivity of the sensor [35]. The human sensory system lacks linearity due to the viscoelastic nature of tissue. Using sensor with good linear response would give more precise magnitude values. It is easy to formulate relation between the input and output, and also easy to calibration.

2.1.6 Temperature Variation

The variation of the temperature causes change in the properties of the transducer, which gives erroneous results. So the sensor output is required to be independent from the temperature drift. Mostly the sensors are designed at the temperature of application. It is preferred that even small change in temperature would not affect the sensor functionality drastically.

All the above properties of sensor are discussed while focusing on the functionality of the sensor. But the viability of the sensor also depends on the physical shape, ruggedness, installation and financial constraints. Summarizing the requirements of the sensor, it can be concluded that sensor should be inexpensive, reliable, no hysteresis and durable.

2.2 Technologies for Tactile Sensing

Technologies for tactile sensing mostly differ from one another by the transduction method. The transduction methods are concerned with change in resistance, capacitance, voltage generation, inductance and optical properties. Some methods are very suitable for clinical applications. The main sensor transduction methods that are used in this arena are capacitive, magnetic, inductive, conductive elastomeric, optical, strain gage sensor and piezoelectric. All these transduction methods for the tactile sensation are discussed in the following sections.

2.2.1 Capacitive Sensors

Tactile sensors within this category are concerned with the measuring capacitance, which varies under applied load. The capacitance of the parallel-plate capacitor depends on the separation of plate, permittivity of dielectric materials and their areas. These sensors are provided with elastomers separator between plates that provide compliance to capacitance according to the applied load. Capacitance type pressure sensors can detect the touch by sensing the normal or tangential force, but is very difficult to differentiate between two forces from output of signal [36].

The force could be measured by simply making one plate as diaphragm. When the force is applied to the diaphragm, the distance between two plates decreases, thus it increases the capacitance. The inverse gap relationship is highly nonlinear and the sensitivity drops significantly with larger gaps. The advantages of this type of sensor are wide dynamic range, robustness and linear response. On the other hand, it also exhibits

some disadvantages like susceptibility to noise; temperature drift and capacitance decrease with size of sensor. The basic diagram of the capacitive sensor is demonstrated in Figure 2.1.

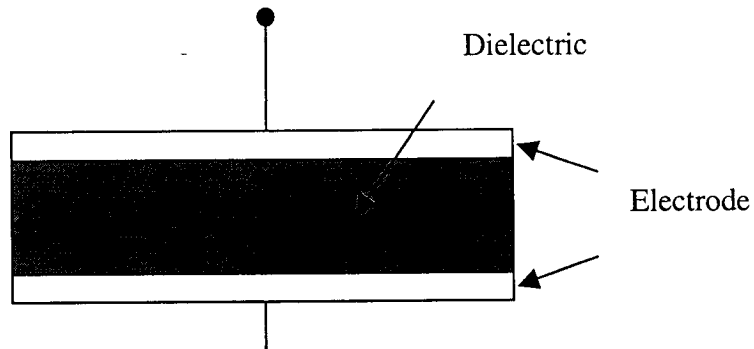


Figure 2.1 Variable capacitance force transducer

The capacitor transducers have high output impedance and more costly as compared to other transducers. The associated circuits of the capacitor transducers are also more intricate. Gray and Fearing et. al. [11] designed micro-machined micro tactile sensor array. It consists of eight-by-eight tactile capacitive array for detection of the micrometer deformation and millinewton forces. Miniaturization made this sensor compatible for robotics and medicine application. The results show hysteresis problem and also failing in detecting the proximity effects. These types of sensors only senses force used for bending the capacitor plates but does not measure the position of the force.

Manish [12] designed capacitive type silicon micromachined pressure sensor for endoscopic grasper. Aluminum electrodes were sputtered inside deep cavities etched in glass. The pressure range of 0.01N/mm^2 up to 0.05N/mm^2 , which is favorable to measure the tissue handling has been claimed. The design of the sensor is shown in the Figure 2.2.

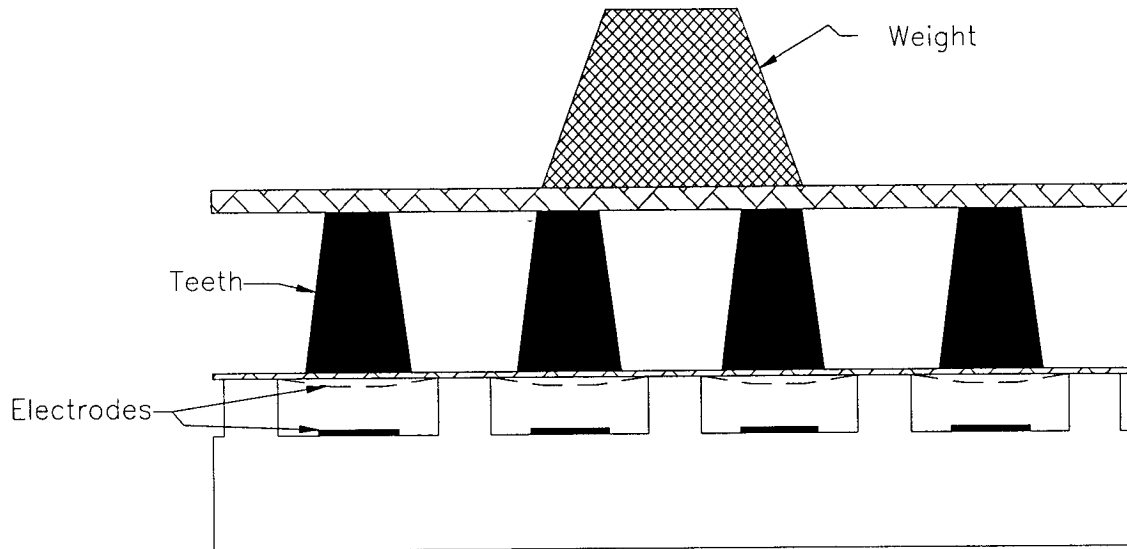


Figure 2.2 Capacitive type sensor used for measuring the force in endoscope grasper

2.2.2 Conductive Polymers

Conductive polymers are also known as Force Sensing Resistor (FSR) and its function is based on the fact that properties of the polymers change when force is applied. The main property of polymer that decreases when force increases is resistivity. Conductive polymers are available in the form of films with different thicknesses. It consists of two parts, one part is made up of resistive materials that is used as film in which conductive digital contact is sandwiched. The resistive films complete the circuit. Films are generally made up of silicon rubber by mixing with the catalyst and processed at room temperature vulcanization (RTV). Mostly silicon rubber is embedded with the carbon crystals, which give resistivity of order 10 Ohm-cm. Increase of pressure on the silicon rubber reduces the resistivity. The carbon particles embedded in the rubber come

closer and make more intimate contact. FRS is not viable for measuring small forces accurately and it exhibits 15% to 25% variation in resistance.

These devices show hysteresis problem. Sensors are economically cheaper than other sensing devices. Inherent problems like non-linearity and lack of sensitivity make sensor more unreliable. But these problems could be solve up-to some extent. Jensen et. al. [37] used conductive polymer sensor for measuring external force as shown in the Figure 2.3. It is the schematic diagram of conductive polymer type sensor.

Conductive sensors made up of carbon fiber, are used to increase the accuracy and to reduce the hysteresis problem. Carbon fibers with fine diameter range in few ‘mm’ are available in thread like form. However, the load range is very limited with high hysteresis and poor accuracy.

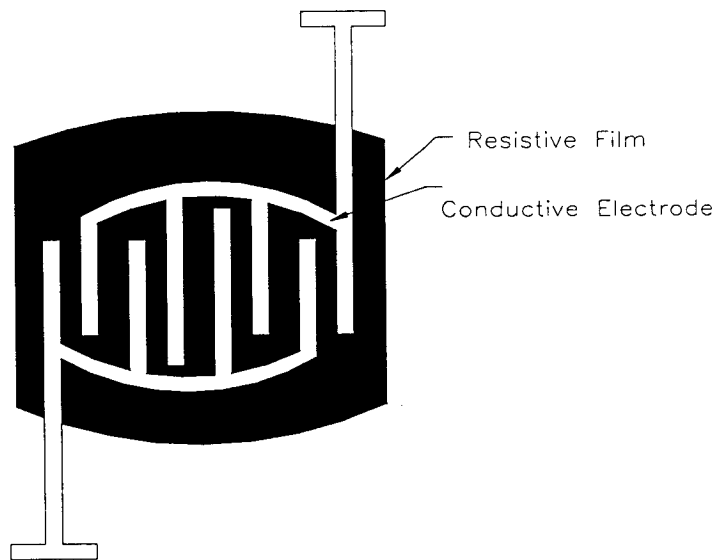


Figure 2.3 Conductive polymer sensor is based on the change in resistance of resistive film between conductive electrodes.

2.2.3 Inductive Displacement Sensors

Inductive transducers for mechanical measurement are electromechanical displacement sensors. LVDT (Linear Variable Differential Transformer) is an example for inductive sensors. It is based on the principle of change in inductance with change in the magnetic field. The inductance depends on the relative separation between the two coils. As the pressure is applied, relative distance between the coils decreases which gives rise to the inductance or decrease in resonant frequency. The relation could be correlated between the pressure and resonant frequency. Air core inductance type sensors are less sensitive as compared to the iron core. Miniaturization of the inductive sensor for high sensitivity using iron core is impractical. The main advantages of the inductive sensors are that they are inexpensive, have no temperature drift, and are resistant to noise (low SNR).

2.2.4 Magnetoresistive (MR) Force Sensors

These types of sensors are widely used in Biosensor industry. It is based on the phenomenon of change in electrical resistance due to external applied magnetic field. This sensor is based on the hall-effect, i.e., the effect of the force exerted by the magnetic field on the moving particles of the current. Basically it is based on the simple practical example that holding a magnet near certain metal causes its atoms to tilt. The tilted atoms present larger obstacle than untilt ones to passing electron. MR sensor senses magnetic fields by measuring an induced voltage in a semiconductor that carries a current. They are usually used as position, speed and current sensor. The highly sensitive

Magnetoresistive (MR) sensors are known as giant magnetoresistive (GMR). These are used for read/write heads of hard drives. GMR sensors are used in nanotechnology for detecting the single molecule. Thus miniature magnet sensor is integrated with deformable element holding a miniature magnet that moves closer to hall-effect sensor. It also required four wires per tactel and it makes it cumbersome to handle.

2.2.5 Optical Sensors

Optical sensors are recent development in the field of fiber optics technology. Optical sensor deals with light emitter and receiver. The optical sensors detect presence, absence, position and characteristic of objects by the interruption of light path. The interruption of the light path causes change in the intensity of the light. As force applied to object comes in the path of source of light (light emitting diode, LED) and receiver of light (photodiode, PIN), this will result in difference in intensity of light emitted and light received [31]. These types of sensors are known as occluder sensors. An occluder partially blocked the light beam and thus modulates its amplitude. The Lord Corporation designed LTS-200 [34] tactile sensor used for measuring force, it converts the force into linear translation. Similarly fiber optics used to measure the force depending upon the light attenuation [31]. The force applied to fiber optics distorts the fiber, which causes the light to leak from the fiber. Fibers have also been used directly as transducers in design of tactile sensors.

The reflective type optical sensor is shown in Figure 2.4. Fiber optics sensor has many advantages; it gives low signal attenuation, high information carrying capacity, flexibility and no electromagnetic interference problems. These sensors also have some

physical properties like small size, rugged, inexpensive and light weight. The small size and flexibility make it more compatible for bioinstruments. With the help of the complex algorithms object position, orientation, size and contour information can be retrieved [38].

In addition to these properties, sensing element can be made as small as fiber, < 0.1 mm diameter. Optical fiber is made up of glass or plastic core (0.01-0.2 mm in diameter), surrounded by the cladding (covering), which has lower index of refraction than core, restricting the light beam to escape. Fiber optics is mostly used to measure the force in cardiac catheters, teleoperation and robotics [39]. It also helps in transmitting data to surgeon during cardiac surgery. Ohka et. al. [18] designed a three axial tactile optical sensor. The results were reported on the large-scale tactile sensor. The experimental results confirmed that sensor was capable of measuring the three-axial force. Sensor consists of CCD camera and silicon rubber. Suzuki [40] also discussed microforce sensor with an optical interferometer. But miniaturization of the sensor is challenging and complicated task.

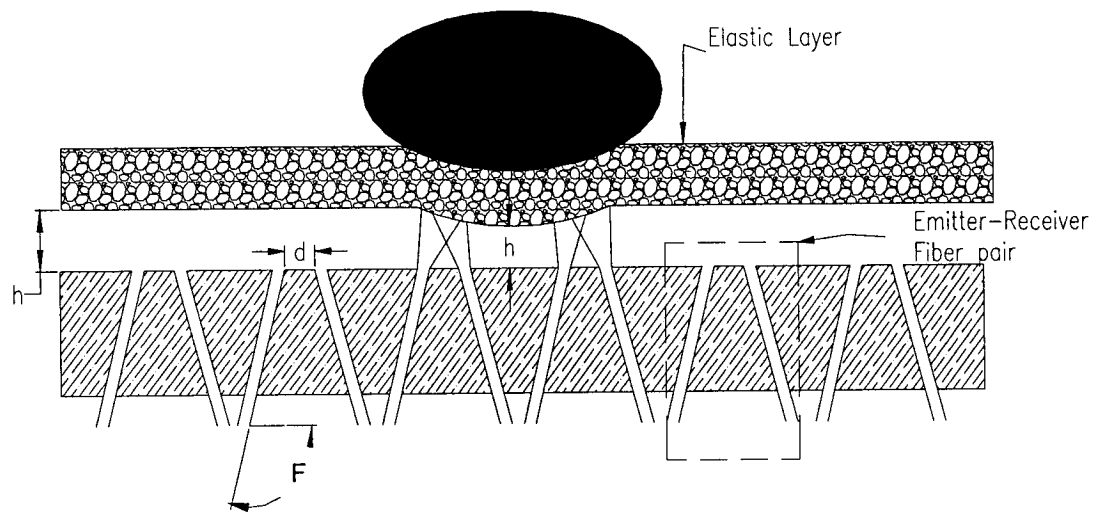


Figure 2.4 Reflective type optical sensor measures the light intensity between emitter and receiver

2.2.6 Strain Gage Sensors

Strain develops in the body, when force is applied and the strain is directly proportional to the applied force. To measure the strain in the body, several types of sensors are used. The main types of sensor are piezoresistive and metal strain gage. Selection of the strain gage for measuring a force at the given condition of measurement depends on several factors such as spatial constraint, temperature, strain rate, frequency response, magnitude of force, cost, geometry, accuracy and sensitivity of the gage. It is very difficult to align and are very fragile in nature. It may even break under small shocks and vibration.

Fundamentally, all strain gages are designed to convert mechanical motion into an electric signal. A change in resistance is proportional to the strain experienced by the sensor. If a wire is held under tension, it gets slightly longer and its cross-sectional area is

reduced. This changes its resistance (R) proportional to the strain sensitivity (S) of the wire's resistance. The strain sensitivity, which is also called the gage factor (GF) can be defined as below:

$$GF = \frac{\frac{\Delta R}{R}}{\frac{\Delta L}{L}} \qquad GF = \frac{\frac{\Delta R}{R}}{\text{Strain}}$$

The ideal strain gage would change resistance only due to the deformations of the surface to which the gage is attached. However, in real applications, temperature, material properties, the adhesive that bonds the gage to the surface, and the stability of the metal, all affect the measured resistance. Because most materials do not have the same properties in all directions, knowledge of the axial strain alone is insufficient for a complete analysis. Poisson ratio, bending, and torsional strains also need to be measured. Each requires a different strain gage arrangement.

Metallic strain gage are generally used to measure the strains. They are made of constantan (Ni-Copper alloy), Nickel-Chromium alloys or Karma alloys (Ref [34]). Strain gages are usually very thin and either wire or foil type arrangements are available. These are adhered to insulated deformable backing. The metallic foil-type strain gage consists of a grid of wire filament of approximately 0.025 mm thickness, bonded directly to the strained surface by a thin layer of epoxy resin. When a load is applied to the surface, the resulting change in surface length is communicated to the resistor and the corresponding strain is measured in terms of the electrical resistance of the foil wire, which varies linearly with strain.

Semiconductor strain gage uses phenomena of piezoresistive effect. It is made of silicon or germanium. The main advantage of semiconductor type strain gage is high

sensitivity and reliability. The gage factor for the semiconductor strain gages are in the order of 150 as compared with 2 or 3.5 for metallic gages [32]. But it also has some disadvantages such as non-linearity, higher temperature sensitivity, limited strain range, fragility and high cost. These gages are fabricated by depositing material directly on the substrate by means of evaporation process. The piezoresistive strain gage behaves differently from piezoelectric polymers. In piezoelectric polymers mechanical energy is converted into the electrical form, but in the case of piezoresistive strain gage, it modulates the current flowing through by altering the force dependent resistance. We can say that the resistance is changed with the force applied in piezoresistive gage.

The change in resistance of piezoresistive gage depends on the current carrying ability of conductive particles. On the contrary, metallic strain gages use the phenomenon of change in geometry of wire during strain. The effect of geometrical deformation is seen in both types of strain gages. Piezoresistive effect is more predominant as compared to the geometrical deformation, i.e. piezoresistive gages show high GF as compared to metallic ones. The piezoresistive strain gages are further dividing into two categories n-type and p-type depending upon the doping [41]. The n-type and p-type gives negative and positive GF, respectively. These strain gages are manufactured by doping n-type and p-type materials into silicon. To reduce the signal-to-noise ratio, gage factor must be sufficiently high. The performance of the strain gage depends on the gage factor. Mostly p-type gage is preferred over n-type gage because of high gage factor, linear behavior and high sensitivity. The GF also depends upon the orientation and crystal size. The simple strain gage is shown in Figure 2.5.

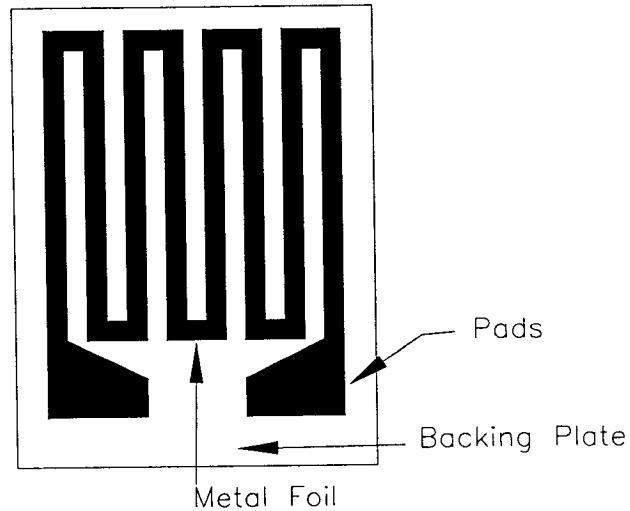


Figure 2.5 Strain gage type sensor based on the change of physical geometry of gage.

Piezoresistive gages are more dependent on the temperature as compared to metallic gage. But this effect can be eliminated by highly doping with impurities (p-type crystals). On the other hand, high doping level also makes GF insensitive to the strain. The temperature compensation is provided with the help of full Wheatstone bridge. This is very helpful in medical robotics application [10].

Josivaldo G. da Silva et. al. [43] designed a strain gage tactile sensor for finger-mounted applications. Results were reported with good linearity and sensitivity. The spatial constraint was the main problem for tactile sensor. The range of the sensor was from 0 N to 100 N with resolution of 0.3 N. To overcome the spatial constraint and resolution, Obana et. al. [19] designed semiconductor strain gage type tactile sensor. This semiconductor sensor shows hysteresis problem with good linear response. A good force sensitivity was reported, i.e., 0.05V/N.

2.2.7 Piezoelectric Sensors

This is the latest technology used in the field of micro-electro-mechanical systems. The designing of the sensors using piezoelectric materials is becoming very common. It is based on the properties of piezoelectric materials. First, piezoelectric material was discovered in 19th century by Curie. Piezoelectric substance has inherited properties in converting mechanical energy to electrical energy and vice-versa. When stress is applied to piezoelectric substance, it generates voltage and voltage applied to substance generates mechanical deformation. This dual-nature of piezoelectric substances makes it more versatile and functional.

This phenomenon is known as the piezoelectric effect. It states that when asymmetrical, elastic crystals are deformed by the force, an electrical potential is generated on the distorted crystal faces. The phenomenon is reversible, i.e., voltage applied generates deformation in crystal. Earlier piezoelectric substances are known as electro-resistive elements. The magnitude of charge developed is directly proportional to the applied force and vice-versa.

The common piezoelectric substances used are quartz, lead zirconate titanate (PZT), poly-vinylidene fluoride (PVDF), barium titanate, tourmaline and rochelle salt. Naturally occurring piezoelectrics materials like quartz, tourmaline are polarized in nature. For synthetic piezoelectric material polarization is required. Piezoelectric materials are available in the form of films and ceramics. The use of piezoelectric material highly depends on the nature of the application. The PVDF films are available in thickness of $6\mu\text{m} - 1000\mu\text{m}$. Ceramics are classified as piezoelectric materials and PVDF is categorized under piezo-polymers. The modulus of elasticity of the piezoelectric

materials varies from 2GPa (for polymers) to 150GPa (for ceramics) [44]. The piezoelectric sensors are inexpensive and rugged. The sensitivity of the sensor depends upon the charge producing capacity (depends upon the coefficients values d_{33} , g_{33}). The d_{33} and g_{33} coefficient correlates the force and charge producing characteristics of the PVDF film. More explanation of the coefficients is given in the Appendix I. Mostly the sensitivity ranges from 10 to 100 pico-Coulombs/N of applied force.

PVDF has long chain molecules with repetition of CF_2-CH_2 molecules in semi-crystalline form of approximately 50-65% crystallinity. Large dipole moment is noticed because of high electro-negativity of fluoride atoms as compared to carbon atoms. The piezoelectric polymer also shows pyroelectric effect, i.e. change in temperature causes the change in mechanical stresses and voltage generation [44]. The most important effect is the sensitivity dependence on the direction of the measurement, i.e. drawn, transverse and thickness in uniaxially orientated PVDF film. Sensitivity of piezoelectric substance with temperature creates problem for designing the force sensor. The temperature dependent effect of piezoelectric material is known as pyroelectric effect. This effect can be used in manufacturing a transducer for the temperature measurement sensor. In tactile piezoelectric sensors, for sensors having an area of 4mm^2 , the temperature change of 0.15K generates a charge equivalent to a force of 1N [45]. Proper insulation of the PVDF film prevents this variation. In addition to temperature drift, piezoelectric materials can only measure dynamic load response. The static loading can be measured by designing the circuit for large time constant ($\tau = RC$). These sensors are preferred because of their high sensitivity and low frequency response. They even respond to finest touch. Force produces the charge in the piezoelectric crystal as shown in the Figure 2.6.

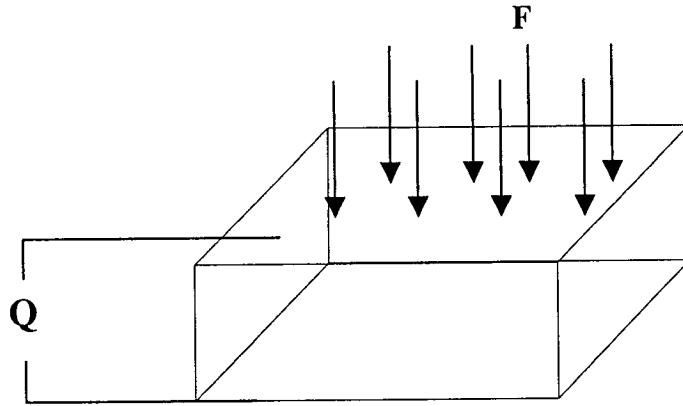


Figure 2.6 Voltage generation by the piezoelectric substance

Shinoda et. al. [16] designed a tactile sensor with 5-D deformation sensing element. It is based upon the ultrasonic wave front in flexible medium. Pieces of piezo film were placed on the top and bottom of the transducer with a section of silicon rubber. The ultrasonic pulses are transmitted by piezo films, which bounce off the rubber-air interface and return. The time of rebound from interface determines the compression in rubber. Knowing modulus of rubber and time of flight, applied force can be calculated. Sensor measures $10\mu\text{m}$ displacement and 0.001rad change of surface inclination and also slippage. It measures three translational and two rotational deformations. The design of the sensor is shown in Figure 2.7.

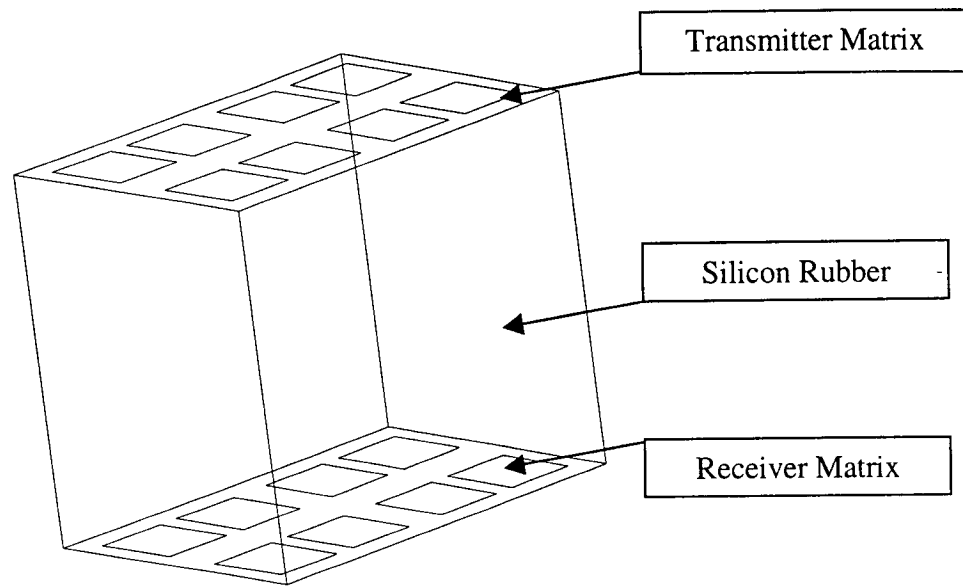


Figure 2.7 Ultrasound wave front sensor consists of PVDF films on the opposite sides as a transmitter and receiver matrix. [16]

2.3 Selection and Decision

Before making decision, first of all, the advantages and disadvantages of different technologies should be compared. All the previous discussions on transduction method for force measuring devices are given in Table 2.1. From Table 2.1, it is clear that capacitor, conductive polymers, magnetoresistive (MR), inductive and optical sensors required some input source. Capacitive and piezoresistive sensor have higher level of the sensitivity but also show noise and hysteresis problem. Silicon strain gages are fragile and they are also difficult to align while gluing. Optical sensor is good preference for the measurement of very minute force but it could not be achieved easily (required emitter and receiver). The input could be in the form of LED, current or magnetic field.

Secondly, two tasks in design of a single tactile sensor should be considered: 1-measuring force and 2-finding the compliance of tissue. Calculation of the compliance of tissue is based on the relative deformation in two parts of the sensor.

The actual measurement of the sensor depends on the stress-strain relationship and changes in electrical properties. For higher sensitivity of the sensor, small stress-strain change with large coupling coefficient is required. PVDF film is one of these materials that its electrical properties change with small change in strain. PVDF film has also low modulus of elasticity and coefficient of coupling as compared to ceramic. PVDF films do not require any activation current, which is highly undesirable in the medical application.

After reviewing the advantages and disadvantages of various sensors, it was decided that piezoelectric sensor is the best choice for measuring force and compliance of tissue. It is also easy to install and miniaturize. Very thin size and high sensitivity of piezoelectric film (around $25\mu\text{m}$) is capable to measure the small touch to the surface. Proper insulation can be provided to avoid the temperature drift. Application of PVDF film in sensor design is discussed in Chapter 3.

Table 2.1 Comparison of the different sensor technologies used for measuring force.

Sensor Type	Advantage	Disadvantage	Purpose
Capacitor type	Simple construction Static and dynamic response Small size and mass Excellent response Continuous response in dc, digital.	High Impedance Temperature drift Complex circuit is required	Used for measuring small forces
Conductive Polymers	Inexpensive Easy to install	High hysteresis Low accuracy Not viable for small force measurements Non-linear variation	Used for measuring force
Inductive Sensor	Continuous resolution Static and dynamic response High output response High SNR LVDT (example) No temperature drift	No high frequency response Large displacement Input required External magnetic field influence Miniaturization impossible	Used for measuring large displacement
Magneto Resistive Sensor (MR)	Highly sensitive (GMR) Good frequency response	Cumbersome Electrical Connection Non-linearity	Used for Position, current sensor, speed
Optical Sensors	Low signal attenuation High information capacity Flexibility and no electromagnetic interference problems High sensitivity Small size, rugged, inexpensive and light weight Compatible for bioinstruments	Extremely fragile Sensitive to vibration Required light emitter and receiver Miniaturization for force sensor is difficult	Used for cardiac catheters, teleoperation and robotics
Strain Gage Sensor	High accuracy Static and dynamic response Insensitive to shocks and vibrations Reliability	Low stability Higher temperature sensitivity Limited strain range Fragile Nonlinear Low dynamic range Hysteresis problem	Used to measure strain caused by the force, shear, pressure and torque

Piezoelectric Sensors	High accuracy Static and dynamic response Insensitive to shocks and vibrations High resolution Readily miniaturized	High temperature drift Low frequency response	Used as force sensor and temperature sensor.
--------------------------	---	---	---

Chapter 3

Design of PVDF Sensor

In this chapter the design of the sensor capable of measuring the force and compliance of the sensed object will be discussed. The design of both single sensor and array of the sensors with the detailed assembling and properties of the material are studied. Piezoelectric film is used to measure the force at different parts of the sensor. The complete assembly of the single sensor is given in the Figure 3.1.

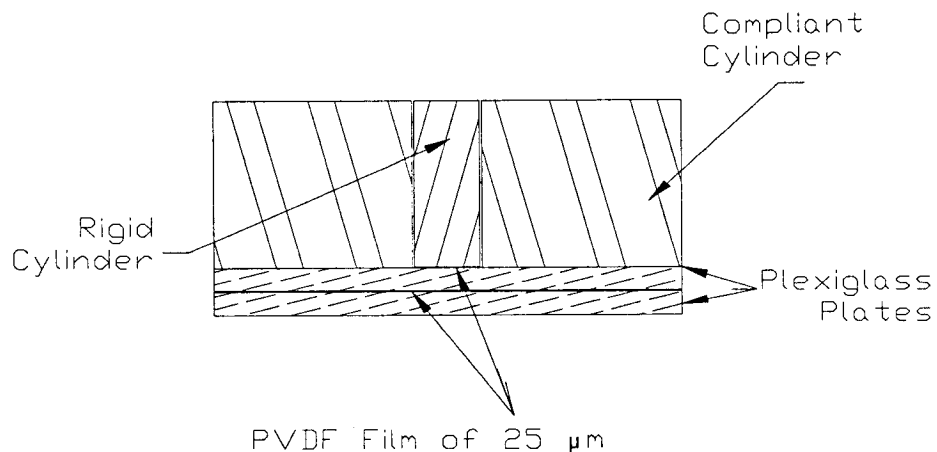


Figure 3.1 Complete assembly of the single sensor.

3.1 Single Sensor Design

The single sensor consists of rigid and compliant cylinders. The rigid cylinder is glued to the base plate and is surrounded by the compliant cylinder. The rigid and compliant cylinders are made up of phenolic and soft rubber, respectively. The PVDF films are used to measure the force at the rigid part and the total force applied to the

sensor. Circular PVDF film placed between the rigid cylinder and base Plexiglas plate is used to measure the force experienced at the rigid part and rectangular PVDF film sandwiched between the two rigid plexiglas plates is used to measure the total applied force.

3.1.1 Design of Plates

Sensor design consists of two 10 x 10 x 0.55 mm square plexiglas plates, which are used as the base for the sensor. The properties of the plate material are given in Table 3.1. Plexiglas is preferred as a base plate due to its high surface finish, surface texture and non-reactive to the chemicals. It is also very hard in nature, its modulus of elasticity lies between the 50 MPa to 100 MPa. A PVDF film is sandwiched between these two plexiglas plates. This sandwiched film measures voltage response in proportional to the total force applied on the sensor. Material properties are provided by the manufacturer and compared with the materials properties website [62]. The top and bottom plexiglas plates are numbered as plate 2 and plate 1, respectively. The schematic diagram of the plates is shown in the Figure 3.1.

Table 3.1. Properties of the Plexiglas

Properties of plexiglas used as base plate for sensor	
Young's Modulus	$70 \times 10^6 \text{ Pa}$
Density	1190 Kg/m^3
Poisson Ratio	0.3
Dimension of Plate	$L = 10\text{mm}, L = 10\text{mm} T = 0.55 \text{ mm}$

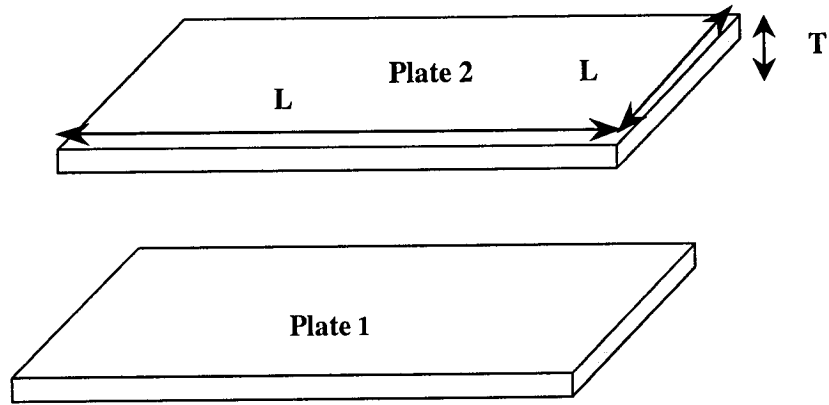


Figure 3.2. Design of base plates for single sensor

3.1.2 Design of PVDF Films

Piezoelectric properties made piezoelectric material to be used as sensor and actuator. When external force is applied to piezo-materials it generates charge on the surface, which is proportional to applied mechanical stress. The converse effect is also possible, applied voltage generates deformation in the piezoelectric materials. Piezoelectricity is related to the crystalline ionic structure. As mentioned before, circular PVDF film is sandwiched between the rigid cylinder and plate 2 while rectangular one is sandwiched between the plate 1 and plate 2. For the sake of clarity, rectangular and circular PDVF films are numbered as PVDF-1 and PVDF-2, respectively. The design of the PVDF-1 and PVDF-2 is addressed in the following section.

3.1.2.1 PVDF-1 Design

The PVDF-1 is sandwiched between the plexiglas plate 1 and plate 2. This PVDF film measures the total force applied on the sensor. The rectangular PVDF film with size of 10 x 10 mm and thickness of 25×10^{-6} m has been used. The PVDF-1 film is metallized on both sides with aluminum coating, which act as the charge collector. The developed signal is then transmitted to the charge amplifier for the required amplification. The properties of the PVDF film are given in Table 3.2. The shape of the PVDF films is also shown in Figure 3.2. The technical data was provided by the good fellow company.

Table 3.2 Properties of the PVDF films

Properties of the PVDF Films (Metallized both sides)	
Orientation of films	Uniaxially
Tensile Modulus (GPa)	1.8-2.7
Density (g cm^{-3})	1.76
Poisson's ratio	0.34
Piezo Coefficient d_{31} , d_{32} , d_{33} (pC.N^{-1})	18-20, 2, ~ -20 , respectively
Piezo Coefficient g_{31} , g_{32} , g_{33} (Vm.N^{-1})	0.15, 0.015, ~ -0.15 , respectively

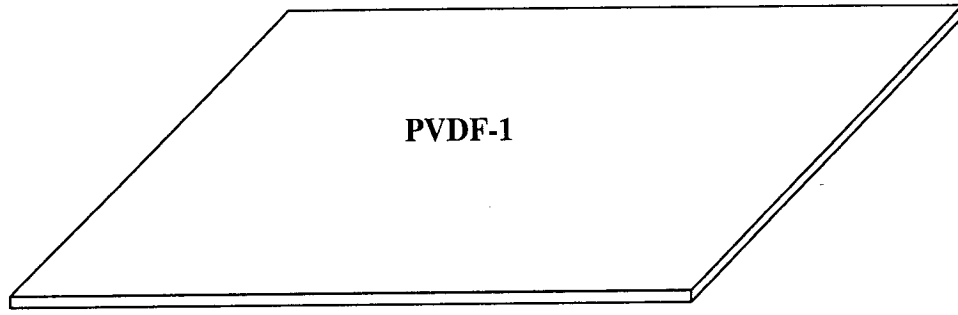


Figure 3.3. PVDF-1 film with both sides metallized.

$$L = 10\text{mm}, T = 25 \times 10^{-3}\text{mm}$$

3.1.2.2 PVDF-2 Design

This PVDF-2 film has a circular shape with the radius of 1.4 mm and thickness of 25×10^{-3} mm as shown in the Figure 3.3. The same material properties are similar to those of PVDF-1 given in the Table 3.2. The film is placed between the rigid cylinder surface and plate-2. This PVDF film measures the force experienced on the rigid cylinder. The PVDF film is anisotropic in nature and is polarized in 'Z' direction. The charge developed is taken from two electrodes of aluminum attached to the surface of the PVDF film. In the analysis of forces, it is assumed that no shear forces exist in the sensor and only force and displacement in the Z direction are taken into account.

Basically four parameters are required for analysis of the piezoelectric behavior, i.e. density, anisotropic array, permittivity and piezoelectric matrix. These parameters are mainly supplied by the manufacturer and are provided in the Appendix I (piezoelectricity). It is noted that both the PVDF films are glued by non-conductive glue

to the base plates.

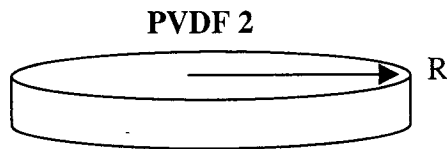


**Figure 3.4 PVDF-2 film of size metallized both sides. $R = 1.4 \text{ mm}$
 $T = 25 \times 10^{-3} \text{ mm}$**

3.1.3 Rigid Cylinder Design

Rigid cylinder plays prominent role in sensing the force and calculating the compliance of the sensed object. Rigid cylinder protrudes outward under applied force which provides the good holding properties to the grasper. The rigid cylinder is made of high pressure laminated phenolic. Laminated phenolic is hard and dense material made by applying heat and pressure to layers of paper or fabric impregnated with synthetic resin. These layers or laminations are usually of cellulose paper, cotton fabrics and glass fiber. When heat and pressure are applied to the layers, a chemical reaction (polymerization) transforms the layer into a high-pressure thermosetting laminated plastic. The phenolic polymer is used as rigid cylinder due to its non-conductive nature with good rigidity. It has also good mechanical properties, with modulus of elasticity 4.1GPa - 10 G Pa and Poisson's ratio of 0.3. The electrical resistivity offered by the rigid cylinder is quite high ($3.43 \times 10^{11} \text{ Ohm-m}$). This rigid part of the sensor can also act as the tooth. When the force is applied on the sensor, compliance cylinder experiences more compression as compared to the rigid cylinder. As a result of this compression, the rigid

part protruded relative to the compliant part. This provides the gripping effect to the tissue. The radius of the cylinder is 1.4 mm and height of cylinder is 3.88 mm as shown in Figure 3.4.

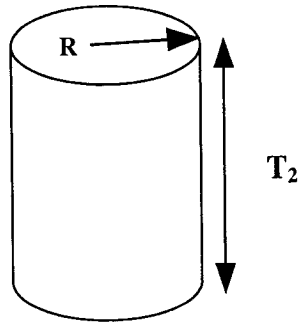


**Figure 3.5 Rigid cylinder made up of phenolic polymer having size
 $R = 1.4 \text{ mm}$, $T_2 = 3.88 \text{ mm}$**

3.1.4 Compliant Cylinder Design

A compliant cylinder which surrounds the rigid cylinder has been designed to measure the compliance of the sensed object. The inner and outer diameter of the cylinder are $R_1 = 1.5 \text{ mm}$ and $R_2 = 5 \text{ mm}$, respectively and the height of the cylinder is $T_2 = 3.88 \text{ mm}$. Two different rubber materials with Young's modulus of $2.4 \times 10^4 \text{ Pa}$ and $3.3 \times 10^4 \text{ Pa}$ have been considered as compliant material. The compliant cylinder is shown in the Figure 3.5.

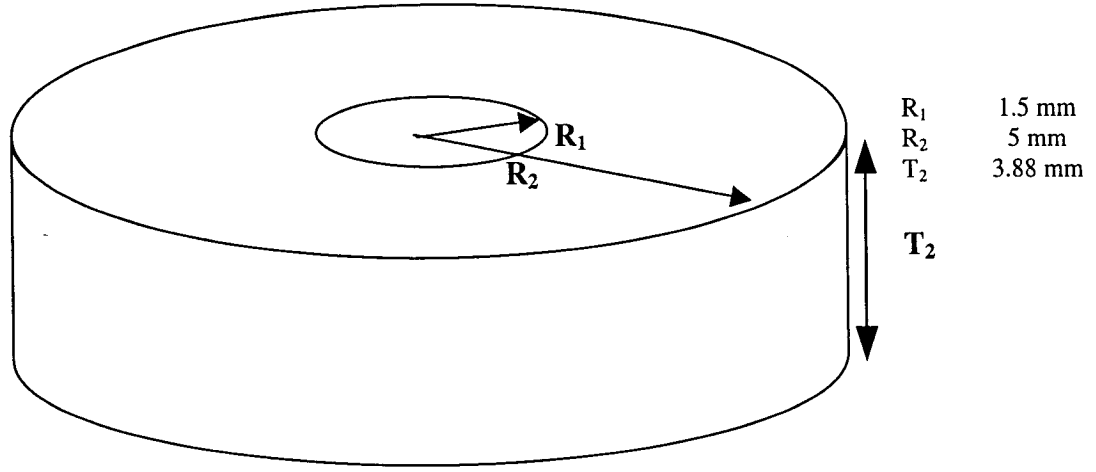


Figure 3.6 Compliant cylinder is made up of soft rubber

3.1.5 Sensed Object Design

It is assumed that tissue or sensed object behaves similar to the soft rubber with the isotropic properties. In reality, the tissue behaves like the visco-elastic material, which has a time dependent response. In this study the visco-elastic behavior of the tissue has not been considered. The tissue is simply considered as rubber specimens with different modulus of elasticity ranging from 1.49×10^4 Pa to 14×10^6 Pa.

3.1.6 Single Sensor Assembly

The parts of the single sensor are attached together using the epoxy glue. Non-conductive and conductive types of epoxy glue have been employed. The electrical connection has been made on the PVDF films by using the conductive epoxy glue; i.e. the wire is attached to the PVDF films on both the upper and lower faces with help of

conductive glue.

Once wire connections are established on the PVDF film, then the PVDF films are placed in the respective position and connected together using non-conductive glue. Small grooves have been provided between the base plates and rigid cylinder in order to accommodate the wires. Since the conductive glue has poor strength it may cause short circuit. Thus it cannot be used to fix the plexiglas plates together. The non-conductive glue provides more strength to the structure. After gluing parts together, it requires sometime to cure. Overall view of the assembly diagram of the single sensor is shown in the Figure 3.6. The detailed design and dimensions of the single sensor are discussed in chapter 4.

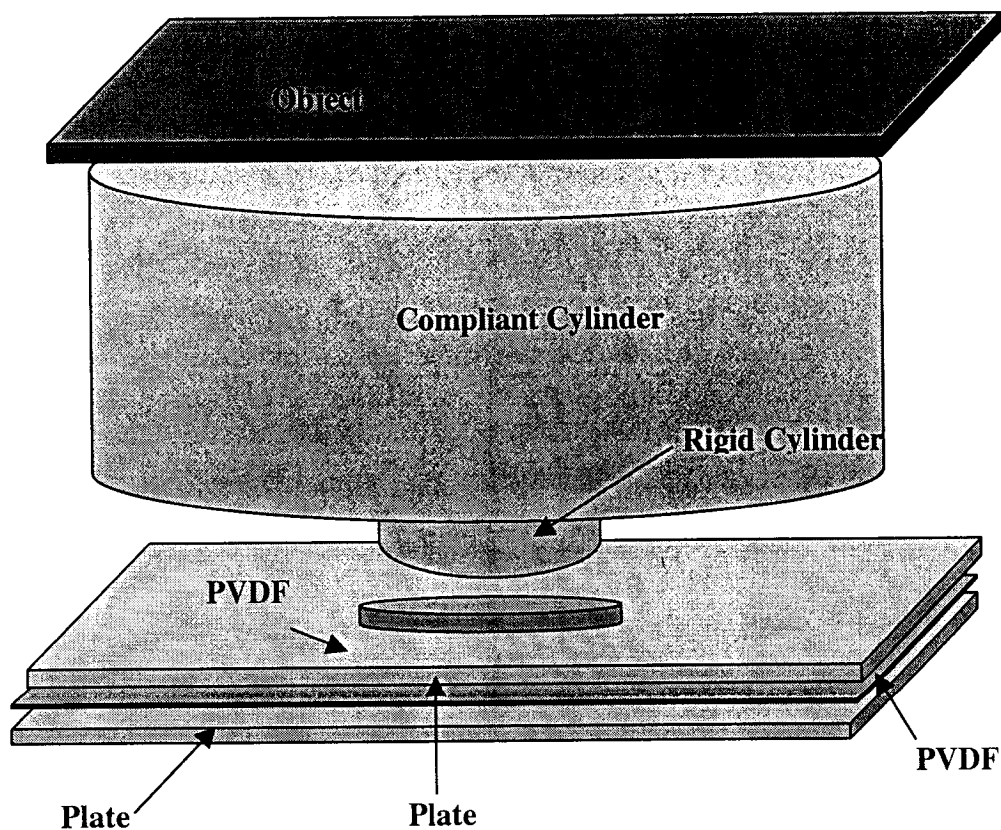


Figure 3.7 Assembly of single

3.2 Two-Sensor Design

The designed single sensor is not useful for the purpose of the endoscope grasper mounting. Endoscope grasper usually requires a number of small micro-machined tactile sensors mounted in the form of array (see Figure 1.1). In practical application, these sensors could be in number of 10-20 in regular pattern of array. In this study, two types of arrays of sensor namely sensors with common base and sensors with different base have been investigated. These sensors only differ in the method of measurement of the total force. For the sake of simplicity the design has been limited to the array of two sensors. The results of this study could be used in designing an array of tooth like tactile sensor used in endoscopic grasper.

3.2.1 Two Sensors with Different Base Plate Design

In the different base sensor configuration, two single sensors are mounted beside each other on a combined plate. These sensors measure the force individually irrespective of the adjacent sensor. Every sensor has its own PVDF film under its rigid cylinder and base plate. In this design the rectangular PVDF film is mounted for each sensor separately without any mutual connection between each other. The materials used for the different base sensor were similar to those of single sensor but only different in the arrangement. The size of the base plate is 12x24 mm. Detailed design of different base sensor is discussed in Chapter 4. Assembly diagram of the sensor is shown in Figure 3.7. PVDF films are numbered as shown in the Figure 3.7. PVDF 1 and PVDF-3 are circular, PVDF-2 and PVDF-4 are rectangular in shape.

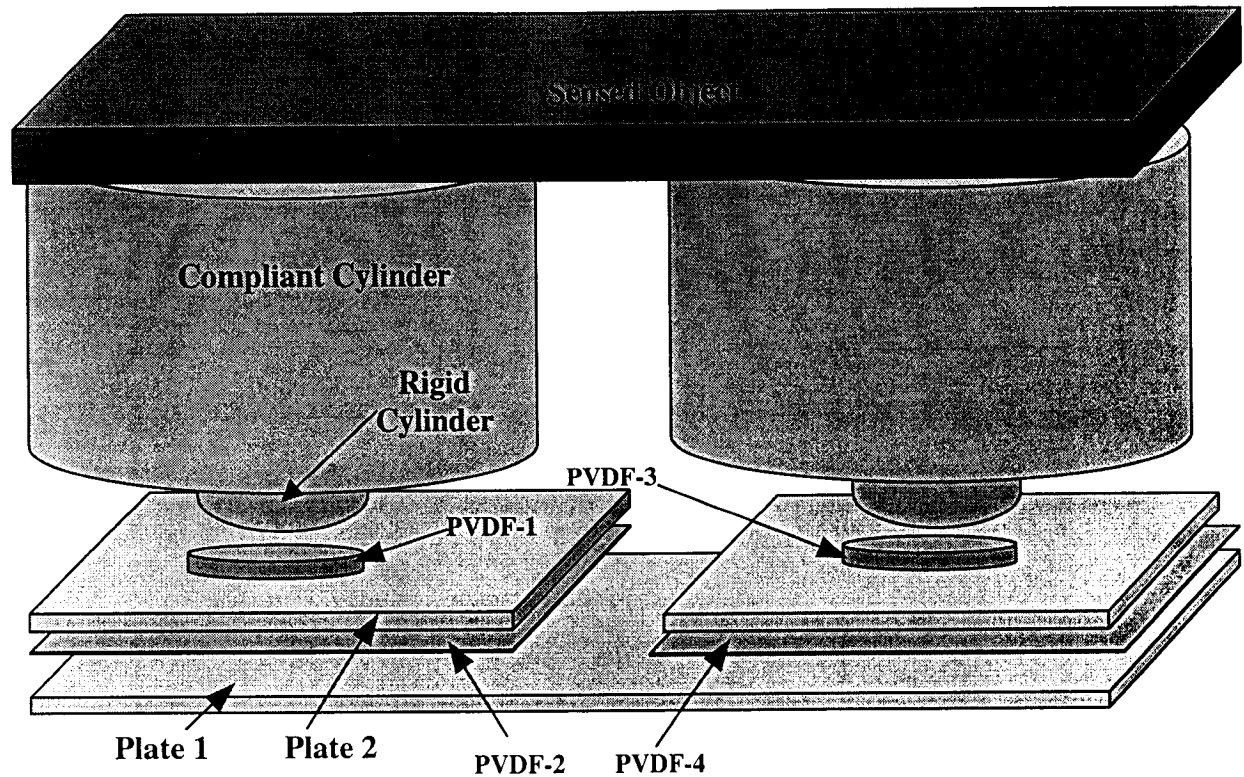


Figure 3.8 Assembly of two sensors on different bases

3.2.2 Two Sensors with Common Base Plate Design

Common base sensors have the same design procedure, however in this case, whole base plate is covered with one PVDF film that measures the total force on the top of the complete assembly of the sensor. PVDF-1 and PVDF-2 are circular and PVDF-3 is rectangular in shape. The materials properties of the element are the same as the single sensor. Detailed design of common base sensor is also discussed in Chapter 4. The assembly diagram of the two sensor mounted on the same base plate are shown in Figure 3.8.

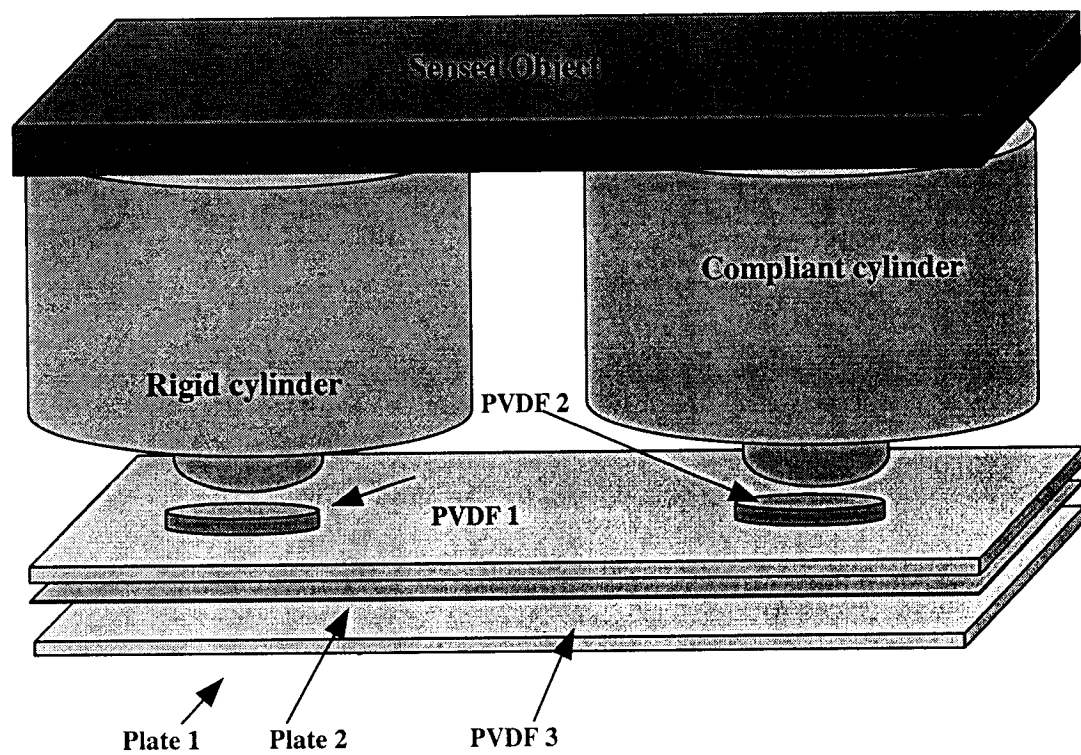


Figure 3.9 Assembly of two sensors on common base

Chapter 4

Numerical Simulation and Comparison

In this chapter 2D and 3D finite element models of the sensor are discussed and compared. Sensor design and advantage of the single sensor and different configuration of the sensors are also investigated.

4.1 Finite Element Formulation

The finite element method is used to study the reaction in the compliant and rigid parts of sensor. Tissue is also modeled in the analysis, and it is assumed that the tissue has uniform distributed modulus of elasticity and the linear behavior. The rigid part of cylinder is considered as rigid support and there is no deflection in the rigid cylindrical part. Only the compliant cylinder part and tissue are considered flexible and can deflect under very small-applied uniform force. For the proposed finite element model, the tissue has been modeled as a beam on rigid (rigid cylinder) and elastic foundation (compliant cylinder). The compliance of the sensed object (tissue) has been calculated by measuring the force distribution on the rigid and compliant parts. The higher the tissue modulus the more reaction will be on the rigid cylinder. The relative deflection between the rigid and compliance part enables the sensor to act as a tooth for holding the tissue.

A geometrical model of a single sensor is given in Figure 4.1a. A Single sensor has been studied and analyzed using 2D finite element formulation. The Fabricated sensor is also shown in the Figure 4.1b. White circular part in the photograph represents

the rigid part and black part represents the compliant cylindrical part of the sensor. As shown in Figure 4.2, the sensor has been modeled as a two-dimensional elastic beam on the rigid and elastic foundation and due to its symmetrical behavior, only one half of the sensor has been considered.

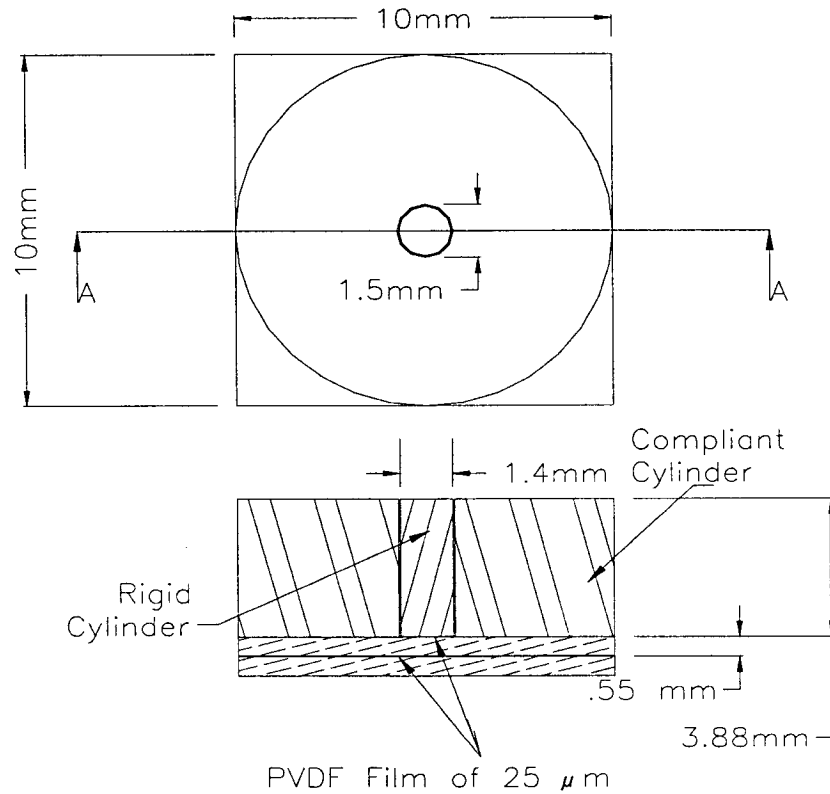


Figure 4.1a Geometrical model of the single sensor

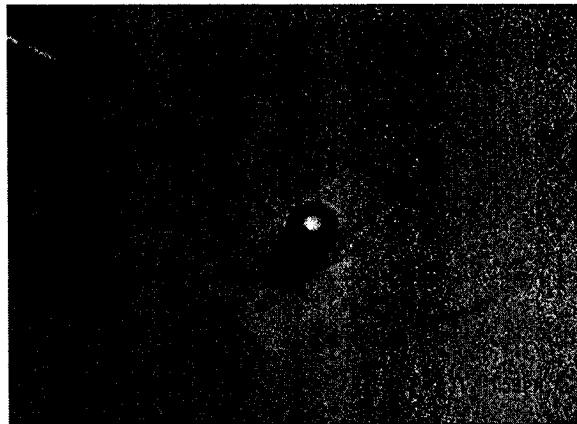


Figure 4.1b Fabricated single sensor

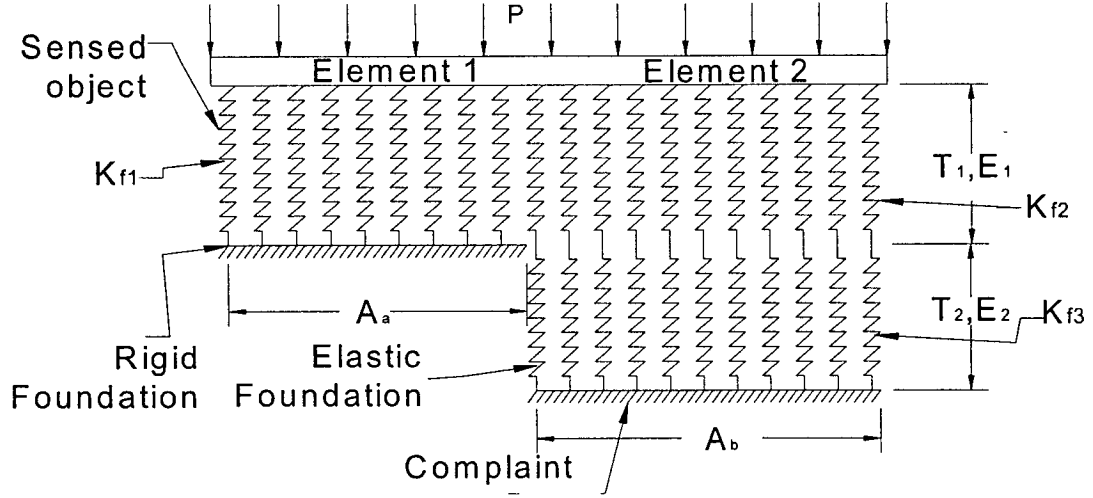


Figure 4.2 Finite element model for single tactile sensor

A uniform load is applied to the sensed object (tissue). The potential energy for a beam on elastic foundation can be written as, [48]:

$$\Pi = \int_0^L \frac{EI}{2} \left(\frac{d^2 v}{dx^2} \right)^2 dx + \int_0^L \frac{K_f v^2}{2} dx - \int_0^L P v dx \quad (4.1)$$

where $v(x)$ is the displacement function, E and I are young's modulus and second moment of inertia, respectively, K_f is the equivalent spring constant per unit length and P is the uniform load applied on the beam. The displacement function can be related to the element nodal displacement vector as

$$v(x) = [N] \{u\} \quad (4.2)$$

where $[N]$ and $\{u\}$ are the shape function matrix $[N]^T = [N_1 \ N_2 \ N_3 \ N_4]$ and nodal displacement vector $\{u\}^T = \{u_1 \ \theta_1 \ u_2 \ \theta_2\}$, respectively. The u and θ represent the displacement and rotational degrees of freedom of the element. The shape functions for the flexural beam element can be written as [48]

$$\begin{aligned}
N_1 &= \frac{2x^3 - 3x^2L + L^3}{L^3}, \\
N_2 &= \frac{x^3L - 2x^2L^2 + xL^3}{L^3}, \\
N_3 &= \frac{-2x^3 + 3x^2L}{L^3}, \\
N_4 &= \frac{x^3L - x^2L^2}{L^3}
\end{aligned} \tag{4.3}$$

By Substituting the Eq. (4.2) into Eq. (4.1) we may obtain:

$$\Pi = \frac{1}{2}EI \int_0^L \{u\}^T [B]^T [B] dx \{u\} + \frac{1}{2} \int_0^L K_f \{u\}^T [N]^T [N] dx \{u\} - \int_0^L P \{u\}^T [N]^T dx \tag{4.4}$$

where $[B] = \frac{\partial^2 [N]}{\partial x^2}$, represented as

$$[B] = \left[\frac{12x - 6L}{L^3} \quad \frac{6xL - 4L^2}{L^3} \quad \frac{-12x + 6L}{L^3} \quad \frac{6xL - 2L^2}{L^3} \right] \tag{4.5}$$

Differentiating Eq. (4.4) with respect to $\{u\}$, the equilibrium equation can be written as:

$$\frac{\partial \Pi}{\partial \{u\}} = EI \int_0^L [B]^T [B] dx \{u\} + \int_0^L K_f [N]^T [N] dx \{u\} - \int_0^L P [N]^T dx = 0 \tag{4.6}$$

$$\left[EI \int_0^L [B]^T [B] dx + \int_0^L K_f [N]^T [N] dx \right] \{u\} = \int_0^L P [N]^T dx \tag{4.7}$$

or in matrix form

$$[k] \{u\} = \{f\} \tag{4.8}$$

where $[k]$ is the element stiffness matrix and $\{f\}$ is the element nodal force vector and can be expressed as:

$$[k] = EI \int_0^L [B]^T [B] dx + \int_0^L K_f [N]^T [N] dx \quad (4.9)$$

$$\{f\} = \int_0^L P [N]^T dx \quad (4.10)$$

It is noted that the stiffness matrix has two terms. The first term is the regular stiffness matrix of the beam and the second term is the stiffness matrix due to the elastic foundation. In other words:

$$[k] = [k_{beam}] + [k_{elastic\ foundation}] \quad (4.11)$$

where

$$[k_{beam}] = EI \int_0^L [B]^T [B] dx \quad (4.12)$$

$$[k_{elastic\ foundation}] = \int_0^L K_f [N]^T [N] dx \quad (4.13)$$

Substituting the values of the [B] and [N] from the Eqs. (4.3) and (4.5) into Eqs. (4.12)

and (4.13), we can obtain:

$$[k_{beam}] = \frac{EI}{L^3} \begin{bmatrix} 12 & 6L & -12 & 6L \\ 6L & 4L^2 & -6L^2 & 2L^2 \\ -12 & -6L^2 & 12 & -6L \\ 6L & 2L^2 & -6L & 4L^2 \end{bmatrix} \quad (4.14)$$

$$[k_{elastic\ foundation}] = K_f \begin{bmatrix} \frac{13L}{35} & \frac{11L}{210} & \frac{9}{70} & -\frac{13L}{420} \\ \frac{11L}{210} & \frac{L^2}{105} & \frac{13L}{420} & -\frac{L^2}{140} \\ \frac{9}{70} & \frac{13L}{420} & \frac{1}{105} & -\frac{11L}{210} \\ -\frac{13L}{420} & -\frac{L^2}{140} & -\frac{11L}{210} & \frac{L^2}{105} \end{bmatrix} \quad (4.15)$$

$$\{f\} = \frac{PL}{12} \begin{Bmatrix} -6 \\ L \\ -6 \\ -L \end{Bmatrix} \quad (4.16)$$

The equivalent spring constant K_f for element number two in Figure 4.2 is obtained by the fact that the sensed object and compliance material are connected in series (two springs in series). In the following, superscript on the stiffness matrix shows the element number. Similarly, subscript as shown in the Figure 4.3 represents element number and number of degree freedom. First number in subscript is the element number and second one is number for degree of freedom. Considering Figure 4.2, the spring constant K_f for element 1 and 2 can be described as:

$$K_f^1 = K_{f1} \quad (4.17)$$

$$K_f^2 = \frac{K_{f2}K_{f3}}{K_{f2} + K_{f3}} \quad (4.18)$$

The value of K_{f1} is the stiffness of the sensed object above the rigid part regarding the element 1. Similarly K_{f2} and K_{f3} are the stiffness of the sensed object and compliant cylinder regarding element 2 as shown in the Figure 4.2. K_f^1 and K_f^2 are the stiffness coefficient to of the element 1 and element 2, respectively. The superscript shows the element number of the element. These stiffness coefficients can be written in terms of area, modulus of elasticity and thickness of the sensed object and compliant object as follows:

$$K_{f1} = \frac{A_a \times E_1}{T_1} \quad (4.19)$$

$$K_{f2} = \frac{A_b \times E_1}{T_1} \quad (4.20)$$

$$K_{f3} = \frac{A_b \times E_2}{T_2} \quad (4.21)$$

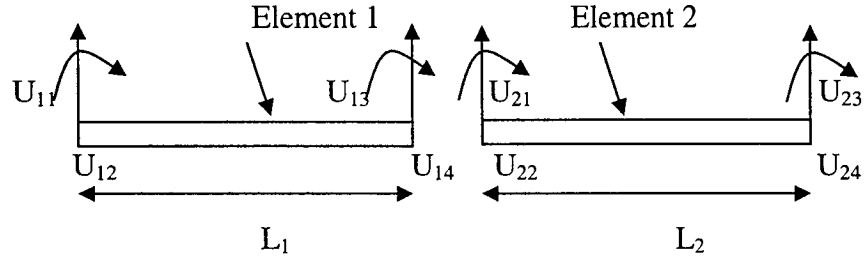


Figure 4.3 Two degrees of freedom model

Assuming $\lambda = \frac{E_1 T_2}{E_2 T_1}$, and substituting values of the stiffness coefficient into

Equations (4.17) and (4.18), we can obtain:

$$K_f^1 = \frac{A_a \times E_1}{T_1} \lambda \quad (4.22)$$

$$K_f^2 = \frac{1}{\frac{T_2}{A_b E_2} \left(\frac{1}{\lambda} + 1 \right)} \quad (4.23)$$

Considering Figure (4.2) and (4.3), two elements are considered with two degrees of freedom at each node. Beneath the Element 1 the spring constant per unit length represents the sensed object. Similarly beneath Element 2 the spring constant per unit length represents the summation of sensed object and compliant part.

Considering Figure 4.3, the finite element model in matrix notation for element number 1 is given as

$$[k]_{4 \times 4}^1 \begin{Bmatrix} U_{11} \\ U_{12} \\ U_{13} \\ U_{14} \end{Bmatrix}_{4 \times 1} = \frac{PL_1}{12} \begin{Bmatrix} -6 \\ L_1 \\ -6 \\ -L_1 \end{Bmatrix}_{4 \times 1} \quad (4.24)$$

Similarly, the finite element notation for the element number 2 is given as

$$[k]_{4 \times 4}^2 \begin{Bmatrix} U_{21} \\ U_{22} \\ U_{23} \\ U_{24} \end{Bmatrix}_{4 \times 1} = \frac{PL_2}{12} \begin{Bmatrix} -6 \\ L_2 \\ -6 \\ -L_2 \end{Bmatrix}_{4 \times 1} \quad (4.25)$$

It is noted that Eqs. (4.24) and (4.25) are equilibrium equations at the element level. After assembling the elements the equilibrium equation at system level can be written as:

$$[K]_{6 \times 6}^{system} \{U\}_{6 \times 1}^{system} = \{F\}_{6 \times 1}^{system} \quad (4.26)$$

where $\{U\}$ and $\{F\}$ are system nodal displacement and force vectors, respectively.

$$\{U\}^T = \{U_1 \ \theta_1 \ U_2 \ \theta_2 \ U_3 \ \theta_3\} \quad (4.27)$$

$$\{F\}^T = \{F_1 \ F_2 \ F_3 \ F_4 \ F_5 \ F_6\} \quad (4.28)$$

The system matrix $[K]^{system}$ is a function of λ and A , represented as

$$[K] = f(\lambda, A) \quad (4.29)$$

where,

$$A = A_b / A_a \quad (4.30)$$

A_a and A_b are the areas of the rigid and compliant parts, respectively. Both rigid and compliant cylindrical parts have the same height T_2 . Where as T_1 is the thickness of the sensed object. The dimensionless constant “ λ ” represents the combined ratio of modulus of elasticity and thickness of the compliant part and sensed object, respectively. The circular and rectangular PVDF films are placed beneath the rigid cylinders and base

plates, respectively. The force experienced by the rigid cylinder and total forces are measured by circular PVDF and rectangular PVDF, respectively. It is noted that the properties of sensed object (Young's modulus and thickness) are not known and the parameters E_2 and T_2 of the compliant object are assumed to be fixed.

A finite element analysis has been performed to find force variation with respect to dimensionless constant λ . The results obtained for force ratio (it is the ratio of force experienced by the rigid cylinder to the total force applied to the sensor) with lambda variation at different area ratio, A , are shown in Figure 4.4. It is clear that as the dimensionless constant λ increases, the sensed object becomes stiffer than the compliant cylinder of the sensor. It is interesting to note that in the limit where the sensed object has higher modulus of elasticity, the force ratio will be approaches unity. In other words, when the stiffness of the sensed object nearly equals to the rigid cylinder, only the rigid cylinder carries all the forces applied, i.e. the deflection between the rigid and compliant cylinder is not significant. When the sensed object is softer as compared to the compliant cylinder, the outer compliant cylinder carries most of the force, thus the force ratio decreases. Force ratio also depends on the different values of the compliant cylinder modulus. The force ratio is directly proportional to the voltage ratio generated at the two different PVDF films.

As shown in the Figure 4.4, the larger the area ratio, the larger the variation in the ratio of the two forces, Therefore, better estimation can be made for the compliance of the object. The better estimation of the force ratio has been obtained for area ratio ranging from 1 to 10. Increasing the area ratio beyond 10, the curve tends to incline more.

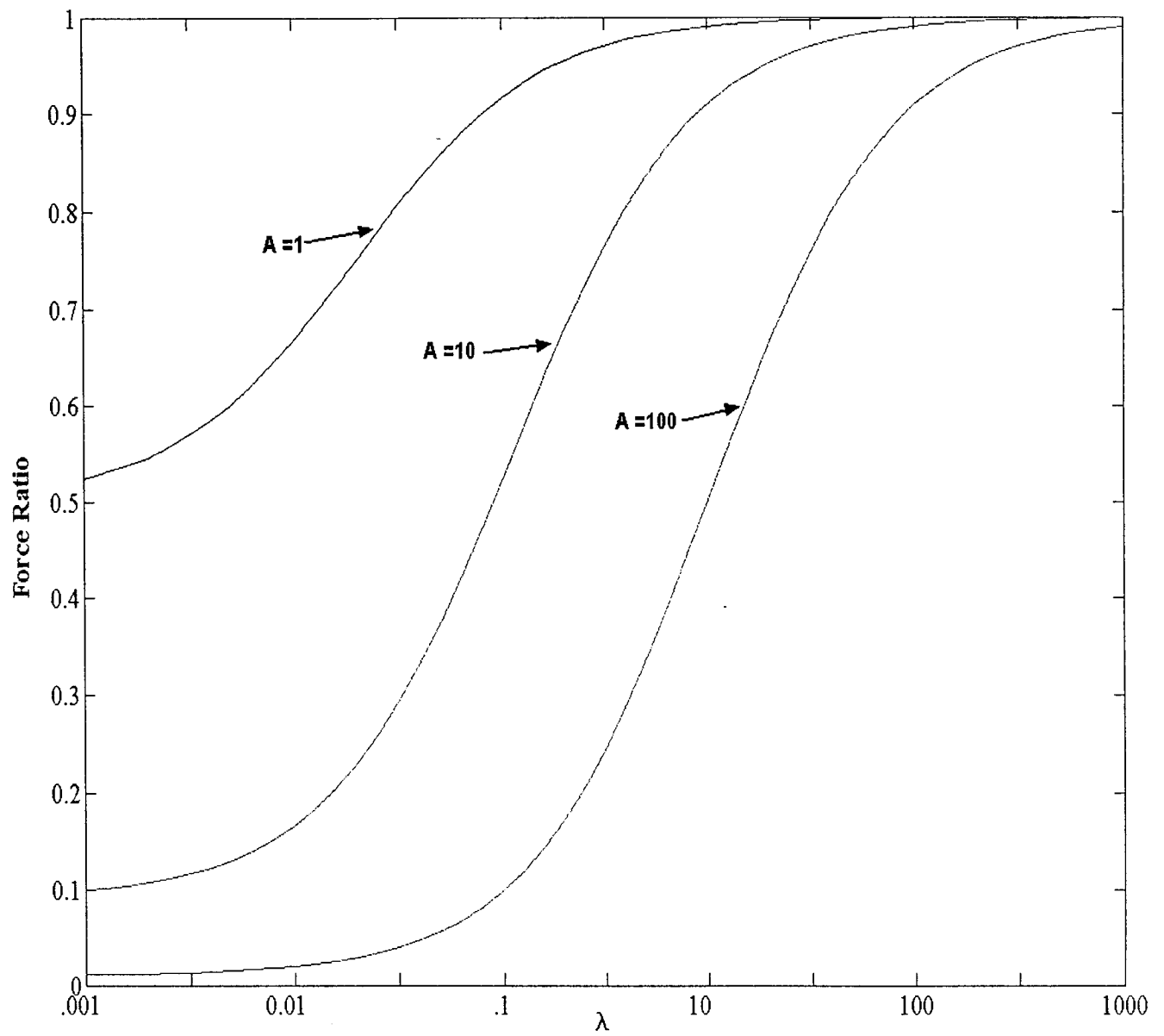


Figure 4.4 Variation of the force ratio with the lambda function

4.2 Analysis in ANSYS

The sensor has also been modeled in ANSYS to validate the results obtained from the proposed finite element model. ANSYS is powerful general-purpose finite element software capable of analyzing the electro-mechanical systems. Due to electro-mechanical nature of the problem, different types of elements have been employed to construct the finite element model of the sensor. These elements are shown in the Figure 4.5. Element Solid 45 has been used to model the plate 1, plate 2 and sensed object of the sensor. The irregular and curved parts of sensor, the rigid and compliant cylindrical parts are all modeled using element Solid 92. Element Solid 5 has been used to mesh the straight edge geometries and rectangular PVDF film which measures the total force of sensor. Element Solid 98, which has a piezoelectric and structural field capabilities similar to Solid 5, is well suited to model irregular edges and has been employed to model the circular PVDF films. The Figure 4.6 shows the single sensor model in ANSYS after meshing. More details of the finite element formulation of the piezoelectric materials are given in the Appendix I.

The complete 3-D model of the single sensor is shown in Figure 4.6. The readings of voltage and force experienced by rigid cylinder are extracted for different set of materials of sensed object. The thickness of the sensed object is assumed to be constant. Two different reading sets are taken at two different modulus of compliant cylinder $2.4 \times 10^4 \text{ N/m}^2$ and $3.3 \times 10^4 \text{ N/m}^2$, respectively. This data is provided in the Appendix II of the dissertation. Only selective set of data is tabulated in the Table 4.1 and Table 4.2.

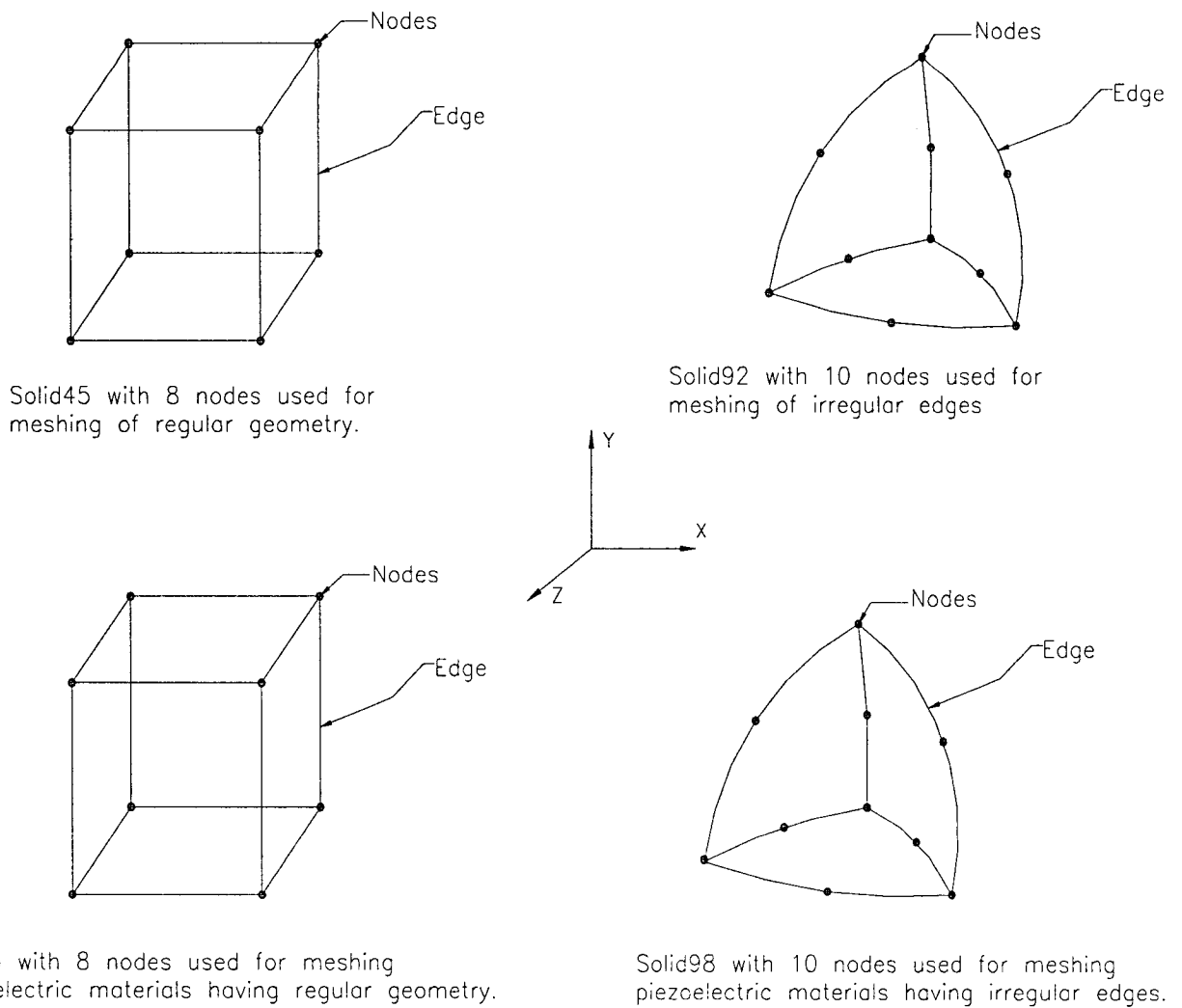


Figure 4.5 Different types of elements used for meshing

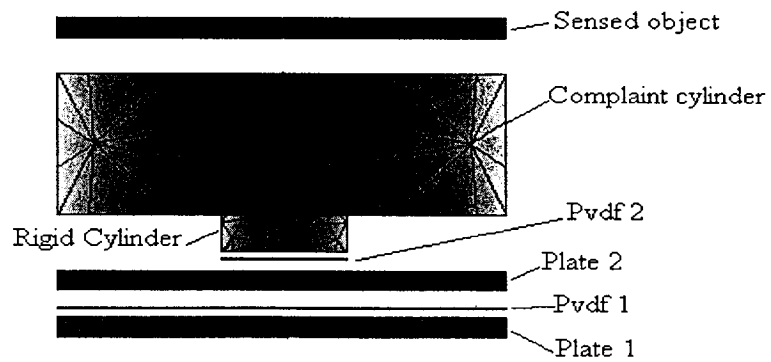


Figure 4.6 Meshed single sensor with assigned elements

Table 4.1 Voltage generation and force distribution on the rigid cylinder of single sensor at the compliance of cylinder 2.4×10^4 .

Sensed object (N/m ²)	Voltage (V)		Force at Rigid Cylinder(N)	Stresses at Rigid Cylinder(N/m ²)	Total Force (N)
	PVDF 2	PVDF 1			
1.49e4	-0.142e-3	-0.616e-4	-0.1417	-23025	-1
3.35e4	-0.191e-3	-0.616e-4	-0.1914	-31097	-1
9.54e4	-0.322e-3	-0.616e-4	-0.3089	-52311	-1
2.56e5	-0.522e-3	-0.616e-4	-0.5223	-84829	-1
1.2e6	-0.824e-3	-0.616e-4	-0.8254	-134050	-1
7.5e6	-0.965e-3	-0.616e-4	-0.9657	-156980	-1
140e6	-0.997e-3	-0.616e-4	-0.9971	-162100	-1

Table 4.2 Voltage generation and force distribution on the rigid cylinder of single sensor at the compliance of cylinder 3.3×10^4 .

Sensed object (N/m ²)	Voltage (V)		Force at rigid cylinder(N)	Stresses at rigid cylinder(N/m ²)	Total Force (N)
	PVDF 2	PVDF 1			
1.49e4	-0.130e-3	-0.616e-4	-0.1301	-21128	-1
3.35e4	-0.168e-3	-0.616e-4	-0.1678	-27252	-1
9.54e4	-0.272e-3	-0.616e-4	-0.2727	-44291	-1
2.56e5	-0.451e-3	-0.616e-4	-0.4519	-73401	-1
1.2e6	-0.775e-3	-0.616e-4	-0.7580	-123100	-1
7.5e6	-0.954e-3	-0.616e-4	-0.9547	-155050	-1
140e6	-0.997e-3	-0.616e-4	-0.9971	-162100	-1

The results obtained from the 3D ANSYS formulation are compared with the 2D model results. The force ratio variation is compared with the modulus variation of the sensed object in both the cases. The comparison between the proposed 2D formulation and 3D ANSYS model has been shown in Figure 4.7. It is noted that both 2D and 3D models follow the similar pattern. The area ratio of the sensor was calculated and found out to be 11.60. It should be emphasized that the lambda parameter is a function of the thickness and Young's modulus of both compliant cylinder and sensed object and thus the variation of any of these parameters will affect the lambda.

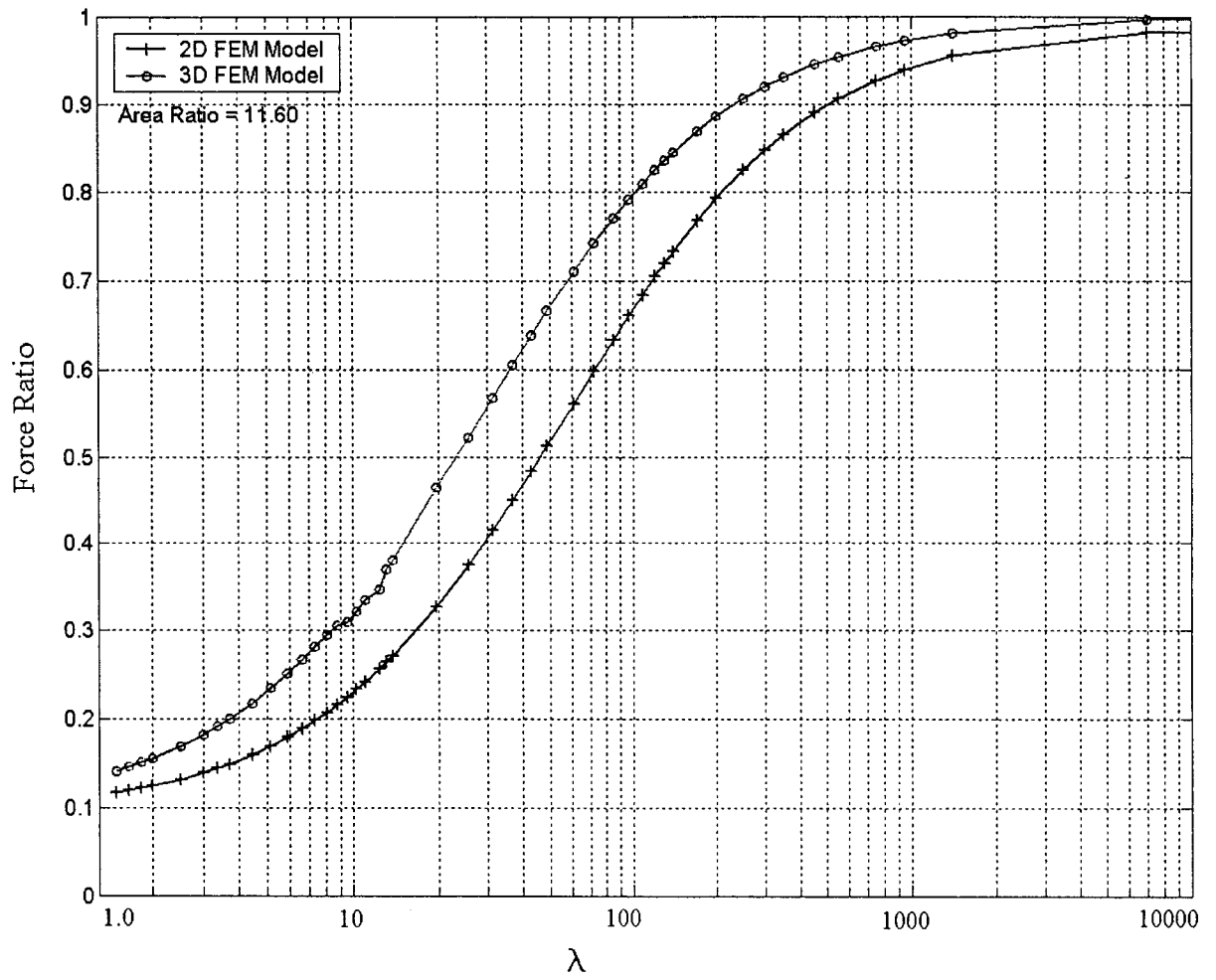


Figure 4.7 Force Ratio versus λ for the 2D and 3D model

In this study it is assumed that the thickness of the compliant cylinder and its modulus of elasticity and also thickness of the sensed object are constant. Therefore the variation of the λ can only be attributed to the modulus of the sensed object. Considering this, variation of force ratio can be directly studied with respect to modulus of elasticity of the sensed object as shown in the Figure 4.8.

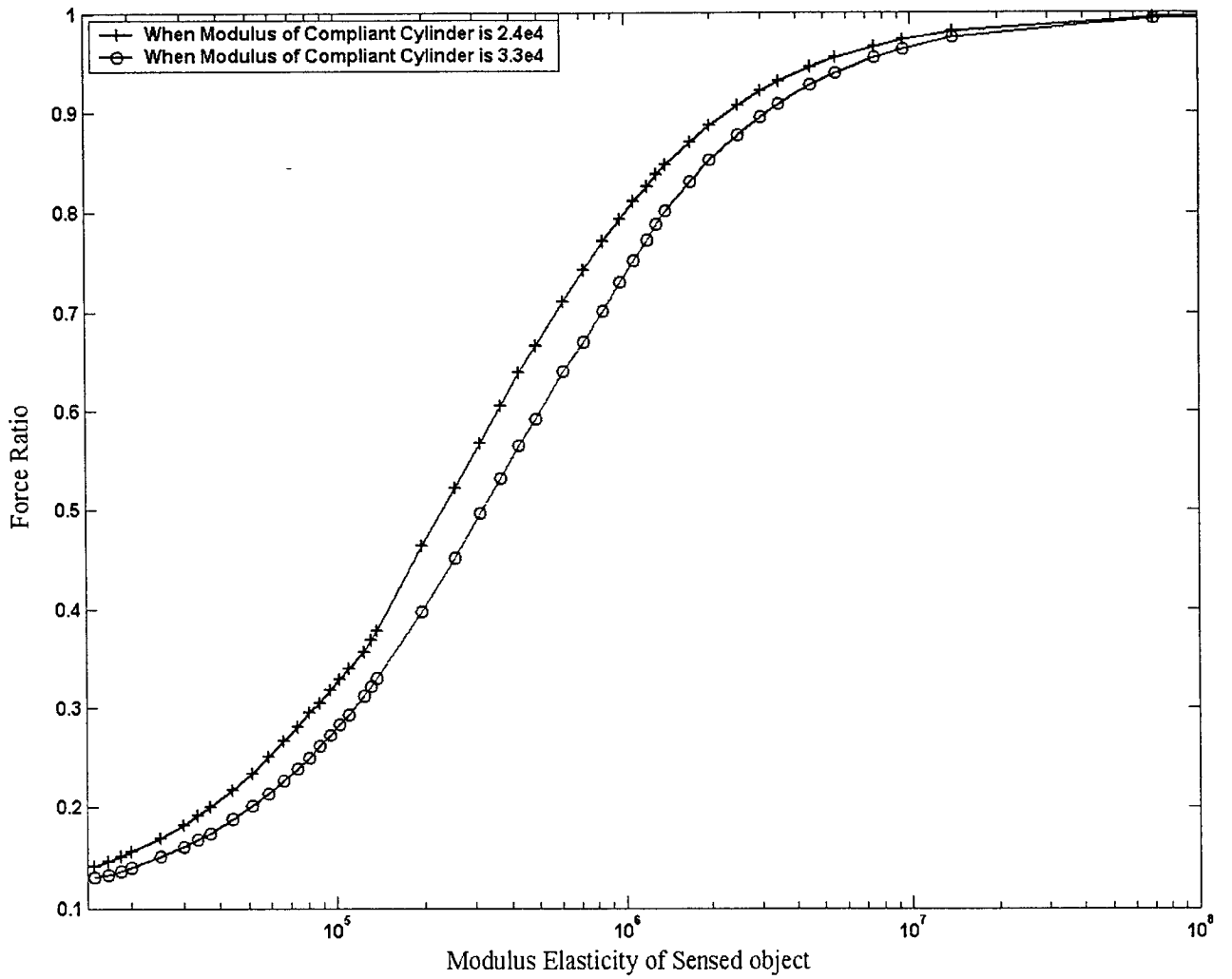


Figure 4.8 Effect of modulus of elasticity of sensed object on the force ratio at two different sets of compliant cylinder

Single sensor is not ideal to measure the compliance of the sensed object and force applied on the grasper. In the actual practical application, number of sensors is used for this purpose.

In this study, two cases were considered for the mounting of the sensor on the grasper plate. Both arrangements have advantages and disadvantages. In the first case,

grasper plate was made with different bases for every sensor, but in the second case it was joined together and made common base plate for the sensors. For the sake of simplicity the design of the grasper arrangements has been justified using two sensors mounted on the different base and common base

4.3 Design of Grasper with Different Base Plates

The first main problem is to measure the total force on the sensed object exerted by sensors mounted on the grasper. In different base plate arrangement, two sensors were placed together on the grasper plate with no interaction and binding in-between. Based on this design, it was possible to measure the local modulus of elasticity of the sensed object. Every sensor measures the local force on its top. The geometrical dimensions and design are shown in Figure 4.9. Although this design was found to be good in measuring the compliance at each local point, it has big drawback in manufacturing, which makes it less practical.

The model consists of two different sensors mounted on the same base plate. Each sensor has its own PVDF film, which measures the total force on the top of sensor. The force experienced by the rigid part in sensor is measured from the voltage response generated by the circular PVDF films below each part. The data obtained from different base sensor under uniform distributed load of 1N are given in Table 4.3. These results give the local modulus of the sensed object. The force ratio “ $\left| \frac{F_{\text{rigid_cylinder}}}{F_{\text{total_force}}} \right|_{\text{For each sensor}}$ ” gives the local modulus at given sensor position. For calculating the net modulus of elasticity, average values for all mounted sensors have been taken. As discussed before in Figure

4.8, the net modulus of elasticity of sensed object is directly proportional to the force ratio.

$$\text{Net-Modulus} \propto \frac{\frac{F_1}{F_{\text{total at 1}}} + \frac{F_2}{F_{\text{total at 2}}} + \dots + \frac{F_N}{F_{\text{total at } N^{\text{th}}}}}{N} \quad (4.31)$$

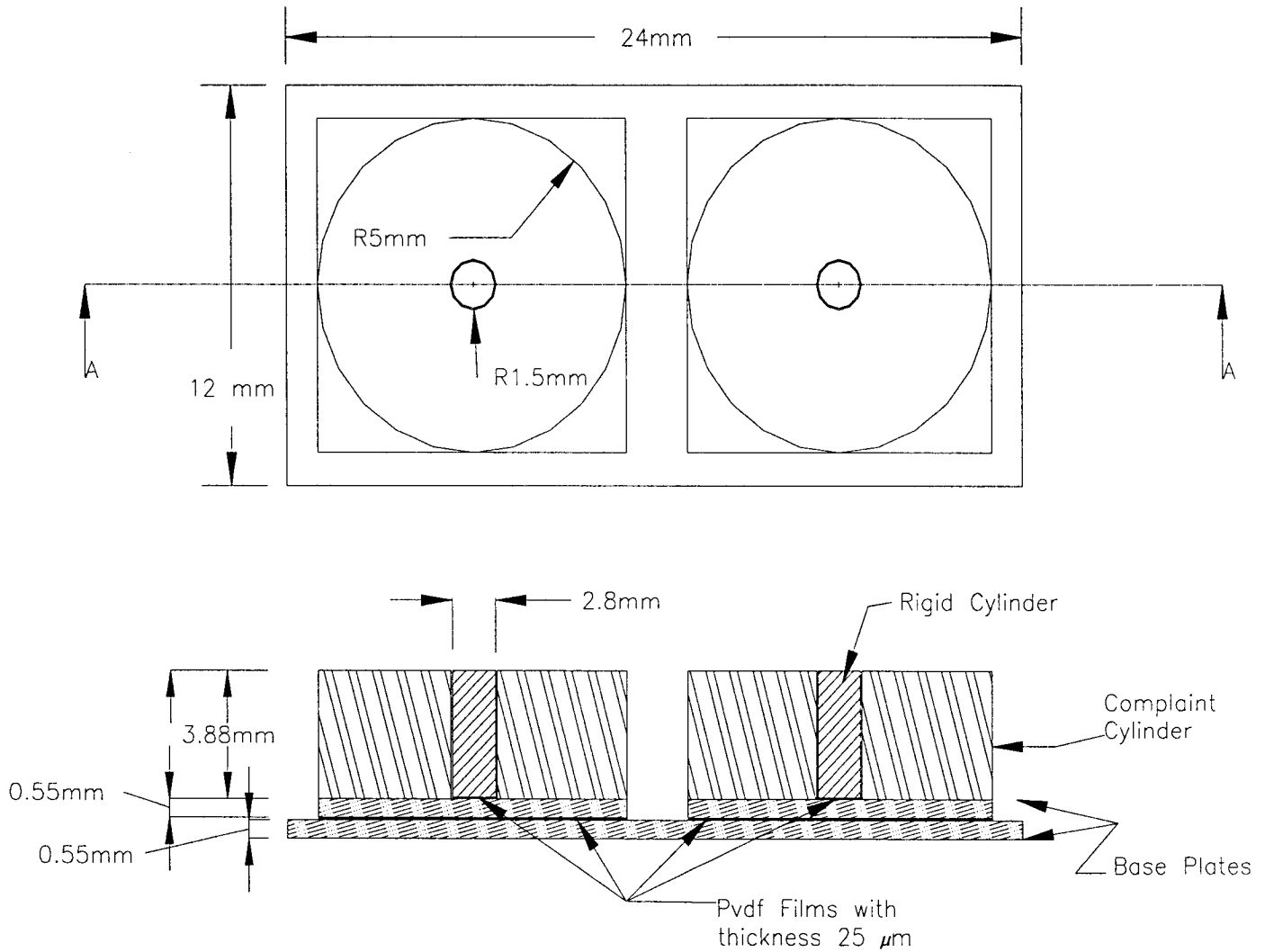


Figure 4.9 Design of the two sensors mounted on the different base plates.

The results obtained from this arrangement are supposed to be more reliable and exact. In the case of point force, using this design, it is very easy to locate the position of

the force and magnitude. The ANSYS was used for modeling the different base plate sensor. The data obtained from ANSYS for the different modulus of the sensed object is given in the Appendix II. The sample results are shown in Table 4.3 and Table 4.4 for two compliant cylinders having different modulus of elasticity. The PVDF-1 and PVDF-3 represent the circular PVDF films beneath the rigid cylinder on left and right side, respectively. The PVDF-2 and PVDF-4 measure the total force on each sensor below rectangular base plates. The total force applied by the grasper on the sensed object was calculated by adding the force on each sensor. The results for the force ratio calculated from equation 4.31 versus modulus of elasticity of the sensed object are shown in Figure 4.10.

Table 4.3 Voltages generation and forces distribution on the two circular PVDF films in different base model with compliance cylinder modulus of $2.4 \times 10^4 \text{ N/m}^2$

Sensed Object N/m^2	Voltage		Force		Force Ratio		Total Ratio
	PVDF 3	PVDF 4	PVDF 3	PVDF 4	Left	Right	
1.49×10^4	-0.440e-4	-0.44e-4	-0.04289	-0.04289	-0.08578	-0.08578	-0.08578
3.35×10^4	-0.604e-4	-0.604e-4	-0.05833	-0.05833	-0.11660	-0.11660	-0.11660
9.54×10^4	-0.107e-3	-0.107e-3	-0.10290	-0.10290	-0.20580	-0.20580	-0.20580
2.56×10^5	-0.192e-3	-0.192e-3	-0.18539	-0.18539	-0.37078	-0.37078	-0.37078
1.2×10^6	-0.371e-3	-0.371e-3	-0.35838	-0.35838	-0.71676	-0.71676	-0.71676
7.5×10^6	-0.486e-3	-0.486e-3	-0.46966	-0.46966	-0.93932	-0.93932	-0.93932
140×10^6	-0.516e-3	-0.516e-3	-0.49820	-0.49820	-0.99640	-0.99640	-0.99640

Voltage at PVDF-2 and PVDF-4 = 0.313×10^{-4}

Total Force on each Sensor-1 and Sensor-2 = - 0.5 N.

Table 4.4 Voltages generation and forces distribution on the two circular PVDF films in different base model with compliance cylinder modulus of $3.3 \times 10^4 \text{ N/m}^2$

Sensed Object N/m^2	Voltage		Force		Force Ratio		Total Ratio
	PVDF 1	PVDF 3	PVDF 1	PVDF 3	Left	Right	
1.49×10^4	-0.407e-4	-0.407e-4	-0.03937	-0.03937	-0.07874	-0.07874	-0.07874
3.35×10^4	-0.527e-4	-0.527e-4	-0.05088	-0.05088	-0.10176	-0.10176	-0.10176
9.54×10^4	-0.883e-4	-0.883e-4	-0.08535	-0.08535	-0.17070	-0.17070	-0.17070
2.56×10^5	-0.160e-3	-0.160e-3	-0.1542	-0.1542	-0.3084	-0.3084	-0.3084
1.2×10^6	-0.336e-3	-0.336e-3	-0.3250	-0.3250	-0.6500	-0.6500	-0.6500
7.5×10^6	-0.475e-3	-0.475e-3	-0.4592	-0.4592	-0.9184	-0.9184	-0.9184
140×10^6	-0.515e-3	-0.515e-3	-0.4976	-0.4976	-0.9952	-0.9952	-0.9952

Voltage at PVDF-2 and PVDF-4 = 0.313×10^{-4}

Total Force on each Sensor-1 and Sensor-2 = - 0.5 N

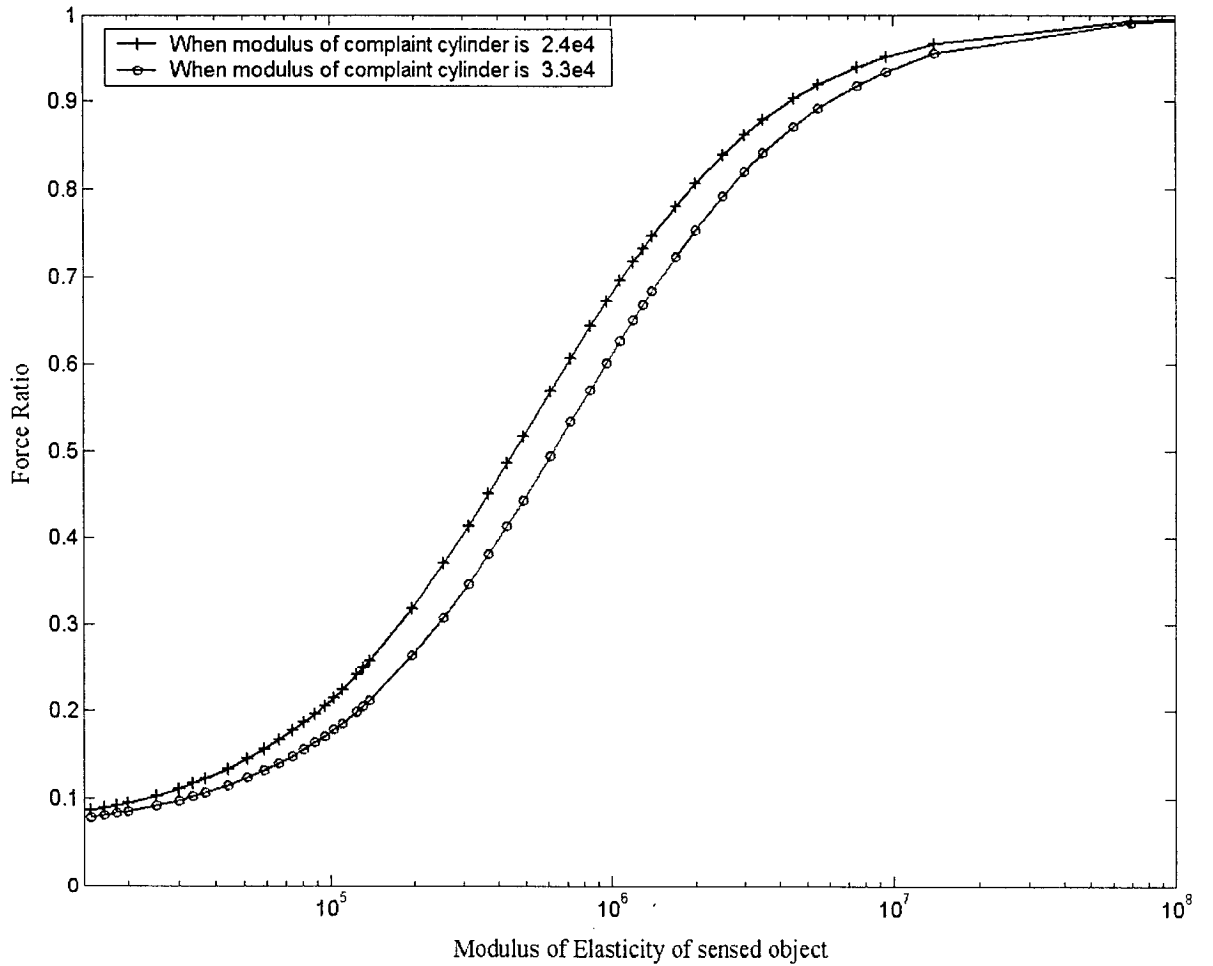


Figure 4.10 Effect of modulus of elasticity of sensed object on the force ratio of grasper with two sensors having different base at two different sets of compliant cylinder.

4.3.1 Limitation of Design of Grasper with Different Base Plates

The following limitations exist to practically implement the design of grasper with different base plates:

1. It is very hard to put so many PVDF films on grasper to measure the total force on each sensor, separately.
2. The number of electrical connections required for measuring the forces is $4 \times$ number of the sensor.
3. Electrical circuit is also complicated for too many electrodes.
4. Miniaturization for such a system is very cumbersome.

To overcome these limitations, a new design based on common base plate for the grasper has been proposed. The total force is measured by the single PVDF film sandwiched between common plexiglas plates.

4.4 Design of Grasper with Common Base Plate

Considering all these limitations, a new grasper design with common base plate has been proposed. In this design PVDF was sandwiched between two plates, which measure the total force on grasper rather than measuring force on each sensor. The design of two sensors arranged in this configuration is shown in Figure 4.11a. The fabricated common base sensor is also shown in Figure 4.11.b. Black and white portion in the photograph represents the rigid and compliant cylinder of the common base sensor. This design is easy to implement practically. The design can be extended to 'N' number

of sensors. In this design the total force is measured by PVDF film sandwiched between the plexiglas plates and the local force is measured by circular PVDF film. The interpretation of modulus of elasticity is defined by ratio of sum of all the force experienced by rigid cylinders to the total global force applied:

$$\text{Net Modulus} \propto \frac{F_1 + F_2 + \dots \dots \dots \dots \dots \dots \dots \dots \dots \dots F_n}{F_{total}} \quad (4.32)$$

The ANSYS results obtained for grasper with common base are presented in the Appendix II for two compliant cylinders having different modulus of elasticity. Table 4.5 and Table 4.6 are tabulated from the ANSYS results of Appendix II for some selective set of the values. The PVDF-1 and PVDF-2 represent the circular PVDF films beneath the rigid cylinders on left and right sides, respectively. The PVDF-3 measures the total force on the grasper. The uniform distributed 1 N load was applied to the grasper. The net force ratio was calculated as given by the equation 4.32 and its variation with respect to the modulus of elasticity of the sensed object is shown in Figure 4.12. It is noted that with this design, the number of electrodes and electrical connection also reduced to 2(N +1).

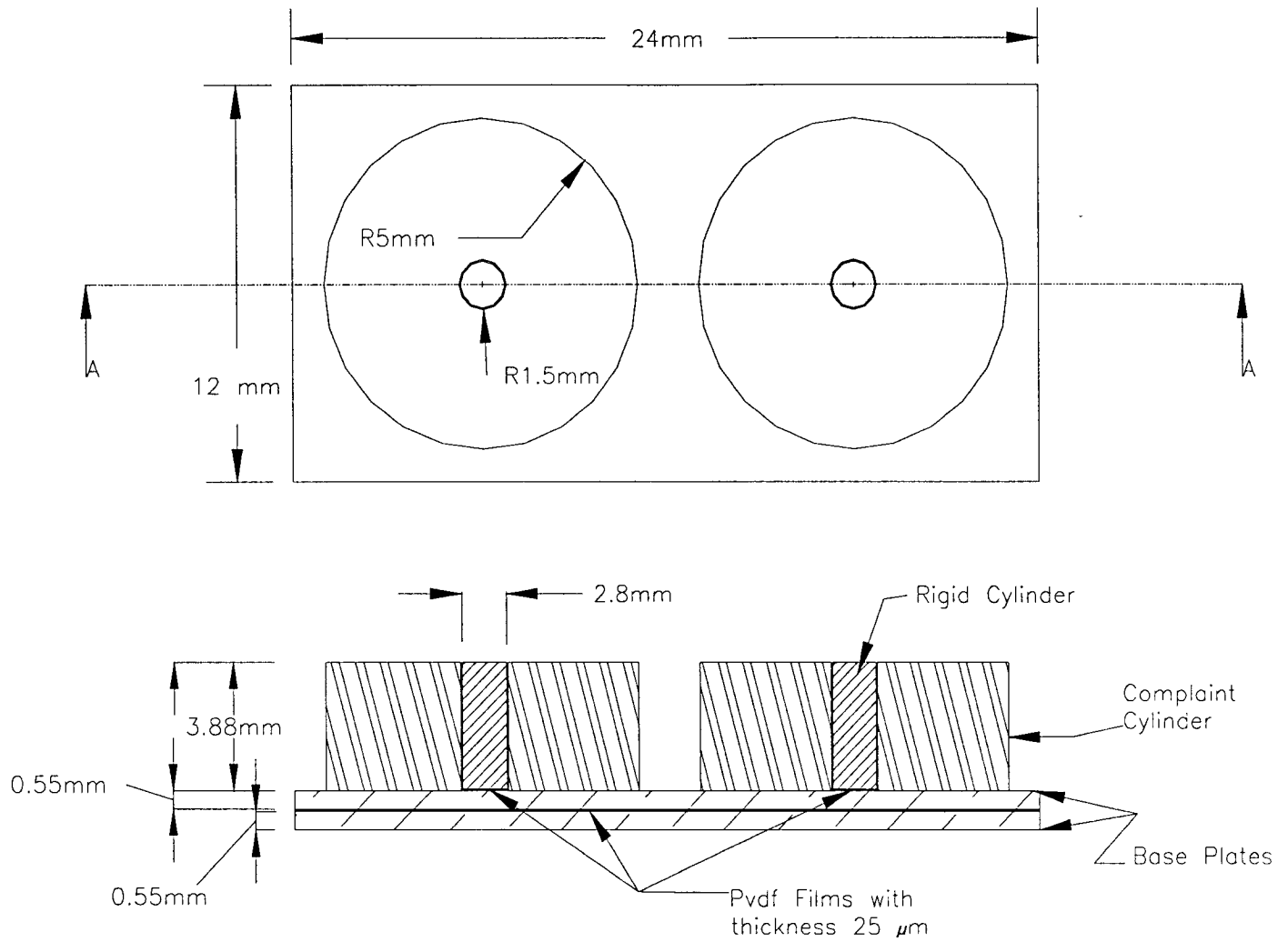


Figure 4.11a Design of the two sensors mounted on the common base plates.

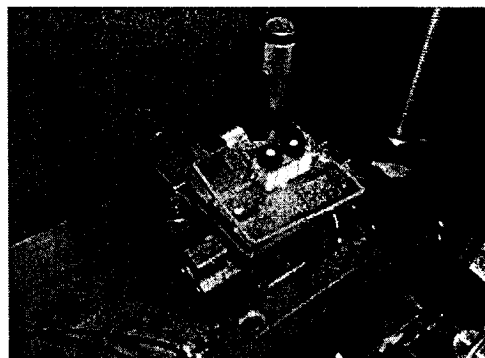


Figure 4.11b Photograph of the manufactured common base sensor.

Table 4.5 Voltages generation and forces distribution on the two circular PVDF films in common base model with compliance cylinder modulus of $2.4 \times 10^4 \text{ N/m}^2$.

Sensed Object N/m^2	Voltage		Force		Force Ratio
	PVDF 2	PVDF 3	PVDF 2	PVDF 3	
1.49×10^4	-0.440e-4	-0.44e-4	-0.04289	-0.04289	-0.08578
3.35×10^4	-0.604e-4	-0.604e-4	-0.05833	-0.05833	-0.11660
9.54×10^4	-0.107e-3	-0.107e-3	-0.10290	-0.10290	-0.20580
2.56×10^5	-0.192e-3	-0.192e-3	-0.18539	-0.18539	-0.37078
1.2×10^6	-0.371e-3	-0.371e-3	-0.35838	-0.35838	-0.71676
7.5×10^6	-0.486e-3	-0.486e-3	-0.46966	-0.46966	-0.93932
140×10^6	-0.516e-3	-0.516e-3	-0.49820	-0.49820	-0.99640

Total Force Applied to the Grasper = -1 N

Voltage Generated by PVDF-3 = -0.213×10^{-4} volt

Table 4.6 Voltages generation and forces distribution on the two circular PVDF films in common base model with compliance cylinder modulus of $3.3 \times 10^4 \text{ N/m}^2$.

Sensed Object N/m^2	Voltage(V)		Force(N)		Force Ratio
	PVDF 2	PVDF 3	PVDF 2	PVDF 3	
1.49×10^4	-0.407e-4	-0.407e-4	-0.03937	-0.03937	-0.07874
3.35×10^4	-0.527e-4	-0.527e-4	-0.05088	-0.05088	-0.10176
9.54×10^4	-0.883e-4	-0.883e-4	-0.08535	-0.08535	-0.17070
2.56×10^5	-0.160e-3	-0.160e-3	-0.1542	-0.1542	-0.3084
1.2×10^6	-0.336e-3	-0.336e-3	-0.3250	-0.3250	-0.6500
7.5×10^6	-0.475e-3	-0.475e-3	-0.4592	-0.4592	-0.9184
140×10^6	-0.515e-3	-0.515e-3	-0.4976	-0.4976	-0.9952

Total Force Applied to the Grasper = -1 N

Voltage Generated by PVDF- 3 = -0.213×10^{-4} volt

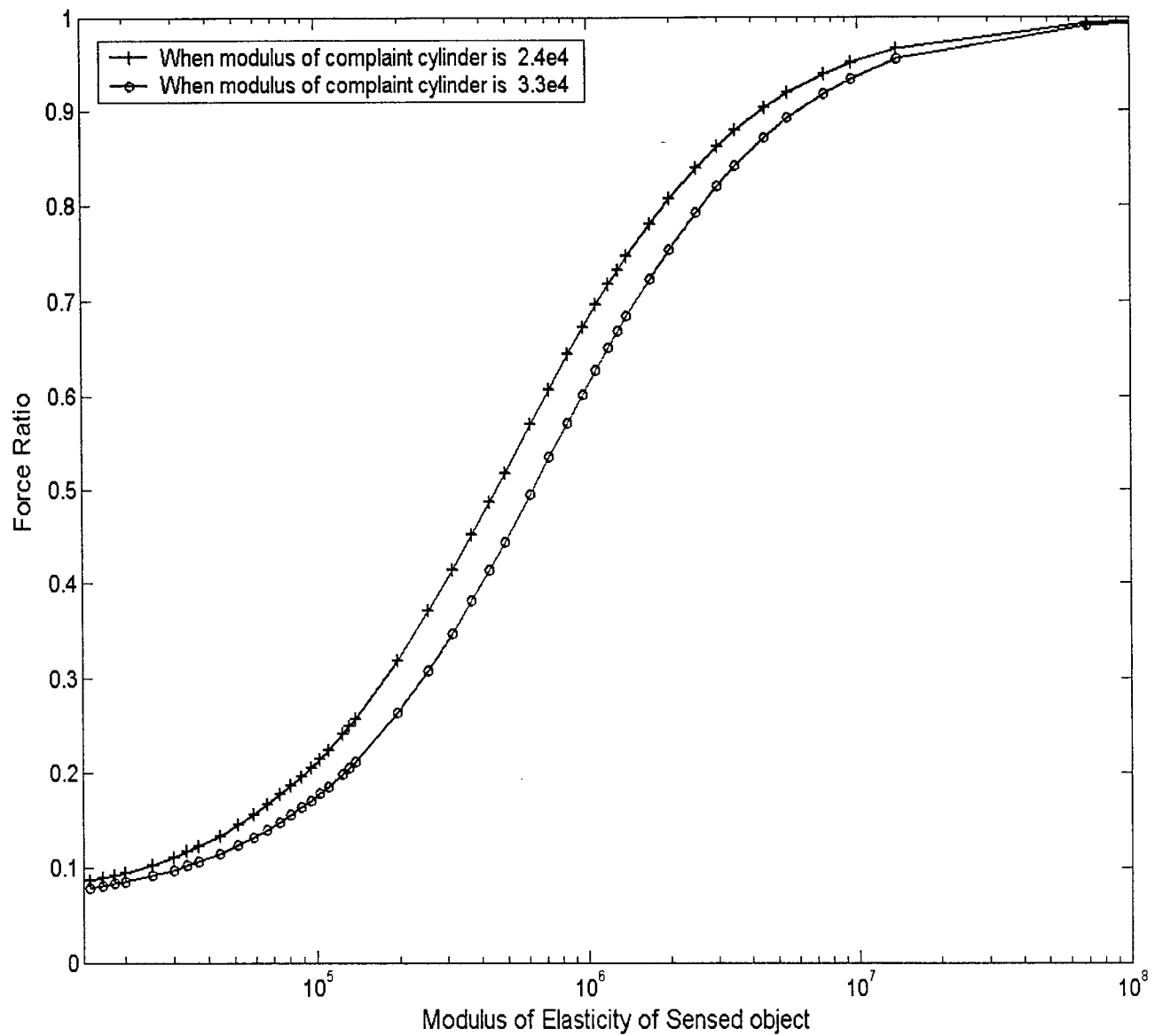


Figure 4.12 Effect of modulus of elasticity of sensed object on the force ratio of grasper with two sensors having common base at two different sets of compliant cylinder

4.5 Comparison of Theoretical Results

The results obtained from the theoretical analysis of 2D proposed model and 3D ANSYS model as well as the results extracted from the common base plate and different base plate are discussed and compared under uniform distributed load.

4.5.1 Comparison of 2D Model with 3D Model

It was shown that the force ratio of the sensor depends on the thickness of compliant cylinder and sensed object, modulus of elasticity of the sensed object and the compliance cylinder. These parameters are combined in one a constant called lambda function. As mentioned before in this study, we have only focused on the effect of modulus elasticity of the sensed object. The area-ratio of the sensor is set to 11.60. This ratio is constant throughout the calculations. The sensor dimensions were predetermined using analytical approach. The thickness and modulus of elasticity of compliant cylinder for single sensor were assumed to be constant for different arrangements. Only the variation of modulus of elasticity of the sensed object was taken into consideration for comparison of the results. The results obtained from 2D proposed formulation implemented in MATLAB are compared with the 3D ANSYS model for the single sensor design. The variation of the force ratio versus modulus of elasticity of the sensed object for two different modulus of elasticity of the complaint cylinder is shown in Figure 4.13 and 4.14. It is noted that good agreement exists between 3D ANSYS model and the proposed 2D model implemented in MATLAB. Both plots 2D and 3D models follow

same pattern of variation but differ in magnitudes. It is clear that the variation of the modulus of elasticity is large as compared to the force ratio, thus a logarithmic scale for X-axis has been used to accommodate large modulus of elasticity. The results obtained for 3D model from ANSYS give higher force ratio as compared to the 2D model. The minor difference between results obtained from 2D and 3D models can be attributed to the following assumptions considered for 2D model:

1. The sensed object on the top of the sensor was considered as 2D beam element.
2. The area of the circular section was taken proportional to the rectangular area in beam element.
3. The length of the element was also calculated in the reference to the area.

The 3D ANSYS results are based on the exact configuration of the sensor and sensed object. Thus, the 3-Dimensional analysis of the sensor is more reliable. To better realize the overall effects, Figure 4.13 and Figure4.14 are combined in the one Figure as shown in the Figure 4.15.

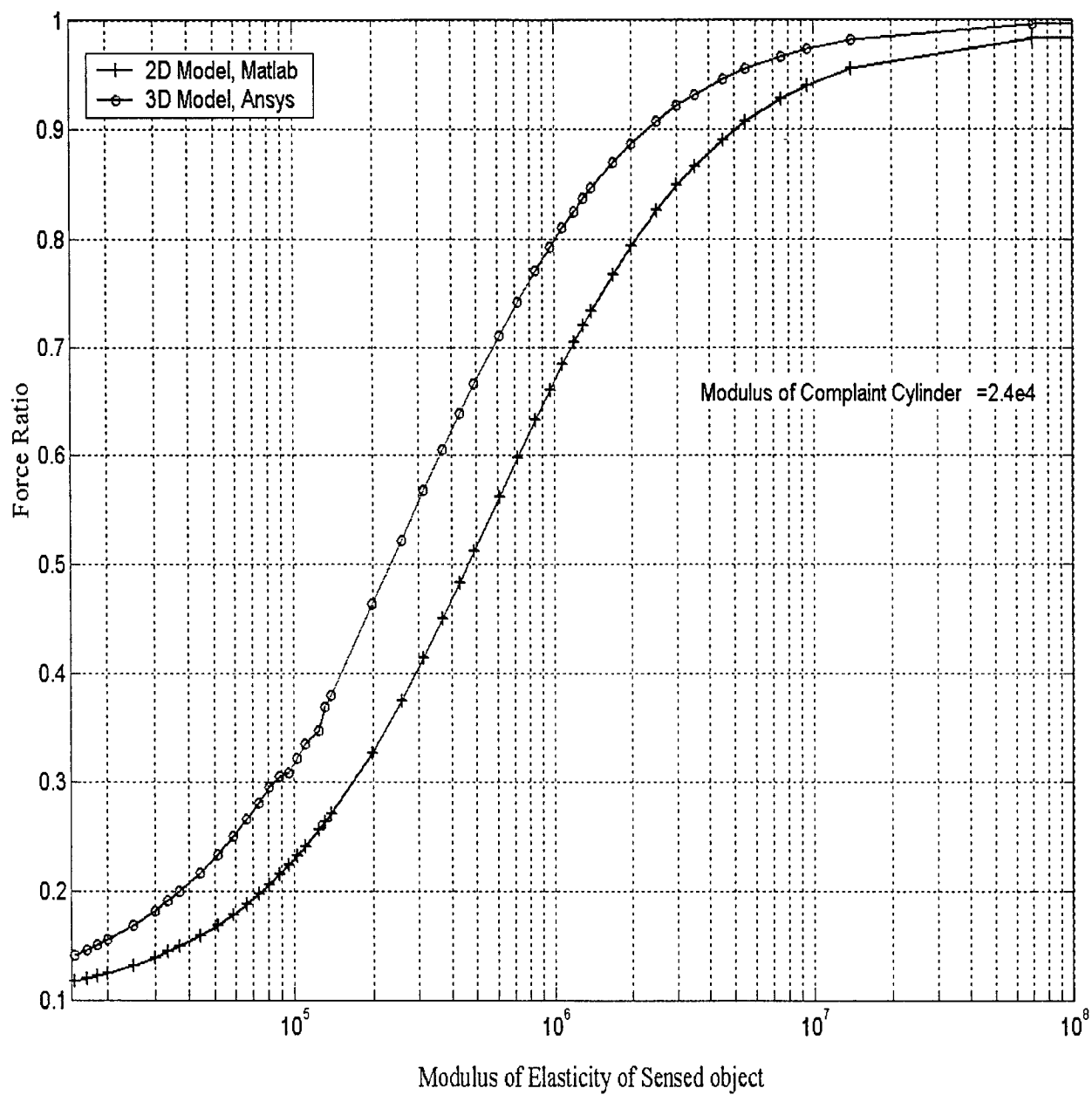


Figure 4.13 Variation of force ratio with modulus of elasticity of sensed object at compliance of cylinder 2.4×10^4 .

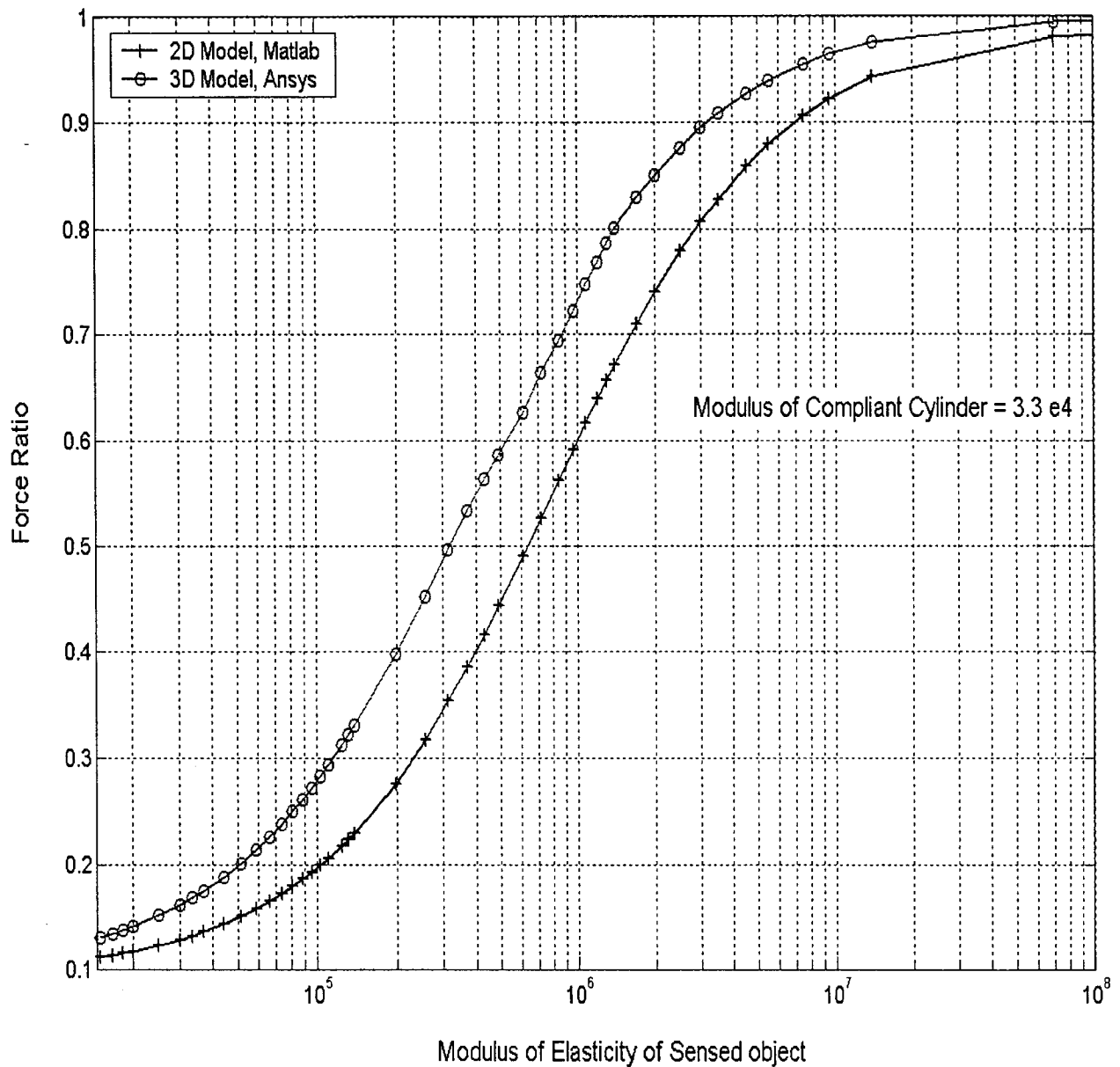


Figure 4.14 Variation of force ratio with modulus of elasticity of sensed object at compliance of cylinder 3.3×10^4 .

Comparing Figures 4.13 and 4.14, it can be concluded that higher values of the modulus of elasticity of compliance cylinder provide less force ratio response. If the compliant cylinder is hard, large portion of the applied load will be taken by the hard

compliant cylinder and therefore effect on the rigid cylinder is less causing less force ratio response.

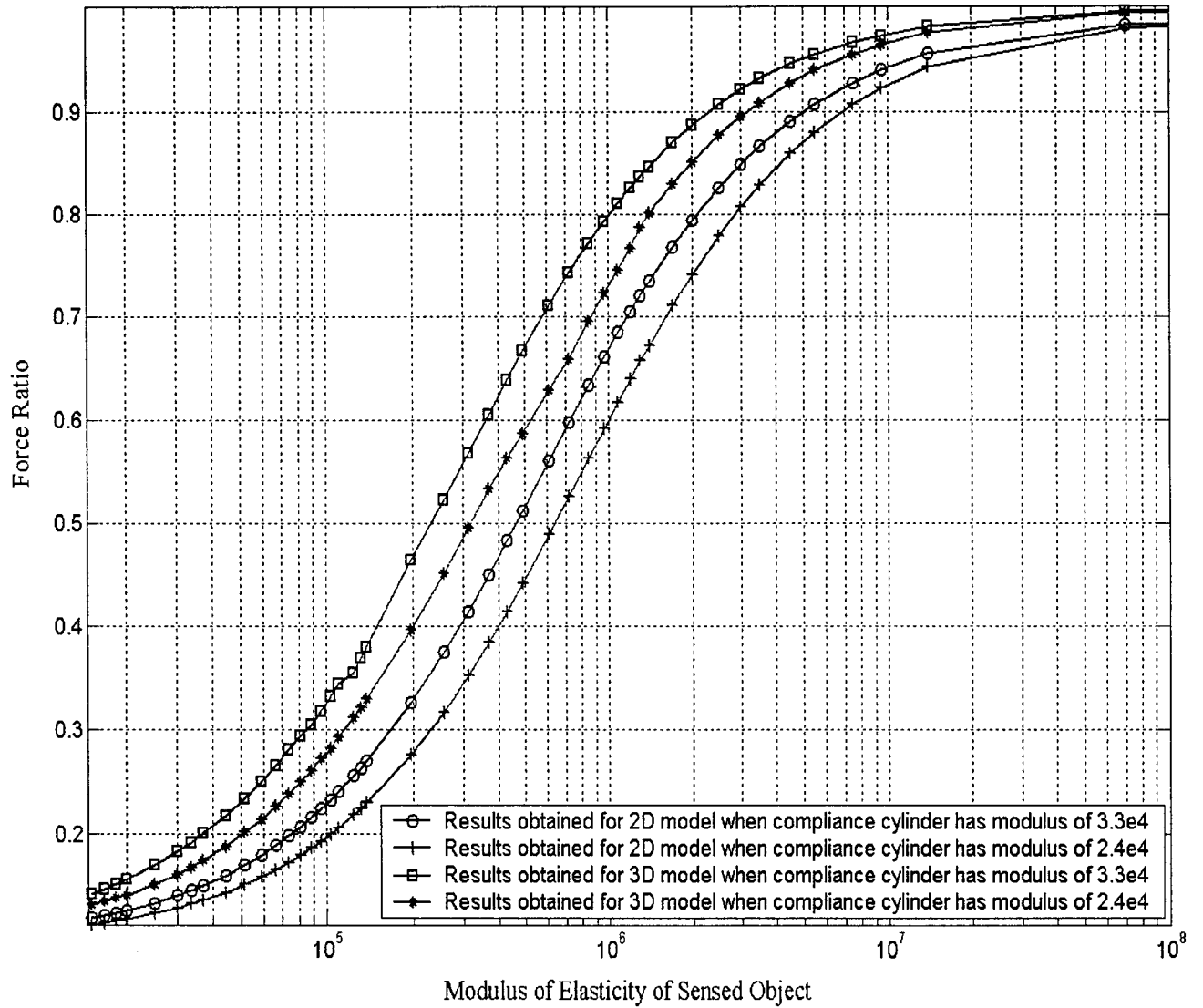


Figure 4.15 Variation of force ratio with modulus of elasticity of sensed object at two sets of compliant cylinders.

4.5.2 Comparison of Two Sensors on Different and Common Base Plate

In different base arrangement, sensors were mounted in the single sensor plate. Both sensors do not have any attachment with each other. The results obtained from the each sensor give only local modulus of elasticity of the sensed object at that position of the sensor. The average of all values obtained from different sensors gives the overall modulus of the sensed object. The uniform distributed load of 1N was applied at the top of sensed object in both cases. The force ratio of left hand side sensor and force ratio for right hand sensor was equal to each other. The average force ratio was then obtained, for complete system.

It is noted that the results obtained from grasper with different base are similar to the common base sensor under uniform distributed load as shown in Figure 4.16. Thus, in practical application, either way of designing the sensor can be used for grasper. The force ratio always lies within the limit (<1). To avoid the complexity of the manufacturing and installation problem, it is preferable to use grasper with common base. The grasper with common base serves the same purpose and easy to manufacture.

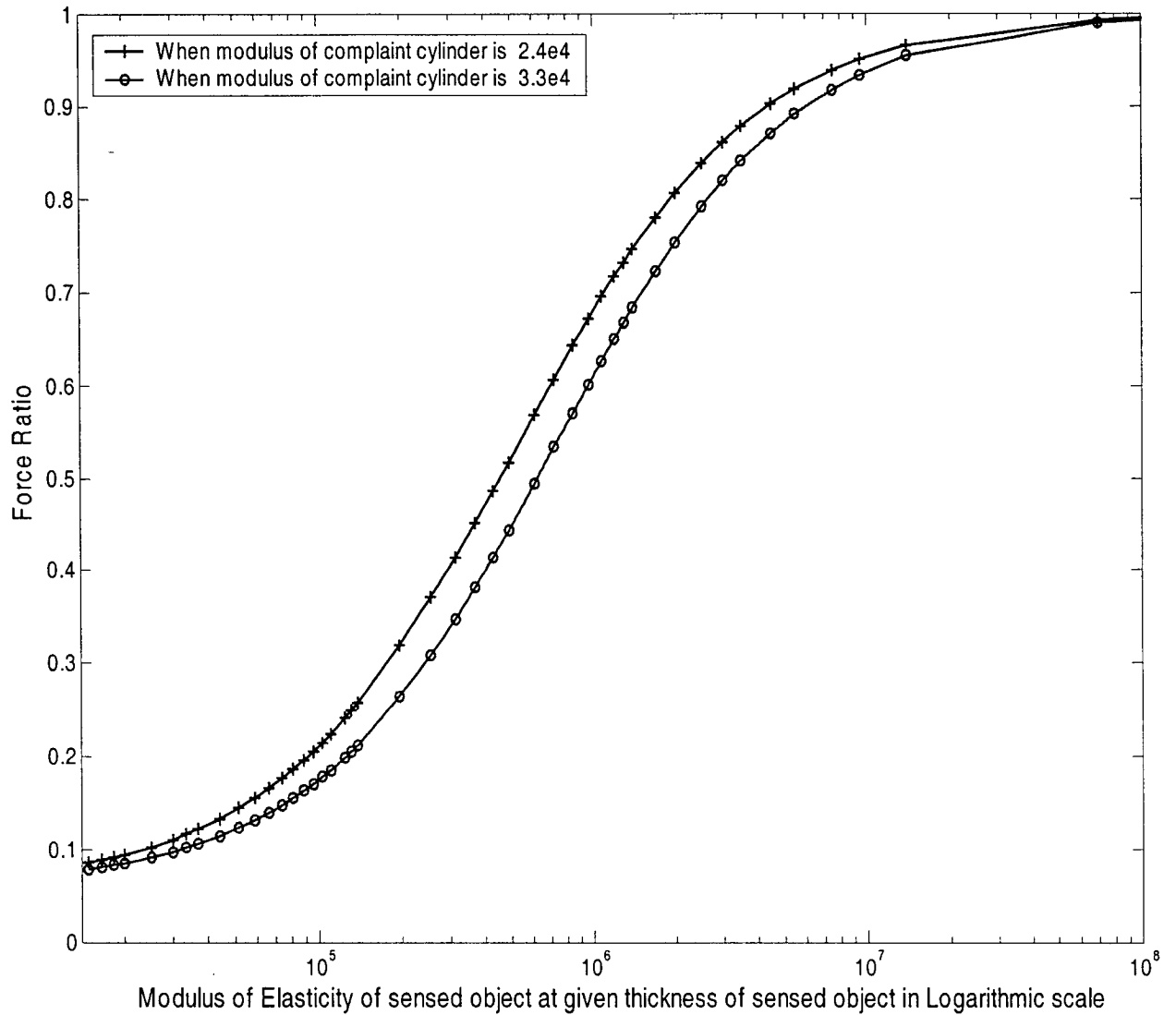


Figure 4.16 Comparison of two sensors on common base and different base plates.

4.5.3 Comparison of the Single Sensor and Two Sensor with Common Base

The single sensor results are compared with the results obtained from the two sensors mounted on the common base arrangement as shown in Figure 4.19. The modulus of the compliant cylinder is considered to be 2.4×10^4 Pa. It is noted that the single sensor shows higher force ratio as compared to the common base sensor. The

difference between results is mainly due to the bending action of the sensed object. In the common base sensor, the compliant cylinder provides the supportive action to the sensed object and hinder the free bending of the sensed object. In other words, force on the sensed object transmitted more to the compliant cylinder rather than the rigid cylinders causing the fore ratio to decrease.

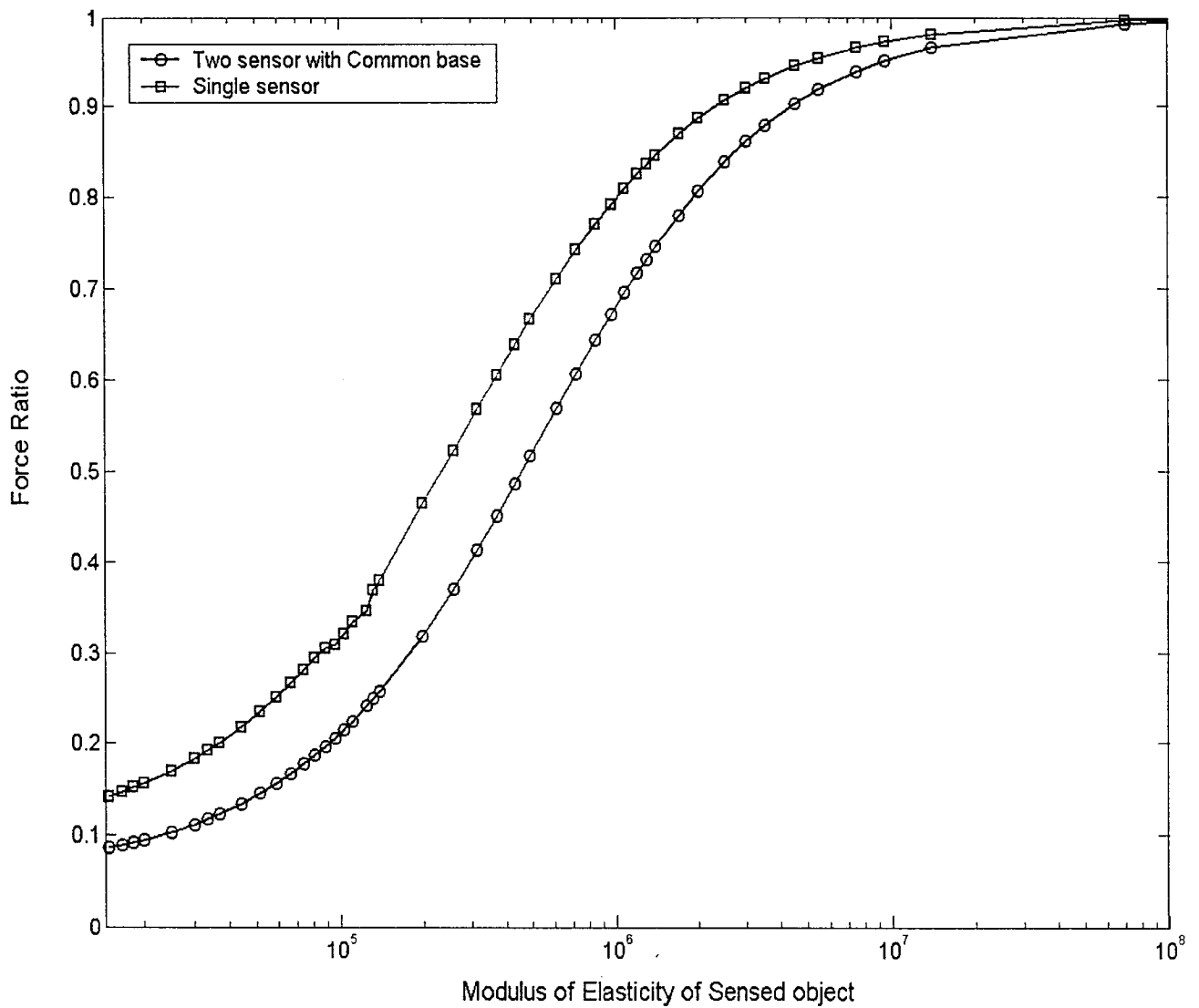


Figure 4.17 Effect of Modulus of elasticity of sensed object on the force ratio for single sensor and double sensor mounted on the common base

4.6 Novelty of Design

The single sensor can also act as tooth during the holding process. The measurement of the compliance of the tissue was based on the relative deformation of the compliant cylinder with respect to the rigid cylinder of the sensor. The relative deformation describes that the different force has been experienced by the rigid and compliant parts of the sensor. Thus the relative deformation is directly related to the force ratio. The higher the force ratio the less will be the relative deformation. Applying the force to the sensor, the compliant part deforms and rigid part remains un-deformed. Therefore rigid part protrudes outward and acts as tooth. The protruded rigid part of sensor is shown in Figure 4.18. Considering this the proposed sensor has built in character to behave as a tooth for grasping purposes. The size of the endoscope grasper varies in the range of few centimeters depending upon the requirement and purpose of the grasper. The size of the sensor on the grasper depends upon the sensitivity and precision requirement of the instrument. In practical application, one sensor cannot serve the purpose for measuring the compliance of tissue and grasping purpose. A number of sensors at different locations on the grasper measures the compliance and to hold the tissue securely. The micromachining techniques are required for further improvement on arrangement of the sensors on the grasper.

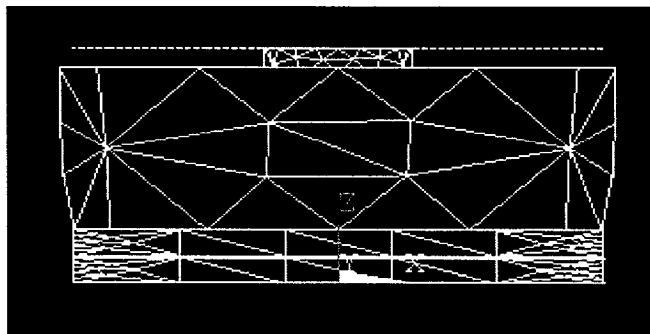


Figure 4.18 Single sensor acts as teeth

Chapter 5

Experimental Results and Comparison

In this chapter the discussion on the experimental results and comparisons with the theoretical results are carried out. The complete procedure of the experimental setup and calibration of the instruments are discussed. Different sensed objects are used for testing purposes at given compliance of the outer cylinders. The modulus of the sensed objects has been checked using the load cell. The calculation of the modulus of elasticity of different objects is also discussed. Experiments have been performed on the single sensor and two sensors with common base and different base sensor, respectively. At the end of this chapter, all the experimental results are compared with the theoretical results.

5.1 Experimental Analysis

The layout of the experimental setup and the photograph of the rig are shown in Figure 5.1a and Figure 5.2b, respectively. A power amplifier has been used to condition signal generated by the signal generator. That conditioned signal is then used to drive vibrator. A sinusoidal signal with the frequency of 10 Hz has been used in these experiments. Tactile sensors should be capable of measuring the frequency of sensor from range 0 Hz -20 Hz [34]. This range depends upon the application of the tactile sensor. It is noted that in the actual practice, the working frequency of the tactile sensor is around 10 Hz. A micro-positioner has been used to position the sensor relative to the position of the probe. Both static load and dynamic applied load measured through the load cell, positioned between the

probe and the shaker. The signal obtained from the tactile sensor is directed to the charge amplifier for the required amplification and measured on an oscilloscope. The signal of the vibrator and amplified signal of tactile sensor are monitored in an oscilloscope. Before performing the experiment with the different samples, it was necessary to calibrate the instruments.

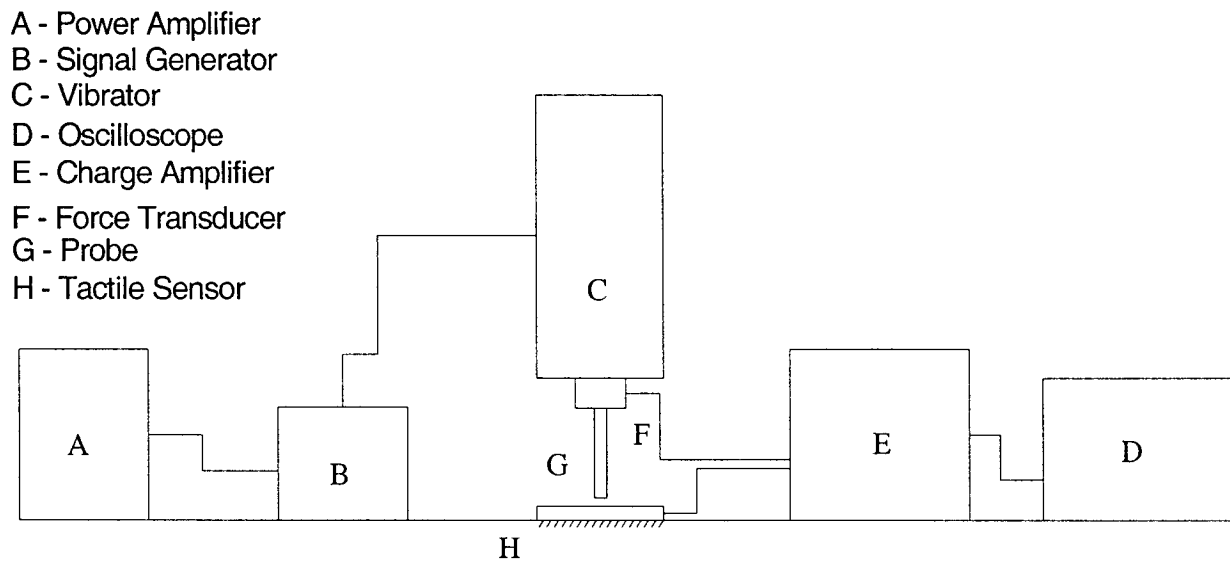


Figure 5.1a Schematic diagram of the experimental setup for measuring the response of the tactile sensor under dynamic loading

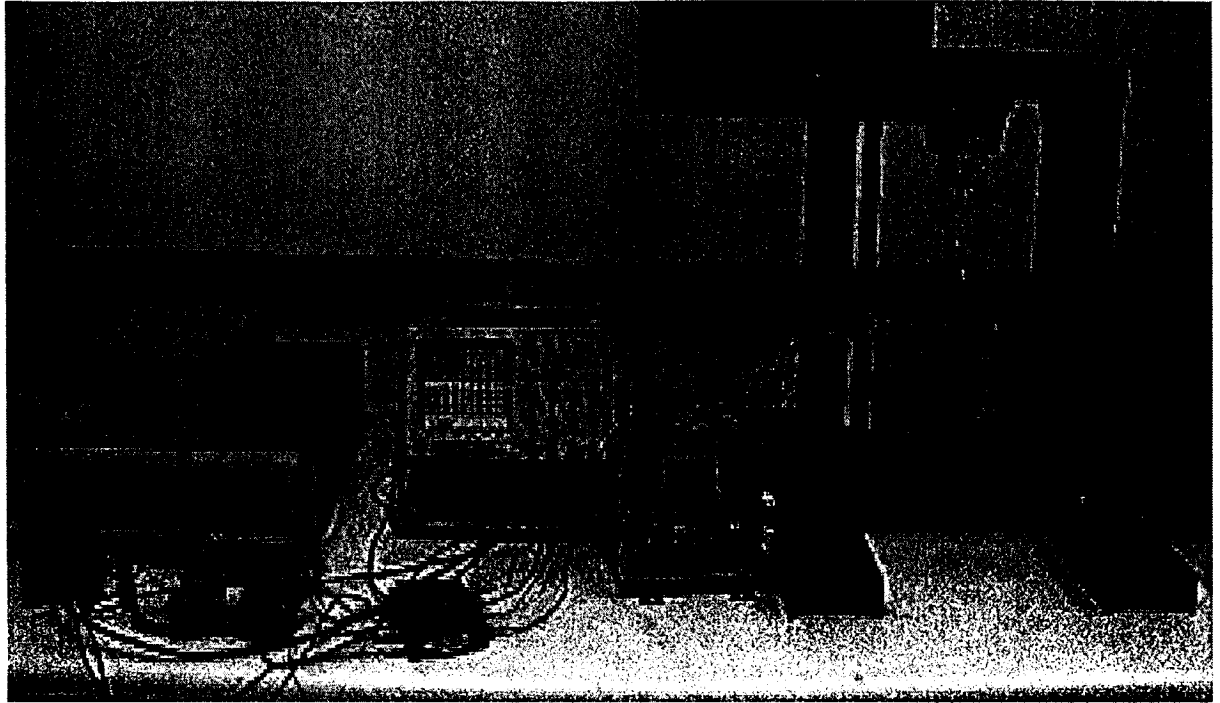


Figure 5.1b Layout for the experimental setup for measuring the response of the tactile sensor under dynamic loading

5.2 Calibration of the Load Cell

Before starting the experiment, it is extremely necessary to calibrate the instruments and find the sensitivity of the load cell. The calibration of the load cell was carried out using standard weights. First, the load cell was mounted on the vibrator, then the output is fed into the strain gage meter for measurement. This signal is then was seen on an oscilloscope. The strain gage meter worked on the principle of the Wheatstone bridge, which is discussed in Appendix III. The load cell was loaded and unloaded. The gage factor of the strain gage meter was set to 8.98. Display of the LED of the strain gage meter has been set to zero using the keys provided on the strain indicator. The significance of the zero value is for balancing full Wheatstone bridge. The output readings at the loading and unloading points have been recorded for the calibration of the instruments.

The data obtained for the calibration are given in Table 5.1 for loading and unloading conditions. The sensitivities of the strain indicator has been found to be 0.1053 mV/N. Once calibration is performed, the moduli of elasticity of the samples have been verified under compression test.

Table 5.1 Calibration data for the Strain Indicator

		Loading	Unloading	Average load/unload	Sensitivity
	Load (gms)	Strain gage Meter (mV)	Strain gage Meter(mV)	Strain gage Meter(mV)	Strain gage Meter(mV/N)
1	140	16	16	16	0.11428
2	240	26	26	26	0.10833
3	340	36	36	36	0.10588
4	440	47	46	46.5	0.10568
5	540	56	57	56.5	0.10462
6	640	67	66	66.5	0.10390
7	740	77	76	76.5	0.10337
Average					0.105530

5.3 Measurement of Modulus of Elasticity

The modulus of elasticity of the sensed object has been measured by applying load and measuring strain. This was done by using the load cell and a circular probe of radius 1 cm. Circular specimens were cut into the same size as the diameter of the probe. The readings from the micro-positioner and strain gage meter provided the deflection and load on the specimen, respectively. Six rubber samples were used. Out of these rubber samples, properties of the five samples are known and one unknown. The rubber samples are numbered as 1-6. The result for sample 1 (white silicone rubber) has been shown in Table 5.2. The specimens of 1 cm radius and 3 mm thickness have been used:

$$\text{Area of specimen} = \pi(D)^2 / 4 = 3.14 (10^{-2})^2 / 4 = 7.85 \times 10^{-5} \text{ m}^2$$

$$\text{Thickness of Specimen} = 3 \text{ mm}$$

$$\text{Stress} = X(124.9) \text{ Pa}$$

$$\text{Strain} = Y / \text{thickness} = Y / 3$$

$$\text{Initial reading on the meter} = -2$$

$$\text{Initial reading on the micro positioner} = 19.475 \text{ mm}$$

where X and Y are the reading of the voltage on the meter and deflection in specimen, respectively. The experimental values of the modulus of elasticity under compression deflection test obtained from the experimental results have been compared with the known technical data provided by the manufacturer given in Table 5.4. It is noted that good correlation exists between the experimental results and the known data within the range of compression test provided by the manufacturer. The value of the experimental compression test are found to be between 15.92 and 16.61 psi, which exactly lies between the range of the 12-20 psi provided by the manufacturer as shown in the Table 5.4. In a similar manner, same tests have been performed on the unknown specimen, sample-6, to find out the modulus of elasticity under compression deflection test value. The experimental data are given in Table 5.3. The thickness of the specimen is 4.70 mm and the area is $7.83 \times 10^{-5} \text{ m}^2$. The value of modulus of elasticity was calculated and found out to be around 14.88 psi, which was the highest amongst the samples. Similar experiments were performed on the other samples of the rubber for calculating the modulus of elasticity. It was found that values of the modulus of the elasticity under compression test for sample 2, 3, 4, 5 are 24131.65, 41368.54, 4823.30, 2579.03 Pa, respectively. The results of the tests for the modulus of the elasticity for the sample 1, 6 are as follows.

Table 5.2 Experimental results of the Modulus of elasticity for the white silicone rubber, sample 1

Deflection (mm)	Meter Reading	Strain	Stress (Pa)	Modulus of Elasticity (Pa)
19.30	-51	0.058	6369.9	109820.68
19.00	-143	0.158	17860.7	113042.41
18.90	-172	0.1916	21482.8	112123.17
18.60	-263	0.2916	32.848	112649.86
18.20	-386	0.425	48211.4	113438.58
18.00	-451	1.475	56329.9	114584.82

Table 5.3 Experimental results of the Modulus of elasticity for the unknown sample of rubber, sample 6

Deflection (mm)	Meter Reading	Strain	Stress (Pa)	Modulus of Elasticity (Pa)
20.6	-96	0.093	9223.38	99176.18
20.4	-146	0.1355	14027.2	103522
20.2	-187	0.1781	17966.3	100878.1
20	-227	0.2206	23050.6	104490.7
19.8	-273	0.2632	27498.1	104476.2
19.6	-314	0.3057	31627.9	103460.6

Table 5.4 Physical properties of the rubber specimens provided by the manufacturer

	1523	SC- 41	SC-42	G-231-N	Silicone
Sample no.	4 (Pa)	5(Pa)	3(Pa)	2(Pa)	1(Pa)
Polymer	Natural	NBR/PVC /NEO Blend	NBR/PVC /NEO Blend	Neoprene	Silicone
Compression Deflection Test	$3.45 \times 10^4 - 2.07 \times 10^4$	$2.07 \times 10^4 - 3.45 \times 10^4$	$2.76 \times 10^4 - 5.52 \times 10^4$	$1.38 \times 10^4 - 3.45 \times 10^4$	$8.28 \times 10^4 - 1.378 \times 10^5$
Tensile Test	$1.73 \times 10^5 - 1.86 \times 10^5$	3.44×10^5	5.17×10^5	5.17×10^5	3.44×10^5

5.4 Experimental Results

Once the experimental setup and calibration are accomplished, it is necessary to know the order of the samples with respect to their softness. The expected order of the softness is shown in Figure 5.2 based on the calculated values of the modulus of elasticity. These values are also in correlation within the range given by the manufacturer. Sample 1 is supposed to be at the top and sample 2 is at the extreme bottom. Sample 6 is placed in the softness order based on the calculated softness values obtained experimentally.

The experimental tests have been conducted on the single sensor, common base sensor and different base sensors, respectively. The experimental results obtained from the single sensor and two sensors with different arrangement are discussed in this section. Sample 2, has been used to fabricate the compliant cylinders all the three sensors i.e. single sensor, common base sensor and different base sensor. Details of the experimental results are given in the following sub-sections.

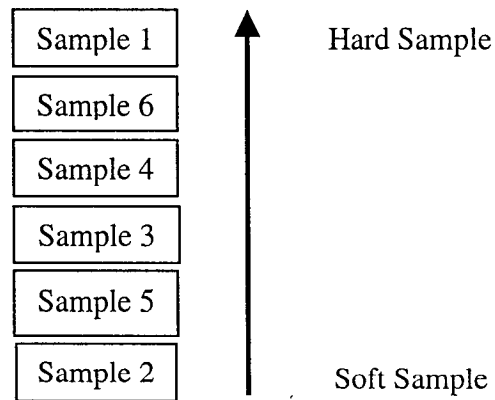


Figure 5.2 Expected order of the softness of the sample based on the technical data provided by the manufacturer

5.4.1 Single Sensor

Single sensor consists of the rigid cylinder surrounded by the compliant cylinder. PVDF-1 and PVDF-2 are representing the rectangular and circular PVDF films, respectively (see section 3.1.6). The leads from the PVDF-1 and PVDF-2 are connected to the charge amplifier for the required conditioning and then fed into the oscilloscope. The single sensor is mounted on the micro positioner that is placed beneath the load cell. The rubber samples with area of 1 cm^2 have been used as the sensed objects. The rubber sample is placed between the probe and sensor. Readings at the different load have been recorded to find out the variation of the force ratio.

Six load sets have been used and each sample has been tested under different load set to confirm the force ratio of the rigid part to the total force applied. In sample 1 and 6, sinusoidal output is very clear without any noise disturbances, it is clear that the hard materials provide better results. On the other hand, sample 2 and 5 show some noise in the output. This is because the soft rubbers are compressed more under small load and acted as vibration damper for the sinusoidal input. Soft rubber absorbs sinusoidal wave input and transmits distorted waveform to the PVDF films. This distorted waveform results in noise. This will provide the damped signal to the PVDF sensor. The data obtained for the six loads per sample are provided in Tables A2.9- A2.14 in Appendix II. A typical data for the single PVDF sensor at 3N load are shown in Table 5.5. The results confirm that different forces are experienced by the rigid part and compliant part and they vary proportionally. The output voltages from the PVDF films are measured in milli volts on the oscilloscope. From the force ratio, the compliance of the sample can be extracted. The higher the force ratio the more rigid is the sample and vice versa. In Figure 5.3, the samples are arranged depending on the

modulus of elasticity evaluated based on the obtained force ratio from the single sensor. Comparing Figure 5.3 with Figure 5.2, it is clear that order of the five known samples is the same as calculated in the previous section.

Table 5.5 Experimental results for single sensor at the 3N of load with different rubber samples

Experimental Data at Load 3N							
Sample No.	Meter Reading	Oscillo-scope	PVDF-2 (mV)	PVDF-1 (mV)	Force Rigid (N)	Total Force (N)	Force Ratio
1	32	32.02	5.87	213	0.964	3.074	0.329
2	32	31.80	2.484	206	0.432	3.121	0.139
3	32	32.09	3.290	212	0.573	3.212	0.178
4	32	32.85	4.304	218	0.742	3.334	0.223
5	32	34.20	2.983	200	0.514	3.059	0.168
6	32	32.80	5.018	214	0.873	3.088	0.283

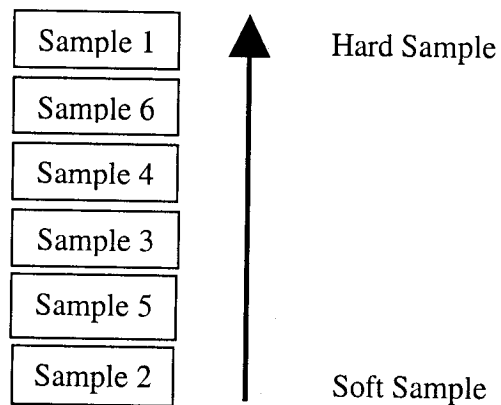


Figure 5.3 Softness of the sample depending on the experimental results obtained from single sensor

5.4.2 Two Sensors with Common Base

Similar experiments were performed on the two sensors mounted on the common base arrangement with six different samples of the rubber. Each rubber sample specimens was cut into the size of the 12 x 24 mm and 3mm thickness. Each rubber sample was placed under the uniform loading from 1.5 N to 4.5 N at an interval of 0.5 N.

The frequency of the sinusoidal applied load was 10 Hz. The experimental results obtained from common base sensor for each rubber sample are given in Tables A2.15- A2.20 in Appendix II.

The experimental data for each specimen of rubber at the uniform load of the 3N were abstracted from the appendix II and tabulated in the Table 5.6. In the case of the common base sensor, the force ratio is ratio of total forces on two rigid cylinders to the total force applied on the sensor. Force ratio is proportional to the softness of the sensed object. Figure 5.4 show the order of the six samples based on the force ratio. Depending on the force ratio obtained at 3N, specimens are arranged in the decreasing order of the hardness in Figure 5.4. As compared to the result obtained from single sensor positions of sample 3 and 5 are interchanged, respectively. The arrows shown in the figure represent the change in the position of the samples relative to the expected order. The position of sample 1, 2, 4 and 6 remain the same in both cases. The variation of the position of the 3 and 5 is not much in terms of numerical values of force ratio. Average value of force ratio for sample-5 is less than that of the sample-3 (refer to Tables A2.15-A2.20). Only force ratio value at 3N for sample 3 is slightly higher than the sample 5. This is due to the experimental error. But the average value of force ratio shows the same position as compared to single sensor and expected order.

Table 5.6 Experimental Results at the 3N of load with different samples of the rubbers, for common base sensor

Experimental Data at Load 3N									
Load 3N			mV	mV	mV	N	N	N	
Sample No.	Meter Reading	Oscillo-scope	PVDF 1	PVDF 2	PVDF 3	Force 1	Force 2	Total Force	Force Ratio
1	32	33.70	2.935	3.375	71.528	0.482	0.574	3.422	0.309
2	32	31.00	1.292	1.429	76.071	0.199	0.243	3.143	0.140
3	32	32.35	1.711	1.892	75.172	0.275	0.298	3.550	0.159
4	32	33.03	2.238	2.475	76.259	0.296	0.330	2.943	0.213
5	32	31.68	1.551	1.715	69.444	0.225	0.291	3.065	0.171
6	32	35.38	2.610	2.886	70.861	0.339	0.551	3.057	0.291

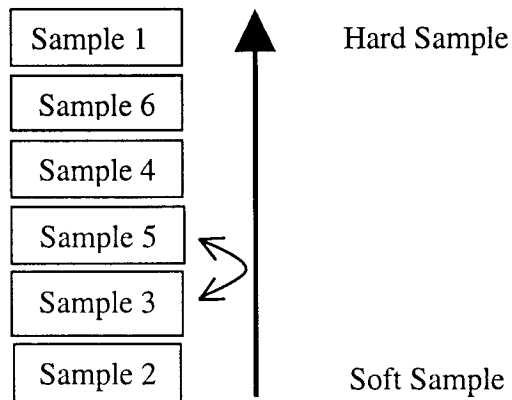


Figure 5.4 Softness of the sample depending on the experimental results, common base.

5.4.3. Two Sensors with Different Base

Softness order of the rubber samples was also measured using the different base sensor. As mentioned above, the single sensor and the common base sensor distinguish the softness of the test samples from each other. Experiment was also performed on the different base sensor. Total force on the different base sensor was measured by adding output from the rectangular PVDF film response of the individual sensor. The force ratio in this case was calculated by averaging the force ratio at each arrangement of the sensor. Same rubber

samples having size of 12 x 24 mm were used for measuring the force ratio as used in the common base sensor. The data obtained for each load set are given in Tables A2.21-A2.26 of Appendix II for each sample of the rubber. The data for each sample of the rubber from appendix tables at 3N were selected and represented in Table 5.7. Similarly, the samples are arranged depending upon the hardness of the sample as shown in the Figure 5.5. Softness order was arranged depending upon the order of the force ratio. Results obtained from the different are similar to the single sensor and common base sensor.

Table 5.7 Experimental Results at the 3N of load with different samples of the rubbers, for different base sensor

Experimental Data at Load 3N									
Sample No	mV PVDF 1	mV PVDF 2	mV PVDF 3	mV PVDF 4	N Force 1	N Force 2	N Force 3	N Force 4	Force Ratio
1	2.946	87.78	3.01	97.32	0.513	1.475	0.518	1.489	0.348
2	1.260	109.18	1.428	108.15	0.202	1.691	0.217	1.721	0.127
3	1.645	106	1.936	112.36	0.303	1.686	0.357	1.805	0.189
4	2.281	110.09	2.30	109.00	0.413	1.701	0.421	1.684	0.246
5	1.506	107.06	1.693	105.00	0.262	1.736	0.307	1.622	0.170
6	2.534	113.42	2.686	113.42	0.472	1.653	0.501	1.736	0.287

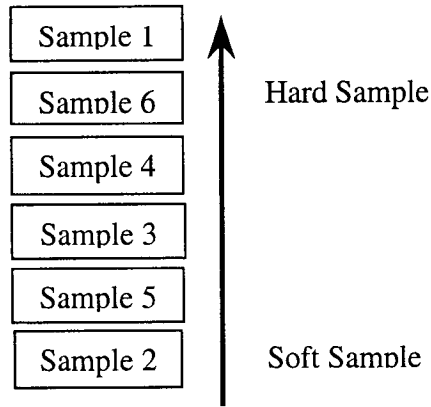


Figure 5.5 Softness of the sample depending on the experimental results, different base

5.5 Comparison of the Experimental Results

Comparisons of the experimental results obtained in the previous section are demonstrated in this section of the chapter. The results obtained from the experimental analysis are compared with the theoretical results. The experimental results are compared amongst the single sensor, common base sensor and different base sensor. In addition the single sensor, common base sensor and different base sensors experimental results are compared with the finite element results of 2D and 3D model. The results are compared and error analysis is made. The deviation of the results from the expected theoretical results is also discussed in each section. The three experimental results are plotted on the same graph as shown in Figure 5.6 for compression. Figure 5.6 shows the experimental results over the range of modulus of the elasticity of 10^4 - 10^6 . The single sensor, common base and different base sensor results are presented in the form of squares, circles and diamonds, respectively.

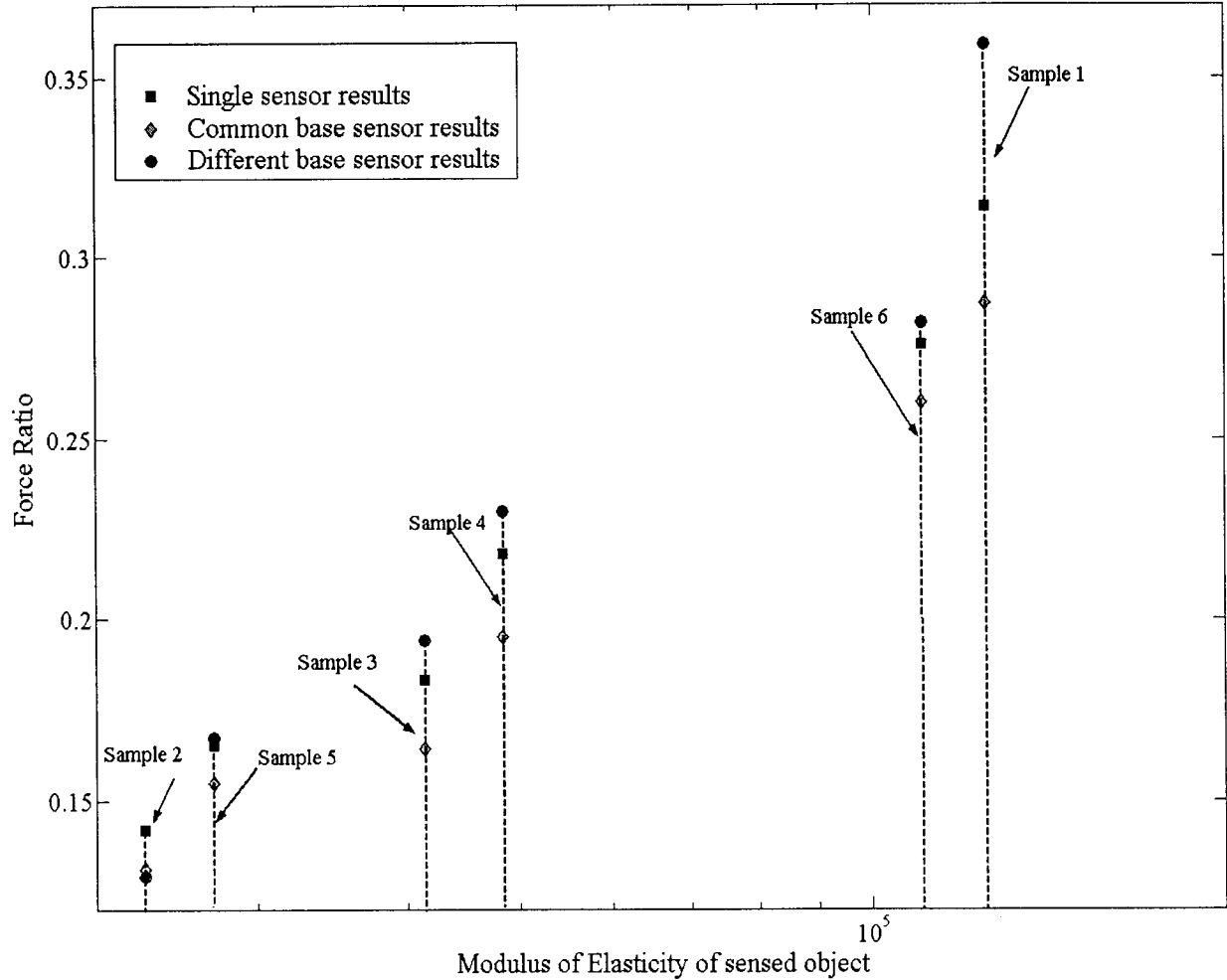


Figure 5.6 Comparison of the experimental results between single sensor, common base and different base sensor.

The single sensor results show the good linearity and parallelism with the theoretical results. By joining single sensor points on the sample 2-3-1 we get parallel line to the theoretical results. This behavior is discussed in the detail in the following section. Similarly, the common base sensor results give good linear and parallel results to expected one. Interestingly, it was noticed that the force ratio calculated by the common base sensor was less than that of the single sensor expect in case of sample 1 and follows the same rise and fall

pattern. It is clear from this variation that more force is carried by the compliant part in common base sensor. Sample 2 is very soft, therefore unexpected behavior was noticed in different base sensor. Sample 2 shows less force ratio. Sample 2 give the very less force ratio in as compared to the common base sensor and single sensor.

5.5.1 Comparison of Experimental and Theoretical Result for Single Sensor

The experimental results of single sensor are compared with the theoretical results of 2D and 3D finite element model of the single sensor. Theoretical results of 2D model and 3D model were obtained from section 4.5.1 of the dissertation. The results obtained at the modulus of elasticity of 2.4×10^4 for compliant cylinder were used. Figure 5.7 shows the experimental and theoretical results for the single sensor. It was noticed that the values of the experimental data lie between the lines of 2D model and 3D model theoretical results. The force ratio represents the order of the samples, but it is very hard to draw line that represents all the values of the experimental data in synchronized form. More focus is required on the experimental data acquisition for more synchronized justification. Error was calculated for each sample with respect to their corresponding theoretical results. Table 5.8 shows the percentage error of the experimental results. The average percentage error with respect to the 2D model is 20.08%. The results are closer to the 3D model with an average error of -9.62%.

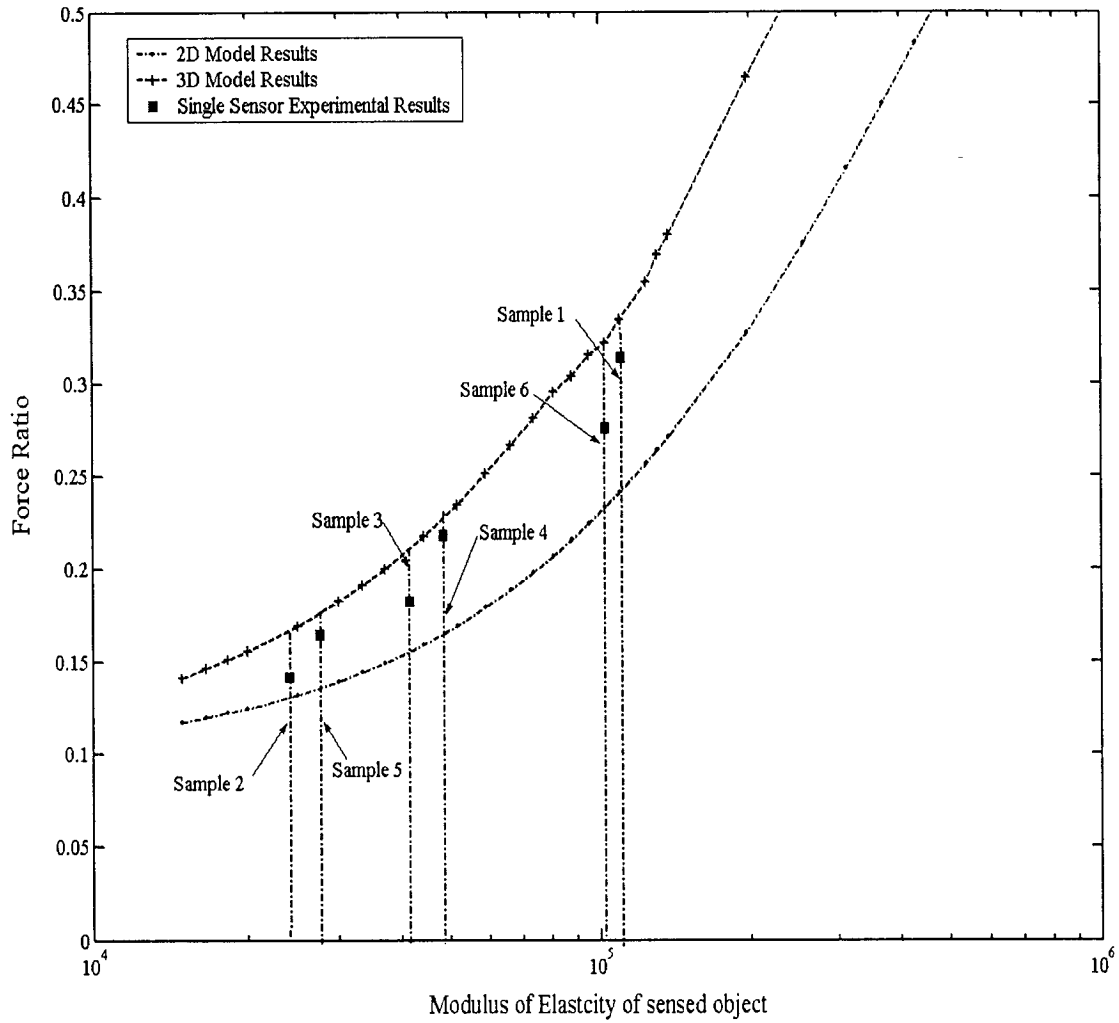


Figure 5.7 Comparison of the experimental results with 2D model and 3D model for single sensor.

5.5.2 Comparison of the Experimental and Theoretical results for Common Base Sensor

The experimental results of the common base sensor was obtained by using different rubber samples and plotted with 3D model of theoretical results of the common base sensor. This is shown in the Figure 5.7. Force ratio results are higher than the 3D model results. This

variation is aligned with all the other data obtained. The results from sample 2-3-6 are close to the theoretical results. Table 5.8 shows the percentage error of the experimental results. Average percentage error was also calculated and was 23.64%.

Table 5.8 Calculated percentage errors in the experimental results

Experimental results compared with	3D Model	2D Model	3D Model	3D Model
Sample No.	Single Sensor		Common base Sensor	Different base Sensor
1	-5.7	30.3	21.56	38.42
2	-15.2	8.33	23.07	22.7
3	-12.93	12.44	21.21	33.8
4	-3.96	31.52	28.2	39.74
5	-7.14	21.05	30.64	37.5
6	-12.8	16.82	17.14	24.2
Average % Error	-9.62	20.08	23.64	32.72

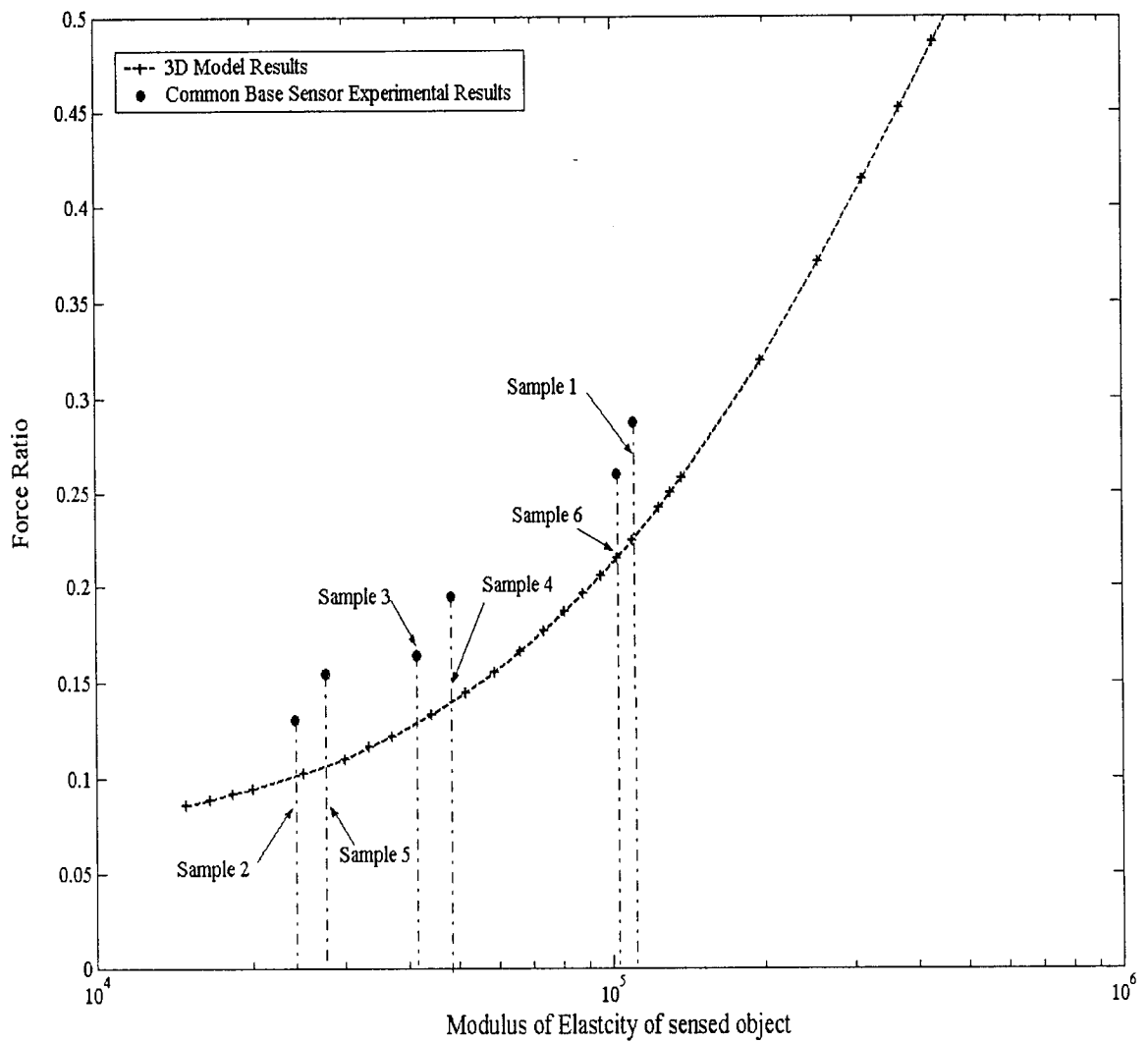


Figure 5.8 Comparison of the experimental results with 3D model for common base sensor

5.5.3 Comparison of the Experimental and Theoretical Results for Different Base Sensor

The experiments results obtained from the different base sensor and 3D finite element model of the sensor are shown in the Figure 5.9. Table 5.8 shows the percentage error of the experimental results. The average percentage error in calculating samples force ratio was found to be 32.72% as compared to the 3D theoretical model results. It is clear from the discussion that single sensor has less percentage error as compared to the common base and different base sensor. The 3D model show more aligned with the experimental results. From all the above discussion, it was concluded that single sensor are aligned with the theoretical results more as compared to the common base and different base sensor. To differentiate the materials based on the softness of the object, single sensor could serve the purpose. The future scope of the study and observation from the results are discussed in the next chapter of the dissertation.

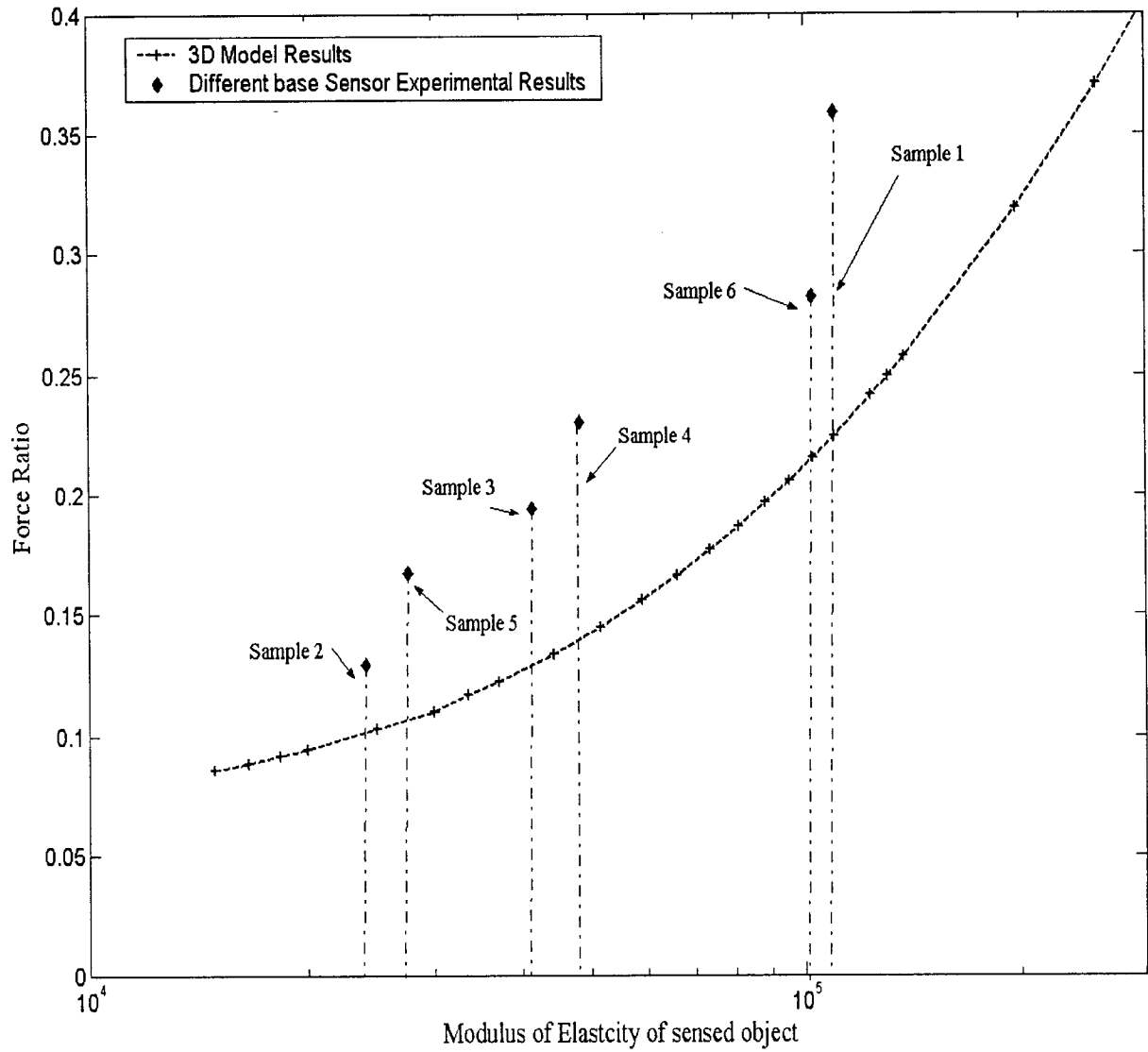


Figure 5.9 Comparison of the experimental results with 3D model for different base sensor

Chapter 6

Conclusions and Recommendations

Piezoelectric force sensors were designed and fabricated for measuring the force and compliance of the tissue using the phenomenon of piezoelectricity and relative deformation. The sensors were designed at considerably bigger size to justify the theory with experimental results. The performance and experimental results of prototype sensors were discussed. The effect of the two sensors mounted on the grasper and the results of the assembled sensor were also taken into consideration. The micromachining concept could be used for making more versatile and smaller size systems. The fabrication of the sensor prototype was not cumbersome and it was simply the joining of the parts together using the nonconductive and conductive glues. This chapter concludes the research work and provides recommendation for the future work.

The prime objective of this research work was to develop the sensor for measuring the force on the endoscopic grasper and simultaneous measurement of the compliance of the tissue. The simulation of the sensor is carried out in the ANSYS. Basic phenomenon of the piezoelectricity is considered for measuring the force on the sensor. The novel method is introduced for the measuring the force and compliance of the tissue. In the dissertation, theoretical and experimental comparison is demonstrated. The main attribution of the present research work is summarized as follows:

- I. The design of the single sensor with dimension of 10 x 10 mm. The sensor is considered as prototype.

- II.** The theoretical approach for measuring the compliance of the tissue is also discussed under the static loading.
- III.** The mounting of the sensor on the grasper is discussed. Two different cases of assembly are presented with experimental justifications. These two arrangements are.
 - a. Two sensors mounted on the common base plates.
 - b. Two sensors mounted on the different base plates.
- IV.** Discussion on the fabrication of the prototype of the sensor using conductive glue and non-conductive glue.
- V.** Experimentation was carried out with the single sensor, common base sensor and different base sensor under dynamic uniform distributed load sets.
- VI.** The 2D model and 3D model are compared using analytical and numerical approach.
- VII.** Dissertation also concludes the discussion on the effect of the uniform distributed load on the sensor assembly.
- VIII.** Comparison of two sensors with different base plates and two sensors with common base plates under uniform distributed load.
- IX.** Comparison of the theoretical results for single sensor and common base sensor.
- X.** Experimental results obtained from single sensor, common base sensor and different base sensor are also compared.
- XI.** Experimental results of sensors are compared with the theoretical results.
- XII.** Percentage errors in the experimentation are also calculated.

6.1 Conclusions

In this section of the chapter, complete conclusion of the dissertation is presented. The comparison of the different arrangements and experimental performance is discussed in the following section:

1. Theoretical justification of the results and the procedure to find the compliance of object. Total uniform static force is applied and uniform over the entire range. The theoretical results showed that it is best for object having modulus of elasticity of sensed object less than 10^7 .
2. Finite element analysis of the 2D and 3D single sensor model also shows good linearity and uniformity in the results. The 2D results are less than 3D model because of the assumption made during the analysis.
3. Experimental results and finite element results for single sensor have established good linear relationship and yields good results with low hysteresis between the modulus of sensed object and force ratio. The percentage error between the results is -9.62% .
4. Experimental results obtained for common base sensor also follow the same pattern of variation as compared to the theoretical results. The percentage error in this case was near 23.64% . This error could be reduced during miniaturization.
5. Experimental results for the different base sensor give an error of 32.72% with linear response.
6. The softness order of materials judge by the single sensor, common base sensor and different base sensor show great similarity with the expected softness order of materials irrespective of the percentage errors.

7. Miniaturization of the sensor could match the theoretical and experimental results more precisely. In the future, sensors could be miniaturized on the endoscopic grasper with help of the micro electro-machining.
8. Proper calibration of the sensor is also required for the accurate data interpretation. Secondly, arrangement should be made in such a way that the load applied is only applied in one direction and PVDF film is free to deform in all direction, without the gluing effect.
9. Theoretical results are obtained under static loading while dynamics analysis where performed on the PVDF sensors. This could be the reason of the deviation of the results.
10. Rubber samples where tested under the dynamic loading, which show higher results as compared to the 3D ANSYS model. Under dynamic effect rubber samples do not undergo complete deformation and act as damper-spring arrangement. This phenomenon is considered as the main cause of the error.
11. We used epoxy glue for assembling of the parts of the sensor. The epoxy glue provides very good strength to the structure and PVDF film. The PVDF film did not undergo the deformation as expected because of this gluing property. In practical application, other alternatives for the glue should be used which have low strength and have good lubrication effect.
12. The more precise dimensions make the results more accurate. The dimension of the sensor should be checked with the fine instruments. Roughness of the plexiglas also effects the PVDF films output. The optimization of the design is required.

13. The sensor is very susceptible to noise, so better insulation is required to shield from the environmental during experiments.
14. Sensor consists of the simply a rigid cylinder and flat plate arrangement so the chances of getting rupture under heavy loading are very less. Only shear force could dislocate the rigid cylinder from its position.

6.2 Recommendation for Future Work

The dissertation only demonstrated the theoretical and experimental justification of the results of prototype sensor. Future work on the sensor design can be extended to different directions and ideas. The prototype of the first generation of the sensor was designed. The theoretical portion and designing aspect of the sensor were considered with experimental validation. The sensor can be manipulated into miniaturized foam. The sizing and micromachining of the sensor is one of the important field in which significant work is required. The provision should be considered to change the tip of the grasper sensors, which is also an important aspect for the future work. The cost of the sensor should be very small so that for each operation the sensor-tip on the grasper can be changed in order to avoid the risk of the infection to the patients. The parametric study is also required for the future optimization of the sensor. Frequency of 10 Hz was used for performing the experimentations. Investigation on the other frequency ranges is also required to optimize the working behaviors of the sensor.

Significant work is also required for amplification of the sensor signal. The signal-to-noise ratio should be reduced for the accurate results. The proper packing and

protection from the environment for the sensor is also required. This protection helps the sensor to work successfully in harsh and destructive environment. The future sensor should be designed like chip. Micromachined devices integrated with the electronics circuits in chip result in high precision capacitance measurement sensors. Some integral electric circuit should be required to measure the static response. The designing of the electronic circuit for measuring the static response and increasing the time constant ($\tau = RC$) for better interpretation of the results are required. To enhance the sensitivity, linearity and ruggedness of the sensor are also important aspects of the performance of the sensor.

The second main aspect of the next generation sensor is to find out the effect of the humidity on the sensor. In actual practice, the sensor will work under the humid conditions inside the body. The leakage of the charge from the PVDF films and wires affects the performance of the sensor. The proper insulation and protection from the humidity should be considered for future application.

Selection of the compliance material for the outer part of the sensor is also very difficult and it requires significant work. The compliance of the outer soft cylinder also changes with the humidity. The tissue was considered as elastic isotropic substance for the analysis. But in actual practice, it behaves like viscoelastic materials. Thus, the viscoelastic modeling is required for good interpolation of the behavior. More research work is required to properly assemble the sensor and appropriate provision should be considered for cleaning and sterilization. The study of temperature variation and compensation is also required for the better performance.

The shear effect is also an important part for tactile sensation. The shear effect can be considered into design in order to detect the roughness and slippage of the tissue from the endoscopic grasper. Detailed study of the relative deformation for the compliant part also requires the understanding of the grasping behavior of the sensor. This relative deformation of the cylinders provides good holding properties. The assembly of the sensors, electronics circuit and fabrication process are the most multifaceted work, which required practical thinking and approach.

BIBLIOGRAPHY

- [1] E. Graves. Vital and Health Statistics. Data from the National Health Survey No. 122. U.S. Department of Health and Human Services, Hyattsville, MD, 1993.
- [2] Voges U. Technology in Laparoscopy - what to expect in the future. Urologe Ausgabe (a) 1996; 35:208 -14.
- [3] Fearing, R.S. and Cohn, M.B., "Tactile feedback for teleoperation." In: Telemanipulator technology, SPIE Proc., Boston, November 1992. pp. 641-6.
- [4] Dario, P., "Tactile Sensor- Technology and Applications." Sensor and Actuators A- Phys. 1991; 26: 251-6.
- [5] Bicchi, Canepa, A., G., Rossi, Lacconi, D. de, P. and Scilingo, Ep., "A Sensorized Minimally Invasive Surgery Tool for Detecting Tissue Elastic Properties." In IEEE Int. Conf. on Robotics and Automation, Minneapolis, MN, 22-28 April 1996. IEEE, Robot and Automation Soc, 1996, pp 884-890.
- [6] Fischer, H., Heilig, R., Trapp, R. and Brhel, K., "Tactile optical sensor for use in minimally invasive surgery." Langen becks Archive Fur Chirurgie 1996; pp-1290.
- [7] Dario, P., Carrozza, M.C., Lenconini, L., Maganani, B. and D'Attanasio, S., "A Micro robotics system for colonoscopy", IEEE Int. Conf. on Robotics and Automation, Albuquerque, New Mexico, April 1997, pp. 1567-72.
- [8] Howe, R.D., Peine, W., Son, J.S. and Kontarinis, A.D., "A tactile shape sensing and display system for teleoperated Manipulation". IEEE Int. Conf. on Robotics and Automation, 1995, pp. 641-646.
- [9] Cohn, M.B., Crawford, L.S., WendLandt, J.M. and Sastry, S.S., "Surgical Application of milli robots." Robotics Systems 1995; 12:6:401-16.

- [10] Umemori, M., Sugawara, J., Kawauchi, M. and Mitani, H., "A pressure-distribution sensor (PDS), for evaluation of lips functions". American. Jour. Of Orthodontics and Dentofacial orthopedics 1996; 109:473-80.
- [11] Gray, B.L., Fearing, R.S., "A surface micromachined microtactile sensor array", Proc. of the IEEE Int. Conf. on Robotics and Automation, Minneapolis, Minnesota, April 1996.
- [12] Mehta, M., "A micro machined capacitative pressure sensor for use in endoscopic surgery", M.Sc. thesis, School of Eng. Science, Simon Fraser University, B.C. Canada, 1996.
- [13] Dargahi, J., Parameswaran and Payandeh, S., "A micro machined piezoelectric tactile sensor for endoscopic grasper: Theory, Fabrication and Experiments," J. of MicroElectroMechanical Systems, 9, No. 3, pp. 329-335, 2000.
- [14] Dario, P., Bergamasco, M. and Sebatini, A., "Sensing body structure by an advanced robotic systems", Proc. IEEE Int. Conf. on Robotics, 1988, 1758-1763.
- [15] Josivaldo, G.S., Carvalho, A.A. and Silva, D.D., "A strain gauge tactile sensor for finger-mounted application", IEEE Trans. on Instrumentation and Measurement, Vol. 51, No. 1, February 2002.
- [16] Shinoda, H. and Ando, S., "A Tactile sensor with 5-D Deformation Sensing Element", IEEE Int. Conf. on Robotics and Automation, Minneapolis Minnesota –April 1996.
- [17] Dargahi, J., "A Piezoelectric tactile sensor with three sensing elements for robotics endoscope and prosthetic application", Sensor and Actuators, Vol. 80, 2000, pp. 23-30.

- [18] Ohka, M., Mitsuya, Y. and Kamekawa, O., "A three axis optical tactile sensor (FEM contact Analysis and sensing experimental Using a large-sized Tactile sensor)", IEEE Int. Conf. on Robotics and Automation, Vol. 6, 1995, pp. 817-824.
- [19] Obana, F.Y., Carvalho, A.A., Gualda, R. and Silva, G.J., "A semiconductor strain gage tactile Transducer", IEEE Instrumentation and Measurement Technology Conf. Budapest, Hungary, May 21-23, 2001, pp 429-432.
- [20] Shimizu, T., Shikida, M., Sato and Itoigawa, K., "A new type of tactile sensor detecting contact force and hardness of an object." IEEE, Int. Conf. on Robotics and Automation, 2002, pp. 344-347.
- [21] Payandeh, S., Faraz, A. and Salvarinov, A., "Design of haptic interface through stiffness modulation for endosurgery: Theory and Experiments", IEEE, Int. Conf on Robotics and Automation, May 1998, pp. 1007-1012.
- [22] Hutter, R., Rhomberg, A., Schmid, P., Brechbuhler, C. and Szekely, G., "Modelling of Soft Tissue Deformation for Laparoscopic Surgery Simulation", Biomechanics, V.1496, 1998, pp- 550.
- [23] Chen, J.E., Novakofski, J., Jenkins, K.W. and O'Brein, Jr. D.W., "Young's modulus measurements of soft tissues with application to elasticity imaging", IEEE Trans. on Ultrasonics, Ferroelectrics and Frequency Control, Vol. 43, No.1, January-1996, pp. 191-194.
- [24] Skovoroda, A.R., Lubinski, A.M. and Emelianov, Y.S., "Reconstructive elasticity imaging for large deformations", IEEE Trans. on Ultrasonics, Ferroelectrics and Frequency Control, Vol. 46, No. 3, May-1996, pp. 523-535.

- [25] Sumi, C., Suzuki, A. and Nakayama, K., "Estimation of shear modulus distribution in soft tissue from strain distribution", IEEE Trans on Biomedical Engineering, Vol. 42, No. 2, February 1995, pp. 193-202.
- [26] Brouwer, I., Ustin, J., Bentley, L., Sherman, A., Dhruv, N. and Tendick, F., "Measuring in vivo animal soft tissue properties for haptic modeling in surgical simulation", Medicine Meets Virtual Reality 2001, J.D. West Wood et al. (Eds), IOS Press, 2001.
- [27] Ottensmeyer, M.P. and Salisbury, Jr. K.J., "In vivo data acquisition instrument for solid organ mechanical properties measurement", W. Niessen and M. Viergever (Eds.): MICCAI 2001, LNCS 2208, pp. 975-982, 2001.
- [28] Chail, V.B., Greenish, S. and Okamura, A.M., "On the display of haptic recording for cutting biological tissues", IEEE, Int. Conf. on Virtual Reality, Orlando FL, March 24-25, 2002.
- [29] Rosen, J., Hannaford, B. and Sinanan, N.M., "Markov modeling of minimally invasive surgery based on tool/tissue interaction and force/torque signature for evaluating surgical skills", IEEE Trans. on Biomedical Engineering Vol., 48, No. 5, May 2001, pp. 579-591.
- [30] Rosen, J., Hannaford, B. and Sinanan, N.M., "Force controlled and teleoperated endoscopic grasper for minimally invasive surgery- Experimental performance evaluation", IEEE Trans. on Biomedical Engineering Vol., 46, No. 10, October 1999, pp. 1212-1221.
- [31] J. Webster, "Mechanical variables measurement", edited by Webster, London 2000.

- [32] L.R., "Sensor Technologies and Microsensor issues for Mechatronics systems", IEEE/ASME Transaction on Mechatronics, 1996, vol. 1, issue 1, p. 39-49.
- [33] Harmon, L.L., "A high resolution imaging tactile sensor", Int. J. Robotics Res. 1982, vol. 1, p. 33.
- [34] J. Webster, "Tactile sensors for robotics and medicine", New York, Wiley, 1988.
- [35] Tse, F.S. and Morse, E.I., "Measurement and instrumentation in engineering", Marcel Dekker Inc, New York, 1989.
- [36] Fearing, R.S., "Tactile sensing mechanism", Int. J. Robotics Res., vol. 9, issue 3, p. 3-24
- [37] Jensen, T.R., Radwin, R.G. and Webster, J.G., "A conductive polymer sensor for measuring external forces", J. Biomechanics, vol. 24, p. 851-858, September 1991.
- [38] Emge, S.M. and Chen, C.L., "Two dimensional contour imaging with fiber optic microbend tactile sensor array", Sensor and Actuator, B, 1991, vol. 3, p.31-42.
- [39] Maalej, N., and Webster, J., "A miniature electrooptical force transducer", IEEE transaction on biomedical Engineering, 1988, vol. 35, issue 2, p. 93-98.
- [40] Suzuki, I., Kikuta, H., Iwata, K. and Kato, N., "Force balancing microforce sensor with an optical fiber interferometer", Review of Scientific Instruments, Vol. 68, No. 6, June 1997.
- [41] Runyan, W.R. , "Silicon semiconductor technology", New York, McGraw-Hill, [1965].
- [42] Beebe, J.D., Hsieh, A.S., Denton, D.D. and Radwin, R.G., "A silicon force sensor for robotics and medicine", Sensor and Actuators, vol.2, p.711-716, 1994.

- [43] Da Silva, J.G., Carvalho, A.A. and Silva, D.D., "A strain gage tactile sensor for finger-mounted Applications", IEEE Trans. on Instrumentation and measurement, vol. 51, p. 824-829, February 2000.
- [44] Donald, L.W., "Bioinstrumentation: Research, Developments and Applications", 1990.
- [45] Dargahi, J., "Piezoelectric and pyroelectric transient signal analysis for detection of the temperature of a contact object for robotic tactile sensing", Sensor and Actuator A, April 1998.
- [46] Harsanyi, G., "Sensor in Biomedical Applications", Technomics, New Holland, Pennsylvania, 2000.
- [47] Ferris, C.D., "Introduction to Bioinstrumentation", Clifton N. Jersey, 1978.
- [48] Bathe, K.J., "Finite Element Procedures", Prentice-Hall, 1996.
- [49] George, G., "The design and fabrication of micromachined capacitive micro sensors for pressure measurement and tactile imaging", Thesis (MA.Sc.), Dept. of Mechanical Engineering, Concordia University, 1995.
- [50] Chowdhury, S., "Design synthesis and testing of a capacitive type pressure transducer using micro-machining techniques", Thesis (MA.Sc.) -- Dept. of Mechanical Engineering, Concordia University, 1993.
- [51] Desai, C.S., "Elementary finite element method", Englewood Cliffs, N.J.: Prentice-Hall, c1979.
- [52] Cady, W.G., "Piezoelectricity," 1st ed., McGraw-Hill Inc., New York, 1946.
- [53] Toupin, R.A., "A Dynamical theory of elastic dielectrics," International Journal of Engineering Science, Vol. 1, 1963, pp. 101-126.

- [54] Toupin, R.A., "The Elastic dielectric," Journal of Rational Mechanical Analysis, Vol. 5, No. 6, June 1956, pp. 849-915.
- [55] Tiersten, H.F., "Coupled magneto mechanical equations for saturated insulators," Journal of Mathematical Physics, Vol. 5, No. 9, 1964, pp. 1298-1318.
- [56] Allik, H. and Hughes, T.J.R., "Finite element method for piezoelectric vibration," International Journal for Numerical Methods in Engineering, Vol. 2, 1970, pp. 151-157.
- [57] Peelamedu S, Naganathan G, Barnett A, Rao D 1999 Finite element approach to model and analyze piezoelectric actuators American Institute of Aeronautics and Astronautics (AIAA) Journal Communicated on Feb 1999.
- [58] Peelamedu S, Niemeyer S, Naganathan G, Rao D 1999 Piezoceramic array actuator system for deformable mirror applications Journal of Smart Materials and Structures Communicated on Dec 1999.
- [59] Fung, Y.C., "Biomechanics: mechanical properties of living tissues", New York: Springer-Verlag, 1993.
- [60] Reddy , J.N., Krishnamoorthy, C.S., Seetharamu, K.N., "Finite element analysis for engineering design" Berlin ; New York : Springer-Verlag, c1988
- [61] Zeus Robotics Systems website "http://trueforce.com/Medical_Robotics/zeus.html"
- [62] Materials properties "www.matweb.com"

APPENDIX - I

Piezoelectric Effect

When external force is applied to piezoelectric materials it generates charge on the surface, which is proportional to applied mechanical stress. The converse effect is also true, applied voltage generates deformation in the materials. Piezoelectricity relates to the crystalline ionic structure.

A simplified model of piezoelectricity entails the motion of anions (-) and cations (+) moving opposite directions under the influence of an electric field and mechanical force. The force generated by this motion cause lattice deformation. for non-centrosymmetric crystals due to presence of both high and low stiffness ionic bonds. As a result, all piezoelectric materials are anisotropic, in case of central symmetry, an applied force does not yield an electric polarization. The effect for quartz is shown below in Figure A1.1, positive and negative charges are formed. It is important to remember that the piezoelectric materials are function of the continuously changing mechanical deformation. Therefore dynamic forces are used in practical situations.

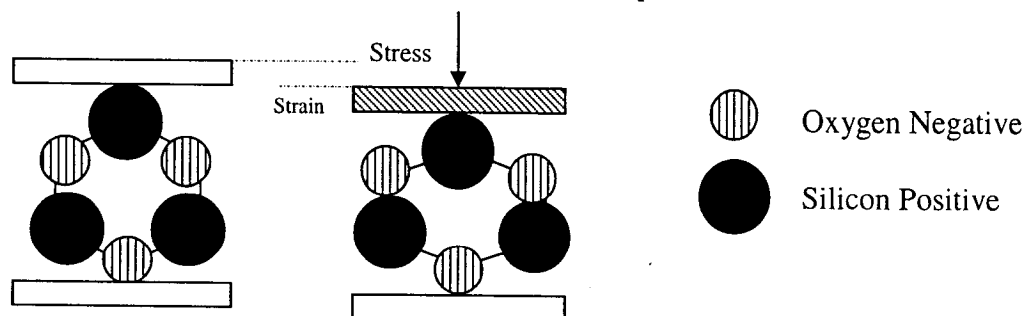


Figure A1.1 Piezoelectric in ionic crystals such as quartz, ion position in quartz lattice with and without applied stress.

A1.1 Piezoelectric Materials

The most extensively used natural piezoelectric materials are crystals (quartz and tourmaline). In synthetic piezoelectric, ceramics formed by many tightly compacted monocrystals (1μ in size) are most popular. These Ceramics, such as Lead Zirconate titanate (PZT), barium titanate is piezoelectric electrics. To align the dipoles to monocrystals in same direction, they subjected to strong electric field during their manufacturing process. We applied electric field to crystal above the Curie temperature to align the dipoles. Then cool the crystal while maintaining the field. This process makes crystal permanent electric polarized. When electric field is removed, the crystalline cannot reorder in random from because of mechanical stresses accumulated, resulting in permanent electric polarization. The problem with these materials relates to their temperature sensitivity and aging when approaching the Curie temperature.

Polymers such as polyvinylidene-fluoride(PVDF), also display piezoelectric properties and have pyroelectric features, i.e. changes the electrical charge with change in temperature. PVDF are not central symmetry i.e. it display piezoelectric properties. Compared to quartz and ceramics, piezo-film is more pliant and lighter in weight. In addition to this it is rugged, inert and low cost. Secondly urethane and epoxy adhesive are used for gluing PVDF. The use of epoxy and urethane adhesives depends upon the strength requirement of the structure.

In smart structures, piezo ceramics are typically used as actuators, polymeric piezoelectric materials are typically tactile sensor, temperature and strain sensors. It is common practice to embed piezoelectric sensors into prototypes because these sensors can be manufactured with strength and dimensional characteristics that do not degrade

the structural integrity of the material from which the prototype device is made. Piezoelectric ultrasonic motors and piezoceramic sensors are currently being built into commercial products such as camera lens drives and automotive engine control systems. In many cases, thin layers of piezoceramic composites are bonded to other structural material surfaces. When thermal effects are generated through either friction or direct exposure to significant temperature gradients, the reliability of the electrode layer in these piezoceramics can completely dominate the performance of the device.

Many efforts have been done for mathematical modeling of piezoelectric phenomenon. The researcher efforts in piezoelectricity carried out in the past produced in our work. Cady [52], (1946) gave comprehensive description of development in the theory of piezoelectricity. Toupin [53-54], (1956, 1963) involved in development of the governing equation using energy methods and dynamics theory. Tiersten [55], (1969) made several approximations and developed linear equation of piezoelectricity using Hamiltonian mechanics and variation techniques. Allik and Hughes [56], (1970) developed the general equation of motion for piezoelectric materials in a matrix form. S. Peelamedu [57-58], combined the work together to formulate finite element solution for piezoelectric structure. This section of work includes the concept of Tiersten, Yang (1986), Allik and Hughes (1970). Basic Constitutive Equations (Tiersten, 1969) are expressed in matrix notation as

$$\begin{aligned} [T] &= [c]\{S\} - [e]^T\{E\} \\ [D] &= [e]\{S\} + [\varepsilon]\{E\} \end{aligned} \tag{A1.1}$$

The first and second equation represents structural and electrical model of piezoelectric material, respectively. Where as the entire matrix are given as

$\{T\}$ = Stress vector (N/m²)

$\{D\}$ = Electric flux density (C/m²)

$\{E\}$ = Electric Field Vector (V/m)

$\{S\}$ = Strain vector (dimensionless)

$[c]$ = Elasticity Matrix (N/m²)

$[e]$ = Piezoelectric matrix at constant stress (C/m²)

$[\epsilon]$ = Dielectric Matrix

A1.2 Finite Element Model of a Piezoelectric Element

The numerical formulation worked out by the different researchers for the piezoelectric elements is included in this section. This section provides the information on the finite element formulation of the mathematical model for piezo element, referred to the Peelamedu [57-58]. The six-degree of freedom per element was considered. Three degree of freedoms is for structural deformation and three for electrical deformation, respectively. The strains matrix is given as

$$\{S\} = \begin{Bmatrix} \epsilon_x \\ \epsilon_y \\ \epsilon_z \\ \gamma_{yz} \\ \gamma_{xz} \\ \gamma_{xy} \end{Bmatrix} = \begin{Bmatrix} \frac{\partial u}{\partial x} \\ \frac{\partial v}{\partial y} \\ \frac{\partial w}{\partial z} \\ \frac{\partial v}{\partial z} + \frac{\partial w}{\partial y} \\ \frac{\partial u}{\partial z} + \frac{\partial w}{\partial x} \\ \frac{\partial u}{\partial y} + \frac{\partial v}{\partial x} \end{Bmatrix} \quad (A1.2)$$

Where as u , v , w , represents the displacement of material in X , Y and Z directions, respectively. If n is number of nodes of element and u_i , v_i , w_i are nodal displacements then displacement of element is given as

$$u = \sum_{i=1}^n N_i u_i, \quad v = \sum_{i=1}^n N_i v_i, \quad w = \sum_{i=1}^n N_i w_i \quad (A1.3)$$

Substituting the value of u , v , w in Equation (2), we get

$$\{S\} = \left\{ \begin{array}{c} \frac{\partial \sum_{i=1}^n N_i u_i}{\partial x} \\ \frac{\partial \sum_{i=1}^n N_i v_i}{\partial y} \\ \frac{\partial \sum_{i=1}^n N_i w_i}{\partial z} \\ \frac{\partial \sum_{i=1}^n N_i v_i}{\partial z} + \frac{\partial \sum_{i=1}^n N_i w_i}{\partial y} \\ \frac{\partial \sum_{i=1}^n N_i u_i}{\partial z} + \frac{\partial \sum_{i=1}^n N_i w_i}{\partial y} \\ \frac{\partial \sum_{i=1}^n N_i u_i}{\partial y} + \frac{\partial \sum_{i=1}^n N_i v_i}{\partial x} \end{array} \right\} \quad (A1.4)$$

The above equation can be expressed as

$$\{S\} = [B_u] \{U\} \quad (A1.5)$$

Where $\{U\}$ are element vector displacement and $[B_u]$ Strains-nodal displacement matrix,

$$\text{it is given as } [B_u] = \begin{bmatrix} [N_x] & 0 & 0 \\ 0 & [N_y] & 0 \\ 0 & 0 & [N_z] \\ 0 & [N_z] & [N_y] \\ [N_z] & 0 & [N_x] \\ [N_y] & [N_x] & 0 \end{bmatrix}, \quad \{U\} = \begin{Bmatrix} u_i \\ v_i \\ w_i \end{Bmatrix} \quad (A1.6)$$

Where as $[N_x]$, $[N_y]$ and $[N_z]$ are the matrices, which contain the derivatives of the shape functions for each node of an element with respect to x , y and z respectively. The above analysis is regarding the structural deformation. Similarly, Piezoelectric element we can deduce the electrical finite element equation by using the electric field vector $\{E\}$, - potential function is given as

$$\{E\} = \begin{Bmatrix} E_x \\ E_y \\ E_z \end{Bmatrix} = - \begin{Bmatrix} \frac{\partial \phi}{\partial x} \\ \frac{\partial \phi}{\partial y} \\ \frac{\partial \phi}{\partial z} \end{Bmatrix} \quad (A1.7)$$

Where as, ϕ nodal potential, the finite element approximation is a function of nodal potentials ϕ and nodal shape functions N_i of an element

$$\phi = \sum_{i=1}^n N_i \phi_i \quad (A1.8)$$

Using above approximation in equation (A1.7), we get

$$\{E\} = - \begin{Bmatrix} \frac{\partial \sum_{i=1}^n N_i \phi_i}{\partial x} \\ \frac{\partial \sum_{i=1}^n N_i \phi_i}{\partial y} \\ \frac{\partial \sum_{i=1}^n N_i \phi_i}{\partial z} \end{Bmatrix} \quad (A1.9)$$

Similarly, converting the equations in to simplified matrix notation for electrical analysis

$$\{E\} = - [B_e] \{ \phi \} \quad (A1.10)$$

Where as $[B_e]$ is matrix of derivative of shape function for the potentials

$$[B_e] = \begin{bmatrix} [N_x] \\ [N_y] \\ [N_z] \end{bmatrix}$$

By using the virtual work principle and equating work done by mechanical forces and external electrical charges, it was concluded as

$$\int_V \{\delta S\}^T \{T\} dV = \{\delta u\}^T \{F\} \quad (A1.11)$$

$$- \int_V \{\delta E\}^T \{D\} dV = \{\delta u\}^T \{Q\} \quad (A1.12)$$

By substituting equation (A1.5) and (A1.10) in equation (A1.1), we get

$$\begin{aligned} \{T\} &= [c][B_u]\{u\} + [e]^T [B_e]\{\phi\} \\ \{D\} &= [e][B_u]\{u\} + [\epsilon][B_e]\{\phi\} \end{aligned} \quad (A1.13)$$

Also,

$$\{\delta S\}^T = \{\delta u\}^T [B_u]^T \quad (A1.14)$$

$$\{\delta E\}^T = - \{\delta \phi\}^T [B_e]^T \quad (A1.15)$$

From equation A1.11, A1.12, A1.13, A1.15 and rearranging, we get

$$\begin{aligned} \{\delta u\}^T \int_V [[B_u]^T [c][B_u]\{u\} + [B_u]^T [e]^T [B_e]\{\phi\}] dV &= \{\delta u\}^T \{F\} \\ \{\delta \phi\}^T \int_V [[B_e]^T [e][B_u]\{u\} - [B_e]^T [\epsilon][B_e]\{\phi\}] dV &= \{\delta \phi\}^T \{Q\} \end{aligned} \quad (A1.16)$$

By simplifying the above equation, the elemental finite element equations are given as

$$\begin{bmatrix} K_{uu} & K_{ue} \\ K_{eu} & K_{ee} \end{bmatrix} \begin{Bmatrix} u \\ \phi \end{Bmatrix} = \begin{Bmatrix} \{F\} \\ \{Q\} \end{Bmatrix} \quad (A1.17)$$

Where as,

$$[K_{uu}] = \text{Structural Matrix} = \int_V [B_u]^T [c] [B_u] dV$$

$$[K_{eu}] = [K_{ue}]^T = \text{Piezoelectric stiffness Matrix} = \int_V [B_u]^T [e]^T [B_e] dV$$

$$[K_{ee}] = \text{Dielectric stiffness Matrix} = - \int_V [B_e]^T [\epsilon] [B_e] dV$$

The elemental finite element equation for piezoelectric material is given by equation (A1.17). Above equations could be used for global meshing. Using the appropriate stiffness matrices, the global stiffness matrix corresponding to a finite element model of a three-dimensional piezoelectric structure generated using the number of solution methodologies can be invoked to solve the resulting system of finite element equations. For the solution of the system of finite element equations assembled, it would seem that a Gaussian Elimination procedure could be used. After the global stiffness matrix and global force vector were assembled, the vector of unknown displacements and potentials would be directly solved for. However, typical elements of $[K_{uu}]$ are of the order of 10^8 , while typical values in $[K_{ee}]$ are of the order of 10^{-11} . Because of this great difference in magnitudes, the global stiffness matrix is too ill conditioned for this method. Although the two sub-matrices are diagonally dominant when considered separately, when taken as a whole, the difference in magnitudes creates problems. The general method of static condensation leads itself well to the solution of piezoelectric element equations. A static condensation procedure sacrifices the accuracy of the solution for one set of unknowns for the improved accuracy of the solution for a second set. Before start working on the piezoelectric material, it became necessary to know more about the piezo-coefficients and values used. Piezoelectric coefficients are discussed in the next section.

A1.3 Piezoelectric Coefficients

Most of piezoelectric coefficients have double subscript that links electrical and mechanical quantities. The first subscript gives the direction of the electrical field associated with voltage applied and second subscript gives the direction of the mechanical stress or strain.

A1.3.1 d - Coefficients

The piezoelectric constant relating the mechanical strain produced by an applied electric field are termed the strain constant or 'd' coefficients or piezoelectric strain matrix. Conversely the coefficient may be viewed as relating the charge collected on the electrodes, to the applied mechanical stress. The unit of 'd' coefficient is C/N.

$$d = \text{charge density} / \text{applied mechanical stress}.$$

A1.3.2 g Coefficients

The piezoelectric constants relating the electric field produced by a mechanical stress are termed the voltage constants, or the "g" coefficients. The units are then expressed as volts/meter per Newton/square meter.

$$g = \frac{\text{ElectricField}}{\text{Applied Mechanical Stress}} \quad (\text{A1.18})$$

High g_{ij} constants favor large voltage output, and are sought after for sensors. The relationship between the [d] and [g] matrix is given as

$$[d] = \epsilon[K]^T[g] \quad (\text{A1.19})$$

A1.3.4 Dielectric Constants

The relative dielectric constant is ratio of the permittivity of material, ϵ , to the permittivity of free space, ϵ_o , in the unconstrained condition. ($\epsilon_o = 8.9 \times 10^{-12}$ Farad/meter).

$$K = \frac{\text{Permittivity of material}}{\text{Permittivity of free space}} = \frac{\epsilon}{\epsilon_o} \quad (\text{A1.20})$$

A1.3.5 Capacitance

Capacitance is a quantity dependent on the type of materials and its dimensions. Unit of capacitance is Farad. Capacitance is expressed by following formula

$$C = \frac{K\epsilon_o A}{t} \quad (\text{A1.21})$$

where as 'A' area of electrodes, 't' is gap between the electrodes.

A1.3.6 Young's Modulus

Young's Modulus is ratio of stress (force per unit area) to strain (change in length per unit length). Unit of young Modulus is N/m^2 .

$$Y = \frac{\text{Stress}}{\text{Strain}} \quad (\text{A1.22})$$

A1.3.8 Curie Temperature

The Temperature at which the crystal structure changes from a non-symmetrical (piezoelectric) to a symmetrical (non- piezoelectric) form, expresses in degrees Celsius.

A1.4 Analytical Approach

In addition to our knowledge we must also know analytical approach for simple cases. The analytical method is demonstrated in this section. In this section relation between the voltage generation and force applied are discussed. The force F is applied to the rectangular piezoelectric plate of size $L \times T \times W$. The Figure A1.2 demonstrates the working of the rectangular piezoelectric plate. The voltage and charge develop by this force is given as

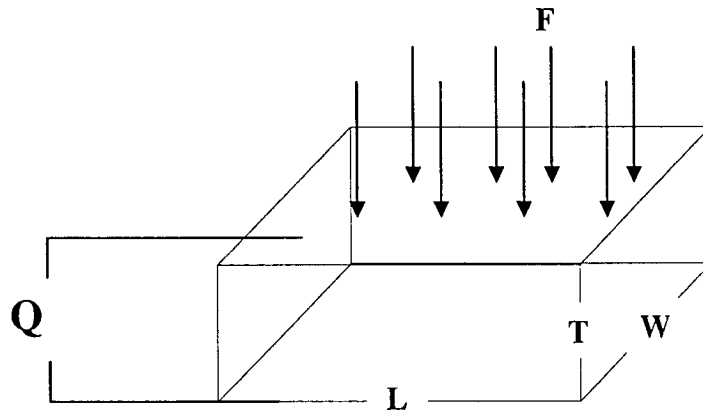


Figure A1.2 Voltage generation by the piezoelectric substance

The sensitivity of uniaxially orientated PVDF film is dependent on the direction of measurement, i.e., drawn, transverse or thickness. When a tensile force is applied in the drawn direction the output charge is expressed by:

$$Q/A_1 = d_{31} F/A_2 = d_{31} \sigma_1$$

Similarly the output charge in the transverse direction (2-2) is expressed by:

$$Q/A_1 = d_{32} F/A_2 = d_{32} \sigma_2$$

where Q = output charge, A_1 = electrode area of the PVDF film, A_2 = cross sectional area of the film perpendicular to the direction of the applied force, d_{31} = piezoelectric strain coefficient in the drawn direction, d_{32} = piezoelectric strain coefficient in the transverse direction, F = applied force, σ_1 = applied tensile stress in the drawn direction and σ_2 = applied tensile stress in the transverse direction, when a PVDF film is compressed by a probe on a rigid flat surface, assuming that both the flat surface and the probe are friction free, the film is free to expand laterally, i.e., in the 1-1 and 2-2 directions. The output charge can thus be given as:

$$Q = d_{33} F$$

where d_{33} is the piezoelectric strain coefficient in the 3-3 direction.

A1.4.1 Properties of different Piezoelectric Materials

Properties of the different piezo electric ceramics and polymers are given in this section. The ceramics are harder as compared to the polymers. Therefore gives small voltage generation response to the same deformation. The main ceramics are PZT-5, PZT-4 and from polymer PVDF film.

PVDF Film Polyvinylidene-fluoride

Compliance matrix $= [s] =$

$$\begin{bmatrix} 0.0820 & -0.0265 & -0.0350 & 0 & 0 & 0 \\ -0.0265 & 0.0820 & -0.0350 & 0 & 0 & 0 \\ -0.0350 & -0.0350 & 0.0945 & 0 & 0 & 0 \\ 0 & 0 & 0 & 0.0215 & 0 & 0 \\ 0 & 0 & 0 & 0 & 0.2250 & 0 \\ 0 & 0 & 0 & 0 & 0 & 0.2250 \end{bmatrix} \times 10^{-8} m^2/N$$

$$\text{Piezoelectric Matrix} = [d] = \begin{bmatrix} 0 & 0 & 0.1900 \\ 0 & 0 & 0.0200 \\ 0 & 0 & -0.1800 \\ 0 & 0 & 0 \\ 0 & -0.0650 & 0 \\ -0.0650 & 0 & 0 \end{bmatrix} \times 10^{-10} \frac{C}{N}$$

$$\text{Dielectric Matrix} = [\epsilon] = \begin{bmatrix} 0.7434 & 0 & 0 \\ 0 & 0.7434 & 0 \\ 0 & 0 & 0.7434 \end{bmatrix} \times 10^{-10}$$

APPENDIX – II

Program of Simulation and Data Obtained

A2.1 Program of Simulation

```
clear all
format long
syms L X E I Kf w Kf1 L1 L2 Kf2 Kf3 L3 P E1 LAMB lambda area
clc
syms A M Aa Ab E1 E2 T1 T2 F1 F2
A1 = pi*(1.4e-3)^2;
T1 = (0.55e-3);
T2 = 3.88E-3;
A2 = 71.47E-6;
E2 = 2.4E4;
N = 1/L^3 * [ (2*X^3 - 3*X^2*L + L^3) (X^3*L - 2*X^2*L^2 + X*L^3) (-2*X^3 + 3*X^2*L) (X^3*L - X^2*L^2) ] ;
M = 1/L^3 * [(2*X^3 - 3*X^2*L + L^3); (X^3 *L - 2*X^2*L^2 + X*L^3);(-2*X^3 + 3*X^2*L); (X^3*L - X^2*L^2) ] ;
B = diff(N,2);
C = [1/L^3*(12*X-6*L); 1/L^3*(6*X*L-4*L^2); 1/L^3*(-12*X+6*L); 1/L^3*(6*X*L-2*L^2)];
P = 1;
Fo = -int(M,0,L)*P;
first_term= E*I*C*B;
second_term = Kf*M*N;
K1 = int(first_term,0,L)
K2 = int(second_term,0,L)
%Element first
Kf1= A1*E1/T1;
U1 = subs(K1,{E,L},{E1,1.4E-3});
U2 = subs(K2,{Kf,L},{Kf1,1.4E-3});
U1(5:6,1:6) = 0;
```

```

U2(5:6,1:6) = 0;
I = 1/12*(5e-3)*(T1)^3;
%Element Second
Kf2= 1/(1/(A2*E1/T1)+1/(A2*E2/T2));
v1 = subs(K1,{E,L},{E1,3.5E-3});
v2 = subs(K2,{Kf,L},{Kf2,3.5E-3});
V1 = [zeros(2,6);zeros(4,2) v1];
V2 = [zeros(2,6);zeros(4,2) v2];
U = U1+V1;
V = U2+V2;
K = U+V
%*clear mod result
L1 = 1.4E-3;
L2 =3.5E-3;
F1 = subs(Fo,{L},{L1});
F2 = subs(Fo,{L},{L2});
F1(5:6,1) = 0
F2 = [ zeros(2,1);F2]
F = F1 + F2
i=0;
for E1= 1.49e4:1e5:1.49e6
i=i+1;
K = subs(K);
disp = inv(K)*F
FORCE1= subs(Kf1)*[disp(1,1)];
FORCE2 = subs(Kf2)*[disp(5,1)];
R(i) = FORCE1/(FORCE2 + FORCE1)
mod(i) =E1
end
plot(mod,R)

```

A2.2 Data Obtained From the Ansys

The data obtained from the ansys and experimental results are presented in this section of the dissertation in table format.

Table A2.1 Voltage generation and force distribution on the rigid cylinder of single sensor at the compliance of cylinder 2.4×10^4

Sensed object Modulus (N/m ²)	Voltage (V)		Force at Rigid Cylinder (N)	Total Force (N)
	PVDF-2	PVDF-1		
1.49e4	-0.142e-3	-0.616e-4	-0.1417	-1
1.66e4	-0.146e-3	-0.616e-4	-0.1465	-1
1.83e4	-0.151e-3	-0.616e-4	-0.1513	-1
2e4	-0.156e-3	-0.616e-4	-0.1560	-1
2.5e4	-0.169e-3	-0.616e-4	-0.1695	-1
3e4	-0.182e-3	-0.616e-4	-0.1825	-1
3.35e4	-0.191e-3	-0.616e-4	-0.1914	-1
3.7e4	-0.200e-3	-0.616e-4	-0.2001	-1
4.43e4	-0.218e-3	-0.616e-4	-0.2177	-1
5.16e4	-0.234e-3	-0.616e-4	-0.2346	-1
5.89e4	-0.250e-3	-0.616e-4	-0.2507	-1
6.62e4	-0.266e-3	-0.616e-4	-0.2661	-1
7.35e4	-0.281e-3	-0.616e-4	-0.2810	-1
8.08e4	-0.295e-3	-0.616e-4	-0.2952	-1
8.81e4	-0.309e-3	-0.616e-4	-0.3052	-1
9.54e4	-0.322e-3	-0.616e-4	-0.3089	-1
10.27e4	-0.334e-3	-0.616e-4	-0.3221	-1
1.1e5	-0.347e-3	-0.616e-4	-0.3347	-1
1.24e5	-0.369e-3	-0.616e-4	-0.3470	-1
1.31e5	-0.379e-3	-0.616e-4	-0.3691	-1
1.38e5	-0.389e-3	-0.616e-4	-0.3797	-1
1.97e5	-0.464e-3	-0.616e-4	-0.4642	-1
2.56e5	-0.522e-3	-0.616e-4	-0.5223	-1
3.13e5	-0.567e-3	-0.616e-4	-0.5676	-1
3.7e5	-0.604e-3	-0.616e-4	-0.6051	-1
4.3e5	-0.637e-3	-0.616e-4	-0.6381	-1
4.9e5	-0.665e-3	-0.616e-4	-0.6660	-1
6.1e5	-0.710e-3	-0.616e-4	-0.7107	-1
7.2e5	-0.741e-3	-0.616e-4	-0.7422	-1
8.46e5	-0.770e-3	-0.616e-4	-0.7709	-1
9.64e5	-0.792e-3	-0.616e-4	-0.7925	-1

1.08e6	-0.809e-3	-0.616e-4	-0.8101	-1
1.2e6	-0.824e-3	-0.616e-4	-0.8254	-1
1.3e6	-0.835e-3	-0.616e-4	-0.8364	-1
1.4e6	-0.845e-3	-0.616e-4	-0.8461	-1
1.7e6	-0.868e-3	-0.616e-4	-0.8693	-1
2e6	-0.885e-3	-0.616e-4	-0.8864	-1
2.5e6	-0.906e-3	-0.616e-4	-0.9068	-1
3e6	-0.920e-3	-0.616e-4	-0.9210	-1
3.5e6	-0.930e-3	-0.616e-4	-0.9314	-1
4.5e6	-0.945e-3	-0.616e-4	-0.9457	-1
5.5e6	-0.954e-3	-0.616e-4	-0.9543	-1
7.5e6	-0.965e-3	-0.616e-4	-0.9657	-1
9.5e6	-0.972e-3	-0.616e-4	-0.9724	-1
14e6	-0.981e-3	-0.616e-4	-0.9810	-1
70e6	-0.995e-3	-0.616e-4	-0.9963	-1
140e6	-0.997e-3	-0.616e-4	-0.9971	-1
140e9	-0.999e-3	-0.616e-4	-0.9999	-1

Table A2.2 Voltage generation and force distribution on the rigid cylinder of single sensor at the compliance of cylinder 3.3×10^4

Sensed object Modulus (N/m ²)	Voltage (V)		Force at Rigid Cylinder (N)	Total Force (N)
	PVDF-2	PVDF-1		
1.49e4	-0.130e-3	-0.616e-4	-0.1301	-1
1.66e4	-0.134e-3	-0.616e-4	-0.1336	-1
1.83e4	-0.137e-3	-0.616e-4	-0.1372	-1
2e4	-0.141e-3	-0.616e-4	-0.1407	-1
2.5e4	-0.151e-3	-0.616e-4	-0.1509	-1
3e4	-0.161e-3	-0.616e-4	-0.1609	-1
3.35e4	-0.168e-3	-0.616e-4	-0.1678	-1
3.7e4	-0.174e-3	-0.616e-4	-0.1745	-1
4.43e4	-0.188e-3	-0.616e-4	-0.1882	-1
5.16e4	-0.201e-3	-0.616e-4	-0.2014	-1
5.89e4	-0.214e-3	-0.616e-4	-0.2143	-1
6.62e4	-0.226e-3	-0.616e-4	-0.2267	-1
7.35e4	-0.238e-3	-0.616e-4	-0.2387	-1
8.08e4	-0.250e-3	-0.616e-4	-0.2504	-1
8.81e4	-0.261e-3	-0.616e-4	-0.2617	-1
9.54e4	-0.272e-3	-0.616e-4	-0.2727	-1
10.27e4	-0.283e-3	-0.616e-4	-0.2833	-1
1.1e5	-0.293e-3	-0.616e-4	-0.2937	-1
1.24e5	-0.312e-3	-0.616e-4	-0.3127	-1

1.31e5	-0.321e-3	-0.616e-4	-0.3218	-1
1.38e5	-0.330e-3	-0.616e-4	-0.3307	-1
1.97e5	-0.397e-3	-0.616e-4	-0.3974	-1
2.56e5	-0.451e-3	-0.616e-4	-0.4519	-1
3.13e5	-0.495e-3	-0.616e-4	-0.4960	-1
3.7e5	-0.533e-3	-0.616e-4	-0.5335	-1
4.3e5	-0.567e-3	-0.616e-4	-0.5635	-1
4.9e5	-0.596e-3	-0.616e-4	-0.5874	-1
6.1e5	-0.64e-3	-0.616e-4	-0.6167	-1
7.2e5	-0.679e-3	-0.616e-4	-0.6448	-1
8.46e5	-0.712e-3	-0.616e-4	-0.6799	-1
9.64e5	-0.736e-3	-0.616e-4	-0.7123	-1
1.08e6	-0.753e-3	-0.616e-4	-0.7373	-1
1.2e6	-0.775e-3	-0.616e-4	-0.7580	-1
1.3e6	-0.788e-3	-0.616e-4	-0.7762	-1
1.4e6	-0.800e-3	-0.616e-4	-0.8011	-1
1.7e6	-0.829e-3	-0.616e-4	-0.8295	-1
2e6	-0.850e-3	-0.616e-4	-0.8509	-1
2.5e6	-0.876e-3	-0.616e-4	-0.8766	-1
3e6	-0.894e-3	-0.616e-4	-0.8948	-1
3.5e6	-0.907e-3	-0.616e-4	-0.9083	-1
4.5e6	-0.926e-3	-0.616e-4	-0.9267	-1
5.5e6	-0.938e-3	-0.616e-4	-0.9394	-1
7.5e6	-0.954e-3	-0.616e-4	-0.9547	-1
9.5e6	-0.963e-3	-0.616e-4	-0.9639	-1
14e6	-0.974e-3	-0.616e-4	-0.9751	-1
70e6	-0.994e-3	-0.616e-4	-0.9949	-1
140e6	-0.997e-3	-0.616e-4	-0.9971	-1
140e9	-0.999e-3	-0.616e-4	-0.9999	-1

Table A2.3 Voltages generation and force distribution on the two circular PVDF films in common base model at compliance of 2.4×10^4 of outer cylinders

Sensed object Modulus (N/m ²)	Voltage (V)		Force (N)		Force Ratio
	PVDF-1	PVDF-2	PVDF-1	PVDF-2	
1.49e4	-0.440e-4	-0.44e-4	-0.04289	-0.04289	0.08578
1.66e4	-0.459e-4	-0.459e-4	-0.04434	-0.04434	0.08868
1.83e4	-0.474e-4	-0.474e-4	-0.04579	-0.04579	0.09158
2e4	-0.489e-4	-0.489e-4	-0.0472	-0.04720	-0.094400
2.5e4	-0.532e-4	-0.532e-4	-0.05140	-0.05140	-0.10280
3e4	-0.575e-4	-0.575e-4	-0.0550	-0.05500	-0.11000
3.35e4	-0.604e-4	-0.604e-4	-0.05833	-0.05833	-0.11660

3.7e4	-0.633e-4	-0.633e-4	-0.06112	-0.06112	-0.12220
4.43e4	-0.692e-4	-0.692e-4	-0.06683	-0.06683	-0.13366
5.16e4	-0.749e-4	-0.749e-4	-0.07239	-0.07239	-0.14478
5.89e4	-0.805e-4	-0.805e-4	-0.07781	-0.07781	-0.15562
6.62e4	-0.860e-4	-0.860e-4	-0.08309	-0.08309	-0.16618
7.35e4	-0.913e-4	-0.913e-4	-0.08825	-0.08825	-0.17650
8.08e4	-0.965e-4	-0.965e-4	-0.09327	-0.09327	-0.18654
8.81e4	-0.102e-3	-0.102e-3	-0.09818	-0.09818	-0.19636
9.54e4	-0.107e-3	-0.107e-3	-0.10290	-0.10290	-0.20580
10.27e4	-0.111e-3	-0.111e-3	-0.10760	-0.10760	-0.21520
1.1e5	-0.116e-3	-0.116e-3	-0.11220	-0.11220	-0.22440
1.24e5	-0.125e-3	-0.125e-3	-0.12068	-0.12068	-0.24136
1.31e5	-0.129e-3	-0.129e-3	-0.12478	-0.12478	-0.24956
1.38e5	-0.133e-3	-0.133e-3	-0.12879	-0.12879	-0.25758
1.97e5	-0.165e-3	-0.165e-3	-0.15946	-0.15946	-0.31892
2.56e5	-0.192e-3	-0.192e-3	-0.18539	-0.18539	-0.37078
3.13e5	-0.214e-3	-0.214e-3	-0.20700	-0.20700	-0.41400
3.7e5	-0.234e-3	-0.234e-3	-0.22588	-0.22588	-0.45176
4.3e5	-0.252e-3	-0.252e-3	-0.24324	-0.24324	-0.48648
4.9e5	-0.268e-3	-0.268e-3	-0.25854	-0.25854	-0.51708
6.1e5	-0.294e-3	-0.294e-3	-0.28425	-0.28425	-0.56850
7.2e5	-0.314e-3	-0.314e-3	-0.30343	-0.30343	-0.60686
8.46e5	-0.333e-3	-0.333e-3	-0.32160	-0.32160	-0.64320
9.64e5	-0.348e-3	-0.348e-3	-0.33582	-0.33582	-0.67164
1.08e6	-0.360e-3	-0.360e-3	-0.34774	-0.34774	-0.69548
1.2e6	-0.371e-3	-0.371e-3	-0.35838	-0.35838	-0.71676
1.3e6	-0.379e-3	-0.379e-3	-0.36617	-0.36618	-0.73235
1.4e6	-0.386e-3	-0.386e-3	-0.37316	-0.37316	-0.74632
1.7e6	-0.404e-3	-0.404e-3	-0.39032	-0.39032	-0.78064
2e6	-0.418e-3	-0.418e-3	-0.40339	-0.40339	-0.80678
2.5e6	0.434e-3	0.434e-3	-0.41940	-0.41940	-0.8388
3e6	0.446e-3	0.446e-3	-0.4308	-0.4308	-0.86172
3.5e6	0.455e-3	0.455e-3	-0.43946	-0.43946	-0.87892
4.5e6	-0.467e-3	-0.467e-3	-0.45153	-0.45153	-0.90306
5.5e6	-0.476e-3	-0.476e-3	-0.45958	-0.45958	-0.91916
7.5e6	-0.486e-3	-0.486e-3	-0.46966	-0.46966	-0.93932
9.5e6	-0.492e-3	-0.492e-3	-0.47572	-0.47572	-0.95144
14e6	-0.500e-3	-0.500e-3	-0.48324	-0.48324	-0.96648
70e6	-0.514e-3	-0.514e-3	-0.49655	-0.49655	-0.99310
140e6	-0.516e-3	-0.516e-3	-0.49820	-0.49820	-0.99640
140e9	-0.518e-3	-0.518e-3	-0.49990	-0.49990	-0.99800

Total force applied to the Two Sensor = -1N

Voltage generated by PVDF- 3= -0.213×10^{-4} V

Table A2.4 Voltages generation and force distribution on the two circular PVDF films in common base model at compliance of 3.3×10^4 of outer cylinders

Sensed object Modulus (N/m ²)	Voltage (V)		Force (N)		Force Ratio
	PVDF-1	PVDF-2	PVDF-1	PVDF-2	
1.49e4	-0.407e-4	-0.407e-4	-0.03937	-0.03937	-0.07874
1.66e4	-0.419e-4	-0.419e-4	-0.04044	-0.04044	-0.08089
1.83e4	-0.430e-4	-0.430e-4	-0.04152	-0.04152	-0.08303
2e4	-0.441e-4	-0.441e-4	-0.04258	-0.04258	-0.08516
2.5e4	-0.473e-4	-0.473e-4	-0.04569	-0.04569	-0.09138
3e4	-0.505e-4	-0.505e-4	-0.04876	-0.04876	-0.09751
3.35e4	-0.527e-4	-0.527e-4	-0.05088	-0.05088	-0.10176
3.7e4	-0.548e-4	-0.548e-4	-0.05298	-0.05298	-0.10596
4.43e4	-0.593e-4	-0.593e-4	-0.05730	-0.05730	-0.11460
5.16e4	-0.637e-4	-0.637e-4	-0.06154	-0.06154	-0.12308
5.89e4	-0.680e-4	-0.680e-4	-0.06569	-0.06569	-0.13138
6.62e4	-0.727e-4	-0.727e-4	-0.06977	-0.06977	-0.13954
7.35e4	-0.764e-4	-0.764e-4	-0.07378	-0.07378	-0.14756
8.08e4	-0.804e-4	-0.804e-4	-0.07771	-0.07771	-0.15542
8.81e4	-0.844e-4	-0.844e-4	-0.08157	-0.08157	-0.16314
9.54e4	-0.883e-4	-0.883e-4	-0.08535	-0.08535	-0.17070
10.27e4	-0.922e-4	-0.922e-4	-0.08908	-0.08908	-0.17816
1.1e5	-0.960e-4	-0.960e-4	-0.09273	-0.09273	-0.18546
1.24e5	-0.103e-3	-0.103e-3	-0.09956	-0.09956	-0.19912
1.31e5	-0.106e-3	-0.106e-3	-0.1028	-0.1028	-0.2056
1.38e5	-0.110e-3	-0.110e-3	-0.1061	-0.1061	-0.2122
1.97e5	-0.136e-3	-0.136e-3	-0.1317	-0.1317	-0.2634
2.56e5	-0.160e-3	-0.160e-3	-0.1542	-0.1542	-0.3084
3.13e5	-0.180e-3	-0.180e-3	-0.1734	-0.1734	-0.3469
3.7e5	-0.197e-3	-0.197e-3	-0.1906	-0.1906	-0.3812
4.3e5	-0.214e-3	-0.214e-3	-0.2069	-0.2069	-0.4138
4.9e5	-0.229e-3	-0.229e-3	-0.2216	-0.2216	-0.4432
6.1e5	-0.256e-3	-0.256e-3	-0.2468	-0.2468	-0.4936
7.2e5	-0.276e-3	-0.276e-3	-0.2668	-0.2668	-0.5336
8.46e5	-0.295e-3	-0.295e-3	-0.2852	-0.2852	-0.5704
9.64e5	-0.311e-3	-0.311e-3	-0.3003	-0.3003	-0.6007
1.08e6	-0.324e-3	-0.324e-3	-0.3133	-0.3133	-0.6266
1.2e6	-0.336e-3	-0.336e-3	-0.3250	-0.3250	-0.6500
1.3e6	-0.345e-3	-0.345e-3	-0.3337	-0.3337	-0.6674
1.4e6	-0.354e-3	-0.354e-3	-0.3416	-0.3416	-0.6832
1.7e6	-0.374e-3	-0.374e-3	-0.3613	-0.3613	-0.7226
2e6	-0.390e-3	-0.390e-3	-0.3766	-0.3766	-0.7532

2.5e6	-0.410e-3	-0.410e-3	-0.3958	-0.3958	-0.7916
3e6	-0.424e-3	-0.424e-3	-0.4099	-0.4099	-0.8198
3.5e6	-0.435e-3	-0.435e-3	-0.4206	-0.4206	-0.8412
4.5e6	-0.451e-3	-0.451e-3	-0.4358	-0.4358	-0.8716
5.5e6	-0.462e-3	-0.462e-3	-0.4461	-0.4461	-0.8922
7.5e6	-0.475e-3	-0.475e-3	-0.4592	-0.4592	-0.9184
9.5e6	-0.484e-3	-0.484e-3	-0.4672	-0.4672	-0.9344
14e6	-0.494e-3	-0.494e-3	-0.4777	-0.4777	-0.9554
70e6	-0.513e-6	-0.513e-6	-0.4952	-0.4952	-0.9904
140e6	-0.515e-3	-0.515e-3	-0.4976	-0.4976	-0.9952
140e9	-0.517e-3	-0.517e-3	-0.4999	-0.4999	-0.9998

Total force applied to the Two Sensor = -1 N

Voltage generated by PVDF-3 = -0.213×10^{-4} V

Table A2.5 Voltages generation and force distribution on the two circular PVDF films in different base model at compliance of 2.4×10^4 of outer cylinders.

Sensed object Modulus (N/m ²)	Voltage (V)		Force (N)		Force Ratio		Total Ratio
	PVDF 1	PVDF 3	PVDF 1	PVDF 3	Left	Right	
1.49e4	-0.440e-4	-0.44e-4	-0.04289	-0.04289	-0.08578	-0.08578	-0.08578
1.66e4	-0.459e-4	-0.459e-4	-0.04434	-0.04434	-0.08868	-0.08868	-0.08868
1.83e4	-0.474e-4	-0.474e-4	-0.04579	-0.04579	-0.09158	-0.09158	-0.09158
2e4	-0.489e-4	-0.489e-4	-0.0472	-0.04720	-0.94400	-0.94400	-0.94400
2.5e4	-0.532e-4	-0.532e-4	-0.05140	-0.05140	-0.10280	-0.10280	-0.10280
3e4	-0.575e-4	-0.575e-4	-0.0550	-0.05500	-0.11000	-0.11000	-0.11000
3.35e4	-0.604e-4	-0.604e-4	-0.05833	-0.05833	-0.11660	-0.11660	-0.11660
3.7e4	-0.633e-4	-0.633e-4	-0.06112	-0.06112	-0.12220	-0.12220	-0.12220
4.43e4	-0.692e-4	-0.692e-4	-0.06683	-0.06683	-0.13366	-0.13366	-0.13366
5.16e4	-0.749e-4	-0.749e-4	-0.07239	-0.07239	-0.14478	-0.14478	-0.14478
5.89e4	-0.805e-4	-0.805e-4	-0.07781	-0.07781	-0.15562	-0.15562	-0.15562
6.62e4	-0.860e-4	-0.860e-4	-0.08309	-0.08309	-0.16618	-0.16618	-0.16618
7.35e4	-0.913e-4	-0.913e-4	-0.08825	-0.08825	-0.17650	-0.17650	-0.17650
8.08e4	-0.965e-4	-0.965e-4	-0.09327	-0.09327	-0.18654	-0.18654	-0.18654
8.81e4	-0.102e-3	-0.102e-3	-0.09818	-0.09818	-0.19636	-0.19636	-0.19636
9.54e4	-0.107e-3	-0.107e-3	-0.10290	-0.10290	-0.20580	-0.20580	-0.20580
10.27e4	-0.111e-3	-0.111e-3	-0.10760	-0.10760	-0.21520	-0.21520	-0.21520
1.1e5	-0.116e-3	-0.116e-3	-0.11220	-0.11220	-0.22440	-0.22440	-0.22440
1.24e5	-0.125e-3	-0.125e-3	-0.12068	-0.12068	-0.24136	-0.24136	-0.24136
1.31e5	-0.129e-3	-0.129e-3	-0.12478	-0.12478	-0.24956	-0.24956	-0.24956
1.38e5	-0.133e-3	-0.133e-3	-0.12879	-0.12879	-0.25758	-0.25758	-0.25758

1.97e5	-0.165e-3	-0.165e-3	-0.15946	-0.15946	-0.31892	-0.31892	-0.31892
2.56e5	-0.192e-3	-0.192e-3	-0.18539	-0.18539	-0.37078	-0.37078	-0.37078
3.13e5	-0.214e-3	-0.214e-3	-0.20700	-0.20700	-0.41400	-0.41400	-0.41400
3.7e5	-0.234e-3	-0.234e-3	-0.22588	-0.22588	-0.45176	-0.45176	-0.45176
4.3e5	-0.252e-3	-0.252e-3	-0.24324	-0.24324	-0.48648	-0.48648	-0.48648
4.9e5	-0.268e-3	-0.268e-3	-0.25854	-0.25854	-0.51708	-0.51708	-0.51708
6.1e5	-0.294e-3	-0.294e-3	-0.28425	-0.28425	-0.56850	-0.56850	-0.56850
7.2e5	-0.314e-3	-0.314e-3	-0.30343	-0.30343	-0.60686	-0.60686	-0.60686
8.46e5	-0.333e-3	-0.333e-3	-0.32160	-0.32160	-0.64320	-0.64320	-0.64320
9.64e5	-0.348e-3	-0.348e-3	-0.33582	-0.33582	-0.67164	-0.67164	-0.67164
1.08e6	-0.360e-3	-0.360e-3	-0.34774	-0.34774	-0.69548	-0.69548	-0.69548
1.2e6	-0.371e-3	-0.371e-3	-0.35838	-0.35838	-0.71676	-0.71676	-0.71676
1.3e6	-0.379e-3	-0.379e-3	-0.36617	-0.366178	-0.73235	-0.73235	-0.73235
1.4e6	-0.386e-3	-0.386e-3	-0.37316	-0.37316	-0.74632	-0.74632	-0.74632
1.7e6	-0.404e-3	-0.404e-3	-0.39032	-0.39032	-0.78064	-0.78064	-0.78064
2e6	-0.418e-3	-0.418e-3	-0.40339	-0.40339	-0.80678	-0.80678	-0.80678
2.5e6	0.434e-3	0.434e-3	-0.41940	-0.41940	-0.8388	-0.8388	-0.8388
3e6	0.446e-3	0.446e-3	-0.43086	-0.43086	-0.86172	-0.86172	-0.86172
3.5e6	0.455e-3	0.455e-3	-0.43946	-0.43946	-0.87892	-0.87892	-0.87892
4.5e6	-0.467e-3	-0.467e-3	-0.45153	-0.45153	-0.90306	-0.90306	-0.90306
5.5e6	-0.476e-3	-0.476e-3	-0.45958	-0.45958	-0.91916	-0.91916	-0.91916
7.5e6	-0.486e-3	-0.486e-3	-0.46966	-0.46966	-0.93932	-0.93932	-0.93932
9.5e6	-0.492e-3	-0.492e-3	-0.47572	-0.47572	-0.95144	-0.95144	-0.95144
14e6	-0.500e-3	-0.500e-3	-0.48324	-0.48324	-0.96648	-0.96648	-0.96648
70e6	-0.514e-3	-0.514e-3	-0.49655	-0.49655	-0.99310	-0.99310	-0.99310
140e6	-0.516e-3	-0.516e-3	-0.49820	-0.49820	-0.99640	-0.99640	-0.99640
140e9	-0.518e-3	-0.518e-3	-0.49990	-0.49990	-0.99800	-0.99800	-0.99800

Total force applied to the Two Sensor = -1 N

Force on the PVDF-2 and PVDF-4 = - 0.5 N

Voltage generated by PVDF-2 and PVDF-4 = $-0.313 \times 10^{-4} \text{V}$

Table A2.6 Voltages generation and force distribution on the two circular PVDF films in different base model at compliance of 3.3×10^4 of outer cylinders.

Sensed object Modulus (N/m ²)	Voltage(V)		Force(N)		Force Ratio		Total Ratio
	PVDF 1	PVDF 3	PVDF 1	PVDF 3	Left	Right	
1.49e4	-0.407e-4	-0.407e-4	-0.03937	-0.03937	-0.07874	-0.07874	-0.07874
1.66e4	-0.419e-4	-0.419e-4	-0.04044	-0.04044	-0.08089	-0.08089	-0.08089
1.83e4	-0.430e-4	-0.430e-4	-0.04152	-0.04152	-0.08303	-0.08303	-0.08303
2e4	-0.441e-4	-0.441e-4	-0.04258	-0.04258	-0.08516	-0.08516	-0.08516
2.5e4	-0.473e-4	-0.473e-4	-0.04569	-0.04569	-0.09138	-0.09138	-0.09138
3e4	-0.505e-4	-0.505e-4	-0.04876	-0.04876	-0.09751	-0.09751	-0.09751

3.35e4	-0.527e-4	-0.527e-4	-0.05088	-0.05088	-0.10176	-0.10176	-0.10176
3.7e4	-0.548e-4	-0.548e-4	-0.05298	-0.05298	-0.10596	-0.10596	-0.10596
4.43e4	-0.593e-4	-0.593e-4	-0.05730	-0.05730	-0.11460	-0.11460	-0.11460
5.16e4	-0.637e-4	-0.637e-4	-0.06154	-0.06154	-0.12308	-0.12308	-0.12308
5.89e4	-0.680e-4	-0.680e-4	-0.06569	-0.06569	-0.13138	-0.13138	-0.13138
6.62e4	-0.727e-4	-0.727e-4	-0.06977	-0.06977	-0.13954	-0.13954	-0.13954
7.35e4	-0.764e-4	-0.764e-4	-0.07378	-0.07378	-0.14756	-0.14756	-0.14756
8.08e4	-0.804e-4	-0.804e-4	-0.07771	-0.07771	-0.15542	-0.15542	-0.15542
8.81e4	-0.844e-4	-0.844e-4	-0.08157	-0.08157	-0.16314	-0.16314	-0.16314
9.54e4	-0.883e-4	-0.883e-4	-0.08535	-0.08535	-0.17070	-0.17070	-0.17070
10.27e4	-0.922e-4	-0.922e-4	-0.08908	-0.08908	-0.17816	-0.17816	-0.17816
1.1e5	-0.960e-4	-0.960e-4	-0.09273	-0.09273	-0.18546	-0.18546	-0.18546
1.24e5	-0.103e-3	-0.103e-3	-0.09956	-0.09956	-0.19912	-0.19912	-0.19912
1.31e5	-0.106e-3	-0.106e-3	-0.1028	-0.1028	-0.2056	-0.2056	-0.2056
1.38e5	-0.110e-3	-0.110e-3	-0.1061	-0.1061	-0.2122	-0.2122	-0.2122
1.97e5	-0.136e-3	-0.136e-3	-0.1317	-0.1317	-0.2634	-0.2634	-0.2634
2.56e5	-0.160e-3	-0.160e-3	-0.1542	-0.1542	-0.3084	-0.3084	-0.3084
3.13e5	-0.180e-3	-0.180e-3	-0.1734	-0.1734	-0.3469	-0.3469	-0.3469
3.7e5	-0.197e-3	-0.197e-3	-0.1906	-0.1906	-0.3812	-0.3812	-0.3812
4.3e5	-0.214e-3	-0.214e-3	-0.2069	-0.2069	-0.4138	-0.4138	-0.4138
4.9e5	-0.229e-3	-0.229e-3	-0.2216	-0.2216	-0.4432	-0.4432	-0.4432
6.1e5	-0.256e-3	-0.256e-3	-0.2468	-0.2468	-0.4936	-0.4936	-0.4936
7.2e5	-0.276e-3	-0.276e-3	-0.2668	-0.2668	-0.5336	-0.5336	-0.5336
8.46e5	-0.295e-3	-0.295e-3	-0.2852	-0.2852	-0.5704	-0.5704	-0.5704
9.64e5	-0.311e-3	-0.311e-3	-0.3003	-0.3003	-0.6007	-0.6007	-0.6007
1.08e6	-0.324e-3	-0.324e-3	-0.3133	-0.3133	-0.6266	-0.6266	-0.6266
1.2e6	-0.336e-3	-0.336e-3	-0.3250	-0.3250	-0.6500	-0.6500	-0.6500
1.3e6	-0.345e-3	-0.345e-3	-0.3337	-0.3337	-0.6674	-0.6674	-0.6674
1.4e6	-0.354e-3	-0.354e-3	-0.3416	-0.3416	-0.6832	-0.6832	-0.6832
1.7e6	-0.374e-3	-0.374e-3	-0.3613	-0.3613	-0.7226	-0.7226	-0.7226
2e6	-0.390e-3	-0.390e-3	-0.3766	-0.3766	-0.7532	-0.7532	-0.7532
2.5e6	-0.410e-3	-0.410e-3	-0.3958	-0.3958	-0.7916	-0.7916	-0.7916
3e6	-0.424e-3	-0.424e-3	-0.4099	-0.4099	-0.8198	-0.8198	-0.8198
3.5e6	-0.435e-3	-0.435e-3	-0.4206	-0.4206	-0.8412	-0.8412	-0.8412
4.5e6	-0.451e-3	-0.451e-3	-0.4358	-0.4358	-0.8716	-0.8716	-0.8716
5.5e6	-0.462e-3	-0.462e-3	-0.4461	-0.4461	-0.8922	-0.8922	-0.8922
7.5e6	-0.475e-3	-0.475e-3	-0.4592	-0.4592	-0.9184	-0.9184	-0.9184
9.5e6	-0.484e-3	-0.484e-3	-0.4672	-0.4672	-0.9344	-0.9344	-0.9344
14e6	-0.494e-3	-0.494e-3	-0.4777	-0.4777	-0.9554	-0.9554	-0.9554
70e6	-0.513e-3	-0.513e-3	-0.4952	-0.4952	-0.9904	-0.9904	-0.9904
140e6	-0.515e-3	-0.515e-3	-0.4976	-0.4976	-0.9952	-0.9952	-0.9952
140e9	-0.517e-3	-0.517e-3	-0.4999	-0.4999	-0.9998	-0.9998	-0.9998

Total force applied to the Two Sensor = -1 N

Force on the PVDF-2 and PVDF-4 = - 0.5 N

Voltage generated by PVDF-2 and PVDF- 4 = $-0.313 \times 10^{-4} \text{V}$

Table A2.7 Effect of different positions of force applied along X-axis on the force-ratio in sensor with common base.

X-distance	Voltage(V)			Force(N)			Force Ratio
	PVDF 2	PVDF 1	PVDF 3	PVDF 2	PVDF 1	PVDF 3	
1	2.13E-02	2.41E-05	4.61E-04	-1	0.02424	0.46158	0.48582
2	2.13E-02	2.41E-05	4.61E-04	-1	0.02424	0.46177	0.48601
3	2.13E-02	2.41E-05	4.62E-04	-1	0.02416	0.46355	0.48771
4	2.13E-02	2.41E-05	4.61E-04	-1	0.02424	0.46166	0.4859
5	2.13E-02	2.19E-05	5.13E-04	-1	0.02189	0.5139	0.53579
6	2.13E-02	2.51E-06	9.41E-04	-1	0.002517	0.94415	0.946667
7	2.13E-02	9.40E-08	9.98E-04	-1	9.41E-05	0.99788	0.997974
8	2.13E-02	2.55E-06	9.43E-04	-1	2.56E-03	0.94411	0.946668
9	2.13E-02	2.18E-05	5.12E-04	-1	2.19E-02	0.51395	0.53588
10	2.13E-02	2.51E-05	4.60E-04	-1	0.025162	0.4607	0.485862
11	2.13E-02	2.54E-05	4.61E-04	-1	0.025428	0.46229	0.487718
12	2.13E-02	4.60E-05	4.38E-04	-1	4.61E-02	0.43994	0.48604
13	2.13E-02	2.43E-04	2.42E-04	-1	0.2432	0.2432	0.4864
14	2.13E-02	4.38E-04	4.60E-05	-1	0.43994	4.61E-02	0.48604
15	2.13E-02	4.61E-04	2.54E-05	-1	0.46229	0.025428	0.487718
16	2.13E-02	4.60E-04	2.51E-05	-1	0.4607	0.025162	0.485862
17	2.13E-02	5.12E-04	2.18E-05	-1	0.51395	2.19E-02	0.53588
18	2.13E-02	9.43E-04	2.55E-06	-1	0.94411	2.56E-03	0.946668
19	2.13E-02	9.98E-04	9.40E-08	-1	0.99788	9.41E-05	0.997974
20	2.13E-02	9.41E-04	2.51E-06	-1	0.94415	0.002517	0.946667
21	2.13E-02	5.13E-04	2.19E-05	-1	0.5139	0.02189	0.53579
22	2.13E-02	4.61E-04	2.41E-05	-1	0.46166	0.02424	0.4859
23	2.13E-02	4.62E-04	2.41E-05	-1	0.46355	0.02416	0.48771
24	2.13E-02	4.61E-04	2.41E-05	-1	0.46177	0.02424	0.48601
25	2.13E-02	4.61E-04	2.41E-05	-1	0.46158	0.02424	0.48582

Table A2.8 Effect of different positions of force applied along the X-axis on the force ratio, for sensor with different base.

X-distance	Voltage (V)				Force (N)				Force Ratio		Total Ratio
	PVDF 1	PVDF 2	PVDF 3	PVDF 4	PVDF 1	PVDF 2	PVDF 3	PVDF 4	Left	Right	
1	5.84e-05	3.08e-06	2.41e-05	4.62e-04	0.94999	0.05009	0.02424	0.46158	0.4858	0.4839	0.4848
2	5.84e-05	3.08e-06	2.41e-05	4.62e-04	0.9499	0.05008	0.024235	0.46177	0.49	0.4839	0.487
3	5.84e-05	3.06e-06	2.40e-05	4.62e-04	0.94998	0.05009	0.024154	0.4635	0.4879	0.4822	0.4851
4	5.84e-05	3.06e-06	2.38e-05	4.62e-04	0.9499	0.05009	0.0243	0.46166	0.486	0.4837	0.4849
5	5.86e-05	2.78e-06	2.18e-05	5.15e-04	0.9547	0.04522	0.02188	0.5139	0.5382	0.4838	0.511
6	6.11e-05	3.19e-07	2.51e-06	9.48e-04	0.9947	0.0052	0.002516	0.9441	0.9491	0.4838	0.7164
7	6.14e-05	1.19e-08	9.40e-10	9.74e-04	0.9998	0.00019	0.0000941	0.99788	0.998	0.4838	0.7409
8	6.11e-05	3.24e-07	2.56e-06	9.48e-04	0.9947	0.00528	0.002558	0.9441	0.9491	0.4844	0.7168
9	5.86e-05	2.78e-06	2.19e-05	5.15e-04	0.9547	0.04531	0.0219	0.5139	0.5382	0.4833	0.5108
10	5.82e-05	3.19e-06	2.51e-05	4.63e-04	0.948	0.05198	0.02516	0.4607	0.4859	0.484	0.485
11	5.82e-05	3.22e-06	2.55e-05	4.64e-04	0.9474	0.0525	0.02541	0.4613	0.4869	0.484	0.4851
12	5.86e-05	5.85e-06	4.60e-05	4.41e-04	0.9047	0.0952	0.04614	0.4399	0.4862	0.4846	0.4854
13	3.07e-05	3.07e-05	2.44e-04	2.44e-04	0.5	0.5	0.25	0.25	0.5	0.5	0.5
14	5.85e-06	5.86e-05	4.41e-04	4.60e-05	0.0952	0.9047	0.4399	0.04614	0.4846	0.4862	0.4854
15	3.22e-06	5.82e-05	4.64e-04	2.55e-05	0.0525	0.9474	0.4613	0.02541	0.484	0.4869	0.4851
16	3.19e-06	5.82e-05	4.63e-04	2.51e-05	0.05198	0.948	0.4607	0.02516	0.484	0.4859	0.485
17	2.78e-06	5.86e-05	5.15e-04	2.19e-05	0.04531	0.9547	0.5139	0.0219	0.4833	0.5382	0.5108
18	3.24e-07	6.11e-05	9.48e-04	2.56e-06	0.00528	0.9947	0.9441	0.002558	0.4844	0.9491	0.7168
19	1.19e-08	6.14e-05	9.74e-04	9.40e-10	0.00019	0.9998	0.99788	9.41e-05	0.4838	0.998	0.7409
20	3.19e-07	6.11e-05	9.48e-04	2.51e-06	0.0052	0.9947	0.9441	0.002516	0.4838	0.9491	0.7164
21	2.78e-06	5.86e-05	5.15e-04	2.18e-05	0.04522	0.9547	0.5139	0.02188	0.4838	0.5382	0.511
22	3.06e-06	5.84e-05	4.62e-04	2.38e-05	0.05009	0.9499	0.46166	0.0243	0.4837	0.486	0.4849
23	3.06e-06	5.84e-05	4.62e-04	2.40e-05	0.05009	0.94998	0.4635	0.024154	0.4822	0.4879	0.4851
24	3.08e-06	5.84e-05	4.62e-04	2.41e-05	0.05008	0.9499	0.46177	0.024235	0.4839	0.49	0.487
25	3.08e-06	5.84e-05	4.62e-04	2.41e-05	0.05009	0.94999	0.46158	0.02424	0.4839	0.4858	0.4848

Table A2.9 Experimental data for the single sensor at six different load sets for sample 1

Sample No. 1							
Load (N)	Meter Reading	Oscilloscope (mV)	PVDF 2 (mV)	PVDF 1 (mV)	Force Rigid (N)	Total Force (N)	Force Ratio
1.5	16	16.01	2.87	104	0.471	1.501	0.311
2	21	21.34	4.00	145	0.657	2.092	0.320
2.5	27	26.68	5.08	184	0.834	2.655	0.295
3	32	32.02	5.87	213	0.964	3.074	0.329
3.5	37	37.35	6.84	248	1.123	3.579	0.317
4	43	42.69	7.86	285	1.291	4.112	0.311
Average Force Ratio							0.314

Table A2.10 Experimental data for the single sensor at six different load sets for sample 2

Sample No. 2							
Load (N)	Meter Reading	Oscilloscope (mV)	PVDF 2 (mV)	PVDF 1 (mV)	Force Rigid (N)	Total Force (N)	Force Ratio
1.5	16	15.90	1.206	100.00	0.202	1.429	0.141
2	21	21.20	1.785	148.00	0.290	2.178	0.133
2.5	27	26.50	2.147	178.00	0.370	2.414	0.153
3	32	31.80	2.484	206.00	0.432	3.121	0.139
3.5	37	37.10	2.906	241.00	0.511	3.512	0.145
4	43	42.40	3.329	276.00	0.552	3.943	0.140
Average Force Ratio							0.142

Table A2.11 Experimental data for the single sensor at six different load sets for sample 3

Sample No. 3							
Load (N)	Meter Reading	Oscilloscope (mV)	PVDF 2 (mV)	PVDF 1 (mV)	Force Rigid (N)	Total Force (N)	Force Ratio
1.5	16	16.05	1.645	106.00	0.276	1.514	0.182
2	21	21.39	2.235	144.00	0.363	2.119	0.171
2.5	27	26.74	2.716	175.00	0.468	2.374	0.197
3	32	32.09	3.290	212.00	0.573	3.212	0.178
3.5	37	37.43	3.818	246.00	0.671	3.585	0.187
4	43	42.78	4.470	288.00	0.741	4.114	0.180
Average Force Ratio							0.183

Table A2.12 Experimental data for the single sensor at six different load sets for sample 4

Sample No. 4							
Load (N)	Meter Reading	Oscilloscope (mV)	PVDF 2 (mV)	PVDF 1 (mV)	Force Rigid (N)	Total Force (N)	Force Ratio
1.5	16	15.31	2.172	110	0.353	1.619	0.218
2	21	21.2	2.922	148	0.489	2.114	0.231
2.5	27	26.93	3.514	178	0.542	2.697	0.201
3	32	32.85	4.304	218	0.742	3.334	0.223
3.5	37	37.27	4.916	249	0.815	3.844	0.212
4	43	43.98	5.765	292	0.937	4.256	0.220
Average Force Ratio							0.218

Table A2.13 Experimental data for the single sensor at six different load sets for sample 5

Sample No. 5							
Load (N)	Meter Reading	Oscilloscope (mV)	PVDF 2 (mV)	PVDF 1 (mV)	Force Rigid (N)	Total Force (N)	Force Ratio
1.5	16	15.16	1.522	102	0.252	1.501	0.168
2	21	20.56	2.178	146	0.365	2.086	0.175
2.5	27	27.6	2.536	170	0.391	2.576	0.152
3	32	34.2	2.983	200	0.514	3.059	0.168
3.5	37	39.4	3.580	240	0.594	3.706	0.160
4	43	45.6	4.057	272	0.659	3.964	0.166
Average Force Ratio							0.165

Table A2.14 Experimental data for the single sensor at six different load sets for sample 6

Sample No. 6							
Load (N)	Meter Reading	Oscilloscope (mV)	PVDF 1 (mV)	PVDF 2 (mV)	Force Rigid (N)	Total Force (N)	Force Ratio
1.5	16	15.23	2.439	104	0.408	1.501	0.272
2	21	21.3	3.377	144	0.549	2.078	0.264
2.5	27	27.9	4.080	174	0.703	2.511	0.280
3	32	32.8	5.018	214	0.873	3.088	0.283
3.5	37	38.5	5.699	243	1.001	3.506	0.286
4	43	43.3	6.519	278	1.081	4.011	0.269
Average Force Ratio							0.276

Table A2.15 Experimental data for the two sensors on the common base, at the different load sets, sample 1

Sample 1			mV	mV	mV	N	N	N	
Load (N)	Meter Reading	Oscill Oscope (mV)	PVDF 1	PVDF 2	PVDF 3	Force 1	Force 2	Total Force	Force Ratio
1.5	16	16.09	1.435	1.363	34.722	0.236	0.191	1.493	0.286
2	21	21.58	2.000	2.260	51.389	0.329	0.378	2.391	0.295
2.5	27	28.85	2.540	2.515	61.806	0.417	0.368	2.821	0.278
3	32	33.70	2.935	3.375	71.528	0.482	0.574	3.422	0.309
3.5	37	39.24	3.420	3.523	83.681	0.562	0.536	4.040	0.272
4	43	46.15	3.930	3.734	95.833	0.646	0.524	4.416	0.265
4.5	48	49.08	4.350	4.698	105.469	0.715	0.750	4.860	0.301
Average Force Ratio									0.287

Table A2.16 Experimental data for the two sensors on the common base, at the different load sets, sample 2

Sample 2			mV	mV	mV	N	N	N	
Load (N)	Meter Reading	Oscill Oscope (mV)	PVDF 1	PVDF 2	PVDF 3	Force 1	Force 2	Total Force	Force Ratio
1.5	16	14.80	0.675	0.573	37.143	0.112	0.080	1.534	0.125
2	21	19.86	0.875	1.008	51.786	0.127	0.168	2.139	0.138
2.5	27	26.54	1.138	1.063	65.714	0.178	0.156	2.715	0.123
3	32	31.00	1.292	1.429	76.071	0.199	0.243	3.143	0.140
3.5	37	36.10	1.584	1.497	88.571	0.255	0.228	3.659	0.132
4	43	42.46	1.831	1.581	101.786	0.298	0.222	4.205	0.124
4.5	48	51.36	2.054	2.112	115.357	0.319	0.337	4.766	0.138
Average Force Ratio									0.131

Table A2.17 Experimental data for the two sensors on the common base, at the different load sets, sample 3

Sample 3			mV	mV	mV	N	N	N	
Load (N)	Meter Reading	Oscill Oscope (mV)	PVDF 1	PVDF 2	PVDF 3	Force 1	Force 2	Total Force	Force Ratio
1.5	16	15.44	0.921	0.781	37.931	0.122	0.129	1.480	0.170
2	21	20.72	1.095	1.263	51.034	0.173	0.183	2.368	0.150
2.5	27	27.69	1.439	1.344	61.379	0.199	0.211	2.496	0.164
3	32	32.35	1.711	1.892	75.172	0.275	0.291	3.550	0.159
3.5	37	37.67	2.081	1.966	85.862	0.299	0.317	3.632	0.170
4	43	44.31	2.458	2.123	100.690	0.326	0.345	3.929	0.171
4.5	48	53.59	2.690	2.766	117.241	0.406	0.429	5.200	0.161
Average Force Ratio									0.164

Table A2.18 Experimental data for the two sensors on the common base, at the different load sets, sample 4

Sample 4			mV	mV	mV	N	N	N	
Load (N)	Meter Reading	Oscill-scope (mV)	PVDF 1	PVDF 2	PVDF 3	Force 1	Force 2	Total Force	Force Ratio
1.5	16	15.76	1.216	1.032	38.129	0.133	0.148	1.472	0.191
2	21	21.15	1.432	1.651	51.799	0.186	0.207	1.999	0.197
2.5	27	28.27	1.862	1.739	62.950	0.212	0.236	2.429	0.185
3	32	33.03	2.238	2.475	76.259	0.296	0.330	2.943	0.213
3.5	37	38.46	2.679	2.532	88.489	0.317	0.354	3.415	0.196
4	43	45.23	3.171	2.738	103.597	0.346	0.386	3.998	0.183
4.5	48	54.71	3.484	3.583	118.345	0.433	0.482	4.567	0.200
Average Force Ratio									0.195

Table A2.19 Experimental data for the two sensors on the common base, at the different load sets, sample 5

Sample 5			mV	mV	mV	N	N	N	
Load (N)	Meter Reading	Oscill Oscope (mV)	PVDF 2	PVDF 3	PVDF 1	Force 1	Force 2	Total Force	Force Ratio
1.5	16	-15.12	0.852	0.723	35.417	0.133	0.104	1.563	0.152
2	21	-20.29	1.067	1.230	50.694	0.146	0.210	2.238	0.159
2.5	27	-27.12	1.344	1.255	59.028	0.199	0.188	2.605	0.148
3	32	-31.68	1.551	1.715	69.444	0.225	0.298	3.065	0.171
3.5	37	-36.89	1.951	1.843	83.333	0.297	0.287	3.678	0.159
4	43	-43.38	2.231	1.927	94.444	0.343	0.277	4.169	0.149
4.5	48	-52.48	2.375	2.442	115.278	0.348	0.399	5.088	0.147
Average Force Ratio									0.155

Table A2.20 Experimental data for the two sensors on the common base, at the different load sets, sample 6

Sample 6			mV	mV	mV	N	N	N	
Load (N)	Meter Reading	Oscill Oscope (mV)	PVDF 2	PVDF 3	PVDF 1	Force 1	Force 2	Total Force	Force Ratio
1.5	16	-16.89	1.366	1.158	34.437	0.191	0.183	1.486	0.251
2	21	-22.66	1.655	1.908	47.682	0.202	0.358	2.057	0.272
2.5	27	-30.29	2.163	2.020	57.616	0.286	0.332	2.486	0.249
3	32	-35.38	2.610	2.886	70.861	0.339	0.551	3.057	0.291
3.5	37	-41.20	3.106	2.935	80.464	0.423	0.501	3.472	0.266
4	43	-48.46	3.586	3.097	92.053	0.492	0.488	3.972	0.247
4.5	48	-58.62	3.799	3.907	112.58	0.498	0.700	4.858	0.247
Average Force Ratio									0.260

Table A2.21 Experimental data for the two sensors on the different base arrangement, at the different load sets, sample 1

Sample1		mV		N							
Force (N)	Meter Reading	Oscillo-scope(mV)	PVDF 1	PVDF 2	PVDF 3	PVDF 4	Force 1	Force 2	Force 3	Force 4	Force Ratio
1.5	16	16.00	1.473	43.89	1.45	45.06	0.247	0.644	0.235	0.663	0.369
2	21	21.34	1.964	58.52	1.91	58.91	0.319	0.867	0.320	0.841	0.374
2.5	27	26.68	2.455	73.15	2.48	79.58	0.423	1.079	0.383	1.206	0.355
3	32	32.02	2.946	87.78	3.01	97.32	0.513	1.475	0.518	1.489	0.348
3.5	37	37.35	3.437	102.41	3.54	115.70	0.604	1.686	0.587	1.786	0.343
4	43	42.69	3.928	117.04	3.82	117.81	0.651	1.683	0.621	1.717	0.374
4.5	48	48.03	4.418	131.67	4.47	143.25	0.761	2.232	0.792	2.170	0.353
Average Force Ratio											0.359

Table A2.22 Experimental data for the two sensors on the different base arrangement, at the different load sets, sample 2

Sample 2		mV				N					
Force (N)	Meter Reading	Oscillo-scope(mV)	PVDF 1	PVDF 2	PVDF 3	PVDF 4	Force 1	Force 2	Force 3	Force 4	Force Ratio
1.5	16	14.40	0.630	51.00	0.687	49.50	0.094	0.692	0.095	0.700	0.135
2	21	19.20	0.840	73.26	0.907	75.48	0.117	1.024	0.125	1.133	0.113
2.5	27	24.01	1.050	93.45	1.179	83.66	0.165	1.204	0.159	1.067	0.143
3	32	28.82	1.260	109.18	1.428	108.15	0.202	1.571	0.217	1.721	0.127
3.5	37	33.61	1.469	128.93	1.682	121.70	0.240	1.785	0.249	1.791	0.137
4	43	38.42	1.679	139.38	1.814	136.62	0.245	1.892	0.248	1.932	0.129
4.5	48	43.23	1.889	173.25	2.122	178.20	0.286	2.345	0.317	2.590	0.122
Average force Ratio											0.129

Table A2.23 Experimental data for the two sensors on the different base arrangement, at the different load sets, sample 3

Sample 3			mV				N			
Force (N)	Meter Reading	Oscilloscope(mV)	PVDF 1	PVDF 2	PVDF 3	PVDF 4	Force 1	Force 2	Force 3	Force 4
1.5	16	15.37	0.823	53	0.931	54.060	0.141	0.750	0.159	0.788
2	21	20.48	1.117	72	1.230	71.280	0.180	1.081	0.198	1.039
2.5	27	25.61	1.358	87.50	1.598	91.875	0.246	1.116	0.289	1.308
3	32	30.74	1.645	106	1.936	112.360	0.303	1.686	0.357	1.805
3.5	37	35.85	1.909	123	2.280	131.610	0.359	1.811	0.429	2.052
4	43	40.98	2.235	144	2.459	145.440	0.374	2.037	0.412	2.098
4.5	48	46.11	2.430	167.5	2.876	175.875	0.433	2.465	0.512	2.665
Average Force Ratio										0.194

Table A2.24 Experimental data for the two sensors on the different base arrangement, at the different load sets, sample 4

Sample 4			mV				N			
Force (N)	Meter Reading	Oscilloscope(mV)	PVDF 1	PVDF 2	PVDF 3	PVDF 4	Force 1	Force 2	Force 3	Force 4
1.5	16	15.688	1.108	52.80	1.06	55.00	0.178	0.746	0.176	0.777
2	21	20.911	1.446	73.26	1.43	74.00	0.247	1.036	0.237	1.047
2.5	27	26.148	1.845	94.34	1.96	89.00	0.268	1.515	0.317	1.429
3	32	31.377	2.281	110.09	2.30	109.00	0.413	1.701	0.421	1.684
3.5	37	36.600	2.630	126.99	2.68	124.50	0.440	2.000	0.476	1.961
4	43	41.832	2.911	150.38	3.00	146.00	0.468	2.257	0.492	2.192
4.5	48	47.066	3.263	174.90	3.46	165.00	0.600	2.597	0.654	2.450
Average Force Ratio										0.230

Table A2.25 Experimental data for the two sensors on the different base arrangement, at the different load sets, sample 5

Sample 5										
Force (N)	Meter Reading	Oscilloscope(mV)	mV PVDF 1	mV PVDF 2	mV PVDF 3	mV PVDF 4	N Force 1	N Force 2	N Force 3	N Force 4
1.5	16	14.88	0.730	49.939	0.708	50.490	0.116	0.750	0.116	0.713
2	21	19.84	1.078	71.547	1.078	74.460	0.179	1.012	0.184	1.053
2.5	27	24.81	1.344	94.605	1.406	79.900	0.220	1.505	0.204	1.283
3	32	29.77	1.506	107.060	1.693	105.000	0.262	1.736	0.307	1.622
3.5	37	34.73	1.826	130.968	2.012	121.200	0.309	2.164	0.337	1.909
4	43	39.69	2.089	141.481	2.152	134.640	0.350	2.083	0.346	2.021
4.5	48	44.66	2.386	172.515	2.709	158.100	0.400	2.397	0.437	2.218
Average Force Ratio										0.167

Table A2.26 Experimental data for the two sensors on the different base arrangement, at the different load sets, sample 6

Sample 6										
Force (N)	Meter Reading	Oscilloscope mV	mV PVDF 1	mV PVDF 2	mV PVDF 3	mV PVDF 4	N Force 1	N Force 2	N Force 3	N Force 4
1.5	16	16.809	1.171	53.040	1.194	53.04	0.192	0.735	0.196	0.727
2	21	22.405	1.672	71.280	1.655	71.28	0.266	1.018	0.264	1.039
2.5	27	28.016	2.163	91.350	2.271	91.35	0.415	1.397	0.436	1.313
3	32	33.618	2.534	113.420	2.686	113.42	0.472	1.653	0.501	1.736
3.5	37	39.214	2.906	130.005	3.110	130.005	0.557	1.913	0.596	1.933
4	43	44.820	3.357	140.390	3.391	140.39	0.579	2.087	0.585	2.066
4.5	48	50.428	3.774	162.750	3.962	162.75	0.678	2.566	0.712	2.617
Average Force Ratio										0.282

APPENDIX III

Interfacing with Electronics

A3.1 Capacitance of Piezo Sensor

To use a piezoelectric material as a sensor, it is necessary to make device for measuring its surface charge. One such method consists of sandwiching a piezo between two metal plates to make a capacitor. Metallized PVDF films are available in the market aluminum coated on the both sides.

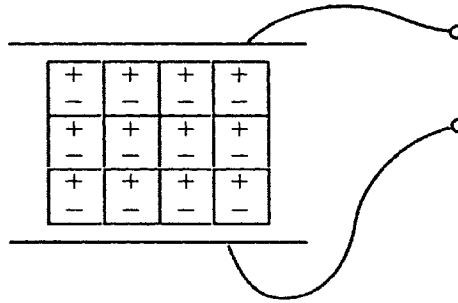


Figure A3.1 PVDF Film act as capacitor with aluminum coating

An applied force will produce a voltage $V = Q_f / C$, where Q_f is the charge resulting from the force and C is the capacitance of the device. The electrical equivalent circuit for this sensor is:

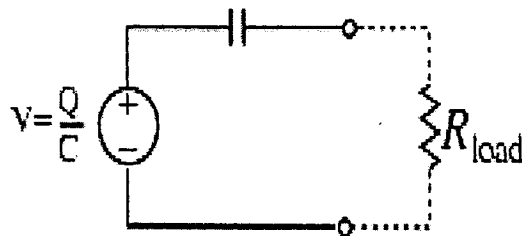


Figure A3.2 Electrical equivalent circuit for sensor

The voltage source represents the voltage that develops due to excess surface charge on the crystal. The capacitor represents the metallic plates. The load resistance results from the act of measuring the voltage across the terminals. Piezo sensors are only useful for measuring dynamic forces, as the capacitance blocks direct current.

A3.1.2. Role of Load Resistance

The most critical part of an interface circuit is the load resistance. Figure A3.3 shows a load resistance that is connected to both sides of piezo film electrodes. The load resistance affects low frequency measurement capability as well as the signal amplitude. It also affects circuit in terms of time constant, loading effect, and frequency response.

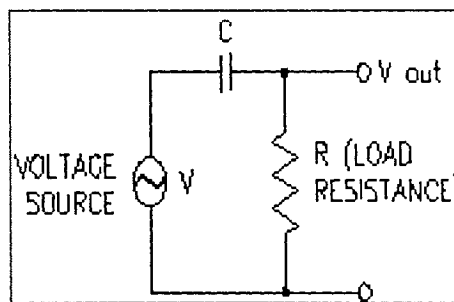


Figure A3.3 Purpose of load resistance

A3.1.3 Charge Amplifier and Voltage Amplifier

Two type of circuit used for the amplification of the piezoelectric sensor. Both the amplification circuit has advantages and disadvantages depending upon application. This amplification can be as charge mode amplification and voltage mode amplification. Both circuits configuration of the charge amplifier and voltage amplifier are shown in the Figure A3.4. The main advantage of charger amplifier exists while using of electronic circuit at distance from the sensor.

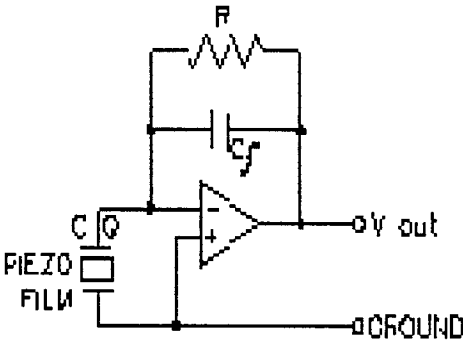
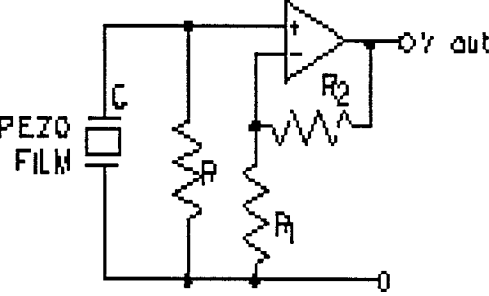
 <p style="text-align: center;">Charge Amplifier</p>	<p>C_f = Feed Back Capacitance</p> <p>$V_{out} = C/C_f$</p> <p>Voltage Gain = C/C_f</p> <p>Time constant = $R C_f$</p>
 <p style="text-align: center;">Voltage Amplifier</p>	<p>Voltage Gain = $1 + R_1/R_2$</p> <p>Time Constant = RC</p>

Figure A3.4 Charger amplifier and voltage Amplifier

It also minimizes the charger leakage. On the other hand voltage amplifier shows less dependence on the temperature. The charger amplifier was used for signal amplification in our case.

A3.2.1 Wheat Stone Bridge Principle

The strain indicator is used for measuring the strain with the help of the LED display. The strain indicator is working on the principle of the wheat stone bridge. In wheat stone bridge four resistances are placed in the series and parallel with the dc power supply. The Figure A3.5 shows the arrangement of the resistances in the circuit. The R_1 ,

R_2, R_3, R_4 represents the resistance in the circuit. DC and e represents the battery and voltmeter, respectively. The balance circuit gives the zero voltage at the voltmeter. In the strain indicator one of the resistances is replaced by the strain gage. The calibrated voltmeter reads the voltage in terms of the resistance change in the strain gage. The gage factor relates the change in the resistance to the change in the strain. The gage factor is mathematical represented in equation A3.1.

$$G.F. = \frac{\frac{\Delta R}{R}}{\frac{\Delta L}{L}} \quad (A3.1)$$

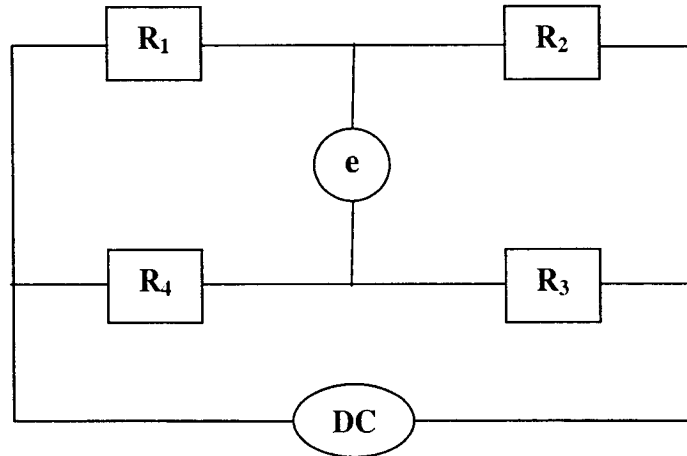


Figure A3.5 Circuit Diagram of the Wheat stone bridge.

The output reading of voltage is calculated with the help of the kirchoff law.

Output:

$$e = \left[\frac{R_2}{R_1 + R_2} - \frac{R_3}{R_3 + R_4} \right] E \quad (A3.2)$$

Balance Condition:

$$R_2 R_4 = R_1 R_3 \quad (A3.3)$$